

UNDERSTANDING NATURE'S PARTICLE ACCELERATORS USING HIGH ENERGY  
GAMMA-RAY SURVEY INSTRUMENTS

By

Anushka Udara Abeysekara

A DISSERTATION

Submitted to  
Michigan State University  
in partial fulfillment of the requirements  
for the degree of

Physics - Doctor of Philosophy

2014

## ABSTRACT

### UNDERSTANDING NATURE'S PARTICLE ACCELERATORS USING HIGH ENERGY GAMMA-RAY SURVEY INSTRUMENTS

By

**Anushka Udara Abeysekara**

Nature's particle accelerators, such as Pulsars, Pulsar Wind Nebulae, Active Galactic Nuclei and Supernova Remnants accelerate charged particles to very high energies that then produce high energy photons. The particle acceleration mechanisms and the high energy photon emission mechanisms are poorly understood phenomena. These mechanisms can be understood either by studying individual sources in detail or, alternatively, using the collective properties of a sample of sources. Recent development of GeV survey instruments, such as Fermi-LAT, and TeV survey instruments, such as Milagro, provides a large sample of high energy gamma-ray flux measurements from galactic and extra-galactic sources. In this thesis I provide constraints on GeV and TeV radiation mechanisms using the X-ray-TeV correlations and GeV-TeV correlations.

My data sample was obtained from three targeted searches for extragalactic sources and two targeted search for galactic sources, using the existing Milagro sky maps. The first extragalactic candidate list consists of Fermi-LAT GeV extragalactic sources, and the second extragalactic candidate list consists of TeVCat extragalactic sources that have been detected by Imaging Atmospheric Cerenkov Telescopes (IACTs). In both extragalactic candidate lists Markarian 421 was the only source detected by Milagro. A comparison between the Markarian 421 time-averaged flux, measured by Milagro, and the flux measurements of transient states, measured by IACTs, is discussed. The third extragalactic candidate list is a list of potential TeV emitting BL Lac candidates that was synthesized using X-ray

observations of BL Lac objects and a Synchrotron Self-Compton model. Milagro's sensitivity was not sufficient to detect any of those candidates. However, the 95% confidence flux upper limits of those sources were above the predicted flux. Therefore, these results provide evidence to conclude that the Synchrotron Self-Compton model for BL Lac objects is still a viable model. Targeted searches for galactic candidates were able to measure TeV emission associated with 14 Fermi-LAT GeV pulsars.

In this thesis I also presented a new multi-wavelength technique that I developed to isolate the flux correlation factor ( $f_{\Omega}$ ) of pulsars as a function of pulsar spin down luminosity. The correlation between  $f_{\Omega}$  and pulsar spin-down luminosity for a Fermi-LAT GeV pulsar sample was measured using the measurements obtained in the Milagro targeted search performed for galactic sources and from the literature. The measured correlation has some features that favor the Outer Gap model over the Polar Cap, Slot Gap and One Pole Caustic models for pulsar emission in the energy range of 0.1 to 100 GeV. However, these simulated models failed to explain many other important pulsar population characteristics. Therefore, further improvements on the galactic pulsar population simulations are needed to provide tighter constraints.

I dedicate my dissertation work to my family.

## ACKNOWLEDGMENTS

First of all, I like to thank my parents, wife and little son for their continuous caring, support and encouragement. I cannot express enough thanks to my thesis adviser Prof. Jim Linnemann for offering me the opportunity to work with him and his continuous support during my days in graduate school.

I also like to extend my deepest gratitude to all of my thesis committee members: Dr. Gus Sinnis, Prof. Kirsten Tollefson, Prof. Scott Pratt, and Prof. Mark Voit for their advice and assistance. Their sincere guidance and comments helped shape this thesis in the best way possible.

All the members of the Milagro and HAWC collaborations deserve special thanks. There are too many special people in both collaborations to name here; it has been my good fortune to be a part of such a supportive and intelligent group of people.

Last but not least I want to thank Michigan State University postdoc Dr. Tilan Ukwatta, graduate student Samuel Marinelli, my office mates, all of my teachers in the past and Michigan State University staff members who helped me to successfully finish my PhD.

# TABLE OF CONTENTS

<b>LIST OF TABLES</b> . . . . .	<b>ix</b>
<b>LIST OF FIGURES</b> . . . . .	<b>xi</b>
<b>Chapter 1 Gamma-ray Astronomy</b> . . . . .	<b>1</b>
1.1 Introduction to Gamma-ray Astronomy . . . . .	1
1.2 Modern Gamma-ray Detectors . . . . .	3
1.2.1 Space-based Detectors . . . . .	4
1.2.2 Ground-based Detectors . . . . .	4
1.3 Imaging Atmospheric (or Air) Cherenkov Telescopes (IACTs) . . . . .	6
1.4 Extensive Air Shower (EAS) Arrays . . . . .	7
<b>Chapter 2 Gamma-ray sources</b> . . . . .	<b>9</b>
2.1 Non-thermal Gamma-ray Production Processes . . . . .	9
2.1.1 Synchrotron Radiation . . . . .	10
2.1.2 Curvature Radiation . . . . .	11
2.1.3 Inverse Compton Radiation . . . . .	12
2.2 Pulsars . . . . .	13
2.2.1 Properties of Neutron Stars . . . . .	14
2.2.2 Pulsar Spin Evolution . . . . .	15
2.2.3 Spin-down Luminosity Evolution . . . . .	16
2.2.4 Characteristic Age of a Pulsar . . . . .	17
2.2.5 Pulsar Magnetosphere . . . . .	18
2.3 Pulsar Wind Nebulae . . . . .	19
<b>Chapter 3 The Milagro Observatory</b> . . . . .	<b>24</b>
3.1 Milagro Detector . . . . .	24
3.1.1 The Main Pond . . . . .	25
3.1.2 The Outrigger Array . . . . .	29
3.2 Front-end Electronics and Time to Digital Converter . . . . .	29
3.3 Trigger . . . . .	32
3.4 Reconstruction . . . . .	35
3.4.1 Shower Core Location Reconstruction . . . . .	35
3.4.2 Incidence Angle Reconstruction . . . . .	36
3.5 Monte Carlo Simulations . . . . .	38
<b>Chapter 4 Milagro Data Analysis Framework</b> . . . . .	<b>41</b>
4.1 Gamma/Hadron Separation Parameter . . . . .	41
4.2 Background Estimation . . . . .	42

4.3	Significance Maps . . . . .	45
4.4	Flux calculation . . . . .	46
4.5	Energy Reconstruction . . . . .	48
<b>Chapter 5</b>	<b>The Fermi Large Area Telescope (Fermi-LAT) GeV Catalogs</b>	<b>52</b>
5.1	Fermi Large Area Telescope (Fermi-LAT) . . . . .	53
5.2	Fermi-LAT Second Source Catalog (2FGL) . . . . .	54
5.3	The Second Fermi-LAT Catalog of Gamma-ray Pulsars (2PC) . . . . .	57
5.4	Source Naming Convention . . . . .	58
<b>Chapter 6</b>	<b>The High Altitude Water Cherenkov Observatory (HAWC)</b>	<b>60</b>
6.1	The HAWC Detector . . . . .	60
6.2	GPS Timing and Control System (GTC System) . . . . .	63
6.2.1	GPS Timing System Hardware . . . . .	63
6.2.2	GPS Timing System Firmware . . . . .	65
6.2.3	Control System Hardware . . . . .	69
6.2.4	Control System Firmware . . . . .	72
6.3	Performance of the GTC system . . . . .	74
6.4	Additional Capabilities of H_Clock cards . . . . .	75
<b>Chapter 7</b>	<b>Data Analysis Methodology</b>	<b>77</b>
7.1	False Discovery Rate method . . . . .	78
7.1.1	Calculation . . . . .	79
7.2	Stack Analysis . . . . .	79
<b>Chapter 8</b>	<b>Milagro Observations of Extragalactic Sources</b>	<b>81</b>
8.1	Targeted Search for 2FGL Extragalactic Sources . . . . .	82
8.1.1	Comparison with Previous $\gamma$ -ray Flux Measurements . . . . .	83
8.1.2	Undetected Candidates . . . . .	84
8.2	Targeted Search for TeVCat Extragalactic Sources . . . . .	85
8.3	Targeted Search for Potential TeV Emitting BL Lac Objects . . . . .	87
<b>Chapter 9</b>	<b>The Milagro Targeted Search for GeV Pulsars.</b>	<b>94</b>
9.1	Comparison With IACT Flux Measurements . . . . .	98
9.2	Population Study of Associated TeV emissions . . . . .	102
9.3	Discussion . . . . .	107
<b>Chapter 10</b>	<b>Experimental Constraints on Gamma-Ray Pulsar Gap Models</b>	<b>115</b>
10.1	A New Method to Isolate $f_{\Omega}$ . . . . .	116
10.2	The Sample of Pulsars and Their Associated PWNe . . . . .	119
10.3	Results and Discussion . . . . .	124
<b>Chapter 11</b>	<b>Milagro Observations of Fermi-LAT Galactic Sources</b>	<b>129</b>

<b>Chapter 12 Conclusions</b> . . . . .	<b>137</b>
<b>APPENDIX</b> . . . . .	<b>140</b>
<b>BIBLIOGRAPHY</b> . . . . .	<b>146</b>



## LIST OF TABLES

Table 3.1	The reconstructed shower properties that were used in the work presented in this thesis. The term ‘Cal’ stands for calibrated. . . . .	40
Table 6.1	The error status corresponding to each time-stamp is encoded into the 4 most significant bits of the time-stamp The meaning of each error code is shown. . . . .	69
Table 8.1	The gamma-ray flux of Markarian 421 at 7 TeV in the high flux state, low flux state and the average flux is summarized . . . . .	84
Table 8.2	Summary of the search with $\lambda = 0.01$ for TeV emission from the 2FGL list that are identified as candidates off the galactic plane. (Note that we used the same abbreviations for the source type as the 2FGL, agu = active galaxy of uncertain type, bzb = BL Lac type of blazar and bzb = FSRQ type of blazar.) The Milagro flux derived at 7 TeV is given for candidates that passed the $\lambda = 0.01$ FDR cut and the 95% confidence level flux upper limit is given for the rest. . . . .	89
Table 9.1	Summary of the search with $\lambda = 0.01$ for TeV emission from the pulsars in the second Fermi-LAT pulsar catalog. The Milagro photon flux derived in the energy band from 34.5 TeV to 35.5 TeV is given for the candidates that passed the $\lambda = 0.01$ FDR cut and 95% confidence level flux upper limits are given for the rest. . . . .	97
Table 9.2	Properties of the Fermi-LAT pulsars in the Milagro sky coverage. Column 2 ( $G_{100}$ ) is the the phase-averaged integral energy flux in the 0.1 to 100 GeV energy band. Column 3 is the $\text{Log}_{10}$ of the pulsars spin-down luminosity. Column 4 is the pulse period. Column 5 is the first time derivative of the pulse period. Column 6 is the distance to pulsar. All of these values are taken from the Fermi-LAT second pulsar catalog. . . . .	99
Table 9.3	The energy flux derived in the energy band from 34.5 TeV to 35.5 TeV is summarized. The first column is the name given in the Fermi-LAT second pulsar catalog. The second column is the name given in the TeVCat catalog. The third column is the flux measured by IACTs. The fourth column is the flux measured by Milagro. (a) Flux measurements were derived from VERITAS measurements. (b) Flux measurements were derived from H.E.S.S. measurements. . . .	101

Table 10.1	<p><math>G_{100}</math> is the integrated phase-averaged energy flux of the pulsar GeV emission in the 0.1-100 GeV energy band. <math>F_{PWN\ TeV}</math> is the integrated energy flux of the PWN TeV emission in the 34.5-35.5 TeV energy band. Properties of a sample of GeV pulsars cataloged in the Fermi-LAT Second Pulsar Catalog and the TeV flux of their associated PWNe. (a). VERITAS Measurement, Energy flux derived by extrapolating the SED, reference [Aliu et al.(2013)] (b). H.E.S.S. Measurement, reference [Aharonian et al.(2006a)] (c). H.E.S.S. Measurement, reference [Aharonian et al.(2006b)] (d). H.E.S.S. Measurement, Energy flux derived by extrapolating the SED, reference [Aharonian et al.(2006d)] (e). H.E.S.S. Measurement, reference [Aharonian et al.(2005)] (f). H.E.S.S. Measurement, Energy flux derived by extrapolating the SED, reference [H. E. S. S. Collaboration et al.(2007)] (g). VERITAS Measurement, Energy flux derived by extrapolating the SED, reference [Aliu et al.(2013)] . . . . .</p>	120
Table 11.1	<p>Summary of the search with <math>\lambda = 0.01</math> for TeV emission from the pulsars in the 2FGL list that were not listed in the 0FGL. (Note that we used the same abbreviations for the source type as the 2FGL: PSR = Pulsar identified by pulsations and psr = Pulsar identifies by spatial association.) The Milagro flux derived at 35 TeV is given for the candidates that passed the <math>\lambda = 0.01</math> FDR cut and 95% confidence level upper limits are given for the rest. . . . .</p>	136
Table A.1	<p>Epoch live times . . . . .</p>	145

## LIST OF FIGURES

Figure 1.1	The Fermi-LAT sky map derived from gamma-rays of energies between 100 MeV and 10 GeV. Colored circles indicate the TeV sources listed in TeVCat online catalog ( <a href="http://tevcat.uchicago.edu/">http://tevcat.uchicago.edu/</a> ) as of April 16 <sup>th</sup> 2013. This sky map was created using the online tool available in the TeVCat web site. . . . .	3
Figure 1.2	A schematic diagram of the technique used in Imaging Atmospheric (or Air) Cherenkov Telescopes (IACTs). The original image was downloaded from <a href="http://veritas.sao.arizona.edu/about-veritas-mainmenu-81/atmospheric-cherenkov-technique-and-veritas-technologies-mainmenu-87">http:// veritas. sao. arizona. edu /about - veritas - mainmenu - 81/ atmospheric- cherenkov - technique- and- veritas- technologies-mainmenu-87</a> . . . . .	7
Figure 2.1	A simplistic toy model for a neutron star and its magnetic sphere. Reference: Handbook of Pulsar Astronomy by Lorimer and Kramer.	20
Figure 2.2	Pulsar Gap regions in the pulsar magnetosphere are marked in different colors. Reference: Alice Harding’s presentation “Gamma-Ray Pulsars Theory and Modeling” at Fermi Summer School 2011. . . . .	21
Figure 3.1	An aerial photograph of the Milagro detector. The pond is at the center of this photograph and red circles mark the locations of the outrigger tanks. . . . .	25
Figure 3.2	This picture was taken during the cleaning process of the Milagro site a few years after the Milagro shutdown. The Milagro water pond is visible on the left side of this picture and several outrigger tanks are visible around the pond. . . . .	26
Figure 3.3	This is an inside view of the Milagro pond. Two layers of PMTs are visible in this picture. . . . .	28
Figure 3.4	This schematic diagram shows the PMT placement inside the Milagro pond. The first layer, the Air Shower Layer, was placed 1.5 m below the water surface. The second layer, the Muon layer, was placed 6 m below the water surface. . . . .	29
Figure 3.5	Functional block diagram of the Milagro front-end analog electronic board. . . . .	30

Figure 3.6	The two analog signals shown at the top of this figure represent the shape of a typical PMT output signal. The one on the left has a high amplitude and the one on the right has a lower amplitude. The two digital signals shown at the bottom are the outputs of the two discriminators. . . . .	31
Figure 3.7	Functional block diagram of the Milagro front-end digital electronic board. . . . .	33
Figure 3.8	A conceptual diagram of the shower core location reconstruction. As an EAS lands on the Milagro detector, PMTs at the core of the shower detect larger numbers of photo electrons (PEs) compared to the PMTs at the edges of the shower. The histogram at the bottom shows the conceptual amplitude distribution of PEs. . . . .	37
Figure 3.9	A conceptual diagram of the shower incidence angle reconstruction in a 2 dimensional space. As an EAS lands on the Milagro detector with an angle $\theta$ , one end of the shower lands on the detector earlier than the other end. The histogram at the bottom shows the conceptual distribution of the arrival times of a shower on each PMT relative to the shower arrival time at the first PMT. . . . .	39
Figure 4.1	$R(\tau)$ shown in the top histogram is the all sky background event rate. $\varepsilon(h, \delta)$ shown in the second histogram from the top is the unit-normalized local-coordinate distribution of background event rate. $B(\alpha, \delta)$ shown in the third histogram from the top is the convolution of the $R(\tau)$ and $\varepsilon(h, \delta)$ . $B(\alpha, \delta)$ is the background estimation of the two hour data set as a function of right ascension $\alpha$ and declination $\delta$ . The fourth histogram from the top is the raw signal collected within a 4 hour period, $S(\alpha, \delta)$ . The histogram at the bottom is the background subtracted signal, $S(\alpha, \delta) - B(\alpha, \delta)$ . . . . .	44
Figure 4.2	Simulated $\frac{dN}{dE}$ as a function of energy for a pure power law spectrum is shown, $\frac{dN}{dE} = I_0(E/\text{TeV})^{-\alpha}$ . $I_0$ 's are selected to give the same excess for three sources with three different spectra, green $\alpha = 2.2$ , red $\alpha = 2.6$ and blue $\alpha = 3.0$ . Flux for all three sources are calculated using spectral optimization of $\alpha = 2.6$ . The region where the lines intersect indicates the energy range least dependent on the assumed spectrum. . . . .	48
Figure 4.3	Two significance contour plots in the $\alpha - E_C$ and $\alpha - I_0$ space obtained from forward folding are shown[Abdo et al.(2012)]. The spectral assumption is a power law with an exponential cutoff, as shown in equation 4.10. The figure on the left shows the $1\sigma$ and $2\sigma$ contours in the $\alpha - E_C$ space. The figure on the right shows the $1\sigma$ and $2\sigma$ contours in the $\alpha - I_0$ space. . . . .	50

Figure 5.1	Schematic diagram of Fermi-LAT. A precision converter-tracker and calorimeter is shown at the center of the figure. Here the calorimeter is taken apart from the precision converter-tracker. The red dotted line indicates the track of a gamma-ray and the blue dotted lines indicate the tracks of the cascade electron and positron. The physical size of this detector is $1.8 \text{ m} \times 1.8 \text{ m} \times 0.72 \text{ m}$ . It weighs 2789 kg and in normal operation mode consumes 650 W. This figure was obtained from the publication [Atwood et al.(2009)]. . . . .	55
Figure 5.2	The Aitoff projection of the significance sky map derived from the data set used to make the Fermi Large Area Telescope Second Source catalog. This map includes the gamma-ray energy flux measured in the range between 100 MeV and 10 GeV. Refer to [Nolan et al.(2012)] for the original figure and a more detailed description of data. Color scale shows the gamma-ray significance of each sky location. . . . .	56
Figure 6.1	A drawing of a HAWC tank with 4 PMTs at the bottom. . . . .	61
Figure 6.2	A photograph of a fully assembled H_Clock card is shown. The Clock version of the H_Clock card with 2 general purpose input ports and 8 general purpose output ports are used in the Clock System. The Control version of the H_Clock card used in the Control System has 4 general purpose input ports and 6 general purpose output ports. . . . .	64
Figure 6.3	A block diagram of the Clock System is shown. The NAVSYNC CW46 GPS receiver and the Clock Card are the two main components of the Clock system. The GPS receiver is used to obtain the GPS time and a low jitter 10 MHz signal. The Clock Card produces a 40 MHz global clock signal and two time-stamps for the scaler system and for the TDC system. The communication between the Clock Card and the control computer is accomplished through a A24D16 VME interface. . . . .	65
Figure 6.4	A simplified functional block diagram of the Clock firmware is shown. This firmware maintains an internal clock synchronized with the GPS time and produces TDC readable time-stamps. The communication between this module and the control computer was done by a A24D16 VME interface. . . . .	66
Figure 6.5	Encoding of the time-stamp 12.34567 seconds with no errors is shown. Each digit is encoded into a 4 bit binary number, and each binary number is then encoded into a pulse. A $1\mu\text{s}$ wide pulse is used to indicate logic 0 and, a $2\mu\text{s}$ wide pulse is used to indicate logic 1. . . . .	68

Figure 6.6	A block diagram of the Control System. The Control system consists of two VME cards: the Control Card and CB_Fan card. The Control card does all the logical operations and the CB_Fan card does the appropriate level conversion to interface TDCs to the Control Card.	70
Figure 6.7	A photograph of the fully assembled CB_Fan card is shown. A CB_Fan card is able to provide the level conversions and Fan-outs required to handle 6 TDCs. . . . .	71
Figure 6.8	A simplified functional block diagram of the Control firmware is shown. The Trigger, CLR, and CRST modules generate the TDC control signals, and LNE, Pause Pulses, Busy Pulses and 10 MHz Reference produces signals to the scaler system. Similar to the Control firmware, communication between the Control system and the control computer was done by a A24D16 VME interface. . . . .	73
Figure 8.1	This map shows the $5^\circ \times 5^\circ$ region around Markarian 421. The Fermi-LAT source position is marked by a white dot. This map is made with the spectral optimization $dN/dE \propto E^{-2.0} e^{-\frac{E}{5\text{TeV}}}$ and the data have been smoothed by a Gaussian point spread function. The color of a bin shows the statistical significance (in standard deviations) of that bin. The horizontal axis is right ascension in hours and the vertical axis is declination in degrees. . . . .	92
Figure 8.2	The horizontal axis is the declination in the Milagro sky coverage. The vertical axis is the energy flux in $\text{erg cm}^{-2}\text{s}^{-1}$ . The red triangle data points are Milagro upper limits of BL Lac objects at 7 TeV, the blue square data points are the theoretically predicted flux at 7 TeV and the black solid line is the 95% confidence level expected upper limit of the flux for extragalactic sources corresponding to zero excess derived at 7 TeV for each declination band of the Milagro sky maps made with spectral assumption $E^{-2.0} \exp -E/5\text{TeV}$ . . . . .	93
Figure 9.1	These maps show the $5^\circ \times 5^\circ$ region around the pulsars that passed the $\lambda = 0.01$ FDR cut. The LAT source positions are marked by white dots. These maps are made with the spectral optimization $dN/dE \propto E^{-2.6}$ and the data have been smoothed by a Gaussian point spread function. The color of a bin shows the statistical significance (in standard deviations) of that bin. The horizontal axis is right ascension in hours and the vertical axis is declination in degrees.	111

Figure 9.2	PWN TeV luminosity vs. Pulsar GeV luminosity normalized with respect to the beaming factor ( $f_{\Omega}$ ). Blue squares are the luminosity derived in the energy band from 34.5 TeV to 35.5 TeV of the candidates that passed the $\lambda = 0.01$ FDR cut. Red triangles are the upper limit of the luminosity derived in the energy band from 34.5 TeV to 35.5 TeV of the candidates that failed the $\lambda = 0.01$ FDR cut. The linear correlation coefficient calculated only using the candidates that passed the $\lambda = 0.01$ FDR cut is 0.73, and the best fit line for these data points have a slope of $0.79 \pm 0.05$ and intercept of $3.5 \pm 1.8$ and $\chi^2/NDF = 129.531/9$ . . . . .	112
Figure 9.3	The PWN gamma-ray flux in the 34.5 to 35.5 TeV energy band is shown ( $F_{TeV}$ ). The blue squares are the flux of the candidates that passed the $\lambda = 0.01$ FDR cut. The red triangles are the upper limits of the candidates that failed the $\lambda = 0.01$ FDR cut. . . . .	113
Figure 9.4	Fraction of the PWNe that passed the $\lambda = 0.01$ FDR cut in one-decade bins of the $\dot{E}/d^2$ . . . . .	113
Figure 9.5	Distributions of PWNe luminosity in the 34.5 to 35.5 TeV energy band $L_{PWN\ TeV}$ vs. the spin-down luminosity $\dot{E}$ of the associated pulsars (a), and $L_{PWN\ TeV}$ vs. the characteristic age ( $\tau_c$ ) of the associated pulsars (b) are shown. Blue squares are the $L_{PWN\ TeV}$ of the candidates that passed the $\lambda = 0.01$ FDR cut. Red triangles are the upper limit of the $L_{PWN\ TeV}$ of the candidates that failed the FDR cut. . . . .	114
Figure 9.6	TeV efficiency of PWNe, $\varepsilon_{\gamma}$ , vs. $\dot{E}$ (a), and $\varepsilon_{\gamma}$ vs. $\tau_c$ (b) distributions are shown. $\varepsilon_{\gamma}$ is defined as shown in Equation 10.16. Blue squares are the $\varepsilon_{\gamma}$ of the candidates that passed the $\lambda = 0.01$ FDR cut. Red triangles are the $\varepsilon_{\gamma}$ upper limit of the candidates that failed the FDR cut. . . . .	114
Figure 10.1	PWN TeV luminosity vs. Pulsar GeV luminosity normalized with respect to the flux correlation factor ( $f_{\Omega}$ ). Blue squares are measured by Milagro. Red stars are measured by H.E.S.S. Green circles are measured by VERITAS. The dotted line is the best fit line. The linear correlation coefficient is $R = 0.8$ . The error bars are dominated by the distance measurement uncertainties. . . . .	121
Figure 10.2	PWN TeV luminosity vs. spin-down luminosity ( $\dot{E}$ ) of the associated pulsar. Blue squares are for PWNe measured by Milagro, red stars by H.E.S.S., and green circles by VERITAS. The distance uncertainty contributes significantly to the error bars. The data are consistent with no dependence of $L_{PWN\ TeV}$ on $\dot{E}$ . . . . .	122

Figure 10.3	Experimentally obtained $f_{\Omega}$ vs. pulsar spin-down luminosity $\dot{E}$ . Blue squares are PWNe measured by Milagro, red stars by H.E.S.S, and green circles by VERITAS. The best fit line for the pulsars with $\dot{E} > 10^{35.1}$ ergs s $^{-1}$ is shown as a dotted line. . . . .	124
Figure 10.4	The distribution of the beaming factor ( $f_{\Omega}$ ) as a function of spin-down luminosity ( $\dot{E}$ ) for four models derived by [Pierbattista et al.(2012)]. This plot was reproduced by M. Pierbattista with linear fits for pulsars above $\dot{E} = 10^{35}$ ergs s $^{-1}$ . For the original figure refer to [Pierbattista et al.(2012)]. Purple and green markers refer to the radio-loud and radio-quiet pulsars, respectively. Black lines refer to the best linear fits for the pulsars with $\dot{E} > 10^{35}$ ergs s $^{-1}$ . . . . .	126
Figure 11.1	The fraction of Fermi-LAT sources seen by Milagro as a function of half-decade bins of the integrated time-averaged Fermi flux ( photons cm $^{-2}$ s $^{-1}$ ) in the energy range from 100 MeV to 100 GeV. . . . .	134
Figure 11.2	The fraction of Fermi-LAT sources seen by Milagro as a function of half-decade bins of the integrated phase-averaged Fermi flux ( photons cm $^{-2}$ s $^{-1}$ ) in the energy range from 100 MeV to 100 GeV. . . . .	135
Figure A.1	Comparison between Monte Carlo simulated data and real data for cosmic-rays. In the top figure, the red data points show the distribution of the energy estimator of the Monte Carlo simulated data. In the top figure, the blue data points show the distribution of the energy estimator of the real data. In the bottom figure, the blue data points show the ratio data/monte Carlo simulations. . . . .	143
Figure A.2	Correlation between the energy estimators and true energy. Histogram to the left is the correlation between EBNN and log(Energy). Histogram to the right is the correlation between FRASOR, the old energy estimator, and log(Energy). Both of these plots were made using a simulated data sample. . . . .	143
Figure A.3	Unit-normalized distribution of true energies for events in EBNN bins, 0.2-0.4, 0.4-0.6, 0.6-0.8, 0.8-1.0, 1.0-1.2, 1.2-1.4, 1.4-1.6, 1.6-1.8 and 1.8-2.0. . . . .	144
Figure A.4	Unit-normalized distribution of true energies for events in FRASOR bins, 0.2-0.4, 0.4-0.6, 0.6-0.8, 0.8-1.0, 1.0-1.2, 1.2-1.4, 1.4-1.6, 1.6-1.8 and 1.8-2.0. . . . .	144



# Chapter 1

## Gamma-ray Astronomy

Astronomy is one of the oldest natural sciences dating back to the prehistoric period. Historical records show that almost every civilization such as the Babylonians, Greeks, Chinese, Indians, Iranians and Mayans observed the night sky and recorded them in their own way. In the early stages, astronomers observed the night sky from the visible light emission or reflection from cosmic objects. With the development of new technology astronomers were able to observe the universe using electromagnetic radiation all the way from radio waves to TeV gamma-rays.

### 1.1 Introduction to Gamma-ray Astronomy

The first cosmic gamma-rays were observed by Vela satellites, which were part of a US military program. A study performed in 1973 was able to find sixteen gamma-ray bursts in the energy range 0.2 to 1.5 MeV<sup>1</sup> [Klebesadel et al.(1973)]. The first dedicated satellite missions designed to detect gamma-rays were the Small Astronomy Satellite (SAS-2) in

---

<sup>1</sup>1 MeV = 10<sup>6</sup> eV

1972 and the COS-B mission in 1975. Both missions were able to observe the Vela and the Crab pulsar wind nebulae. In 1981 the COS-B satellite produced a source catalog with 25 detections above 100 MeV [Swanenburg et al.(1981)]. Since then gamma-ray emission from many different types of cosmic objects have been detected, such as pulsars, pulsar wind nebulae (PWNe) and Active Galactic Nuclei. The latest Fermi Large Area Telescope (Fermi-LAT) catalog known as the 2FGL [Nolan et al.(2012)] contains 1873 sources detected in the 100 MeV to 100 GeV energy range. Most of these sources do not have a spatial association with the sources listed in the earlier catalogs such as 1<sup>st</sup> AGILE catalog, the 3<sup>rd</sup> EGRET Gamma-ray catalog or the EGRET Revised catalog.

The first TeV gamma-ray emission from a cosmic object, the Crab Pulsar Wind Nebula, was detected in 1989 by a ground-based instrument called the Whipple Imaging Atmospheric Cherenkov Telescope [Weekes et al.(1989)]. Since then TeV gamma-ray emission from many different types of cosmic objects have been identified. As of April 16<sup>th</sup> 2013 the online TeV source catalog called TeVCat(<http://tevcat.uchicago.edu/>) had 153 sources. Figure 1.1 shows the TeVCat sources marked on the Fermi-LAT sky map derived from  $\gamma$ -rays in the energies between 100 MeV and 10 GeV.

At present, the GeV catalogs such as the Fermi-LAT catalogs and the TeV catalogs such as TeVCat can be considered as two categories by the energy range in which the sources were detected. However, with the current advancement of instrumentation the energy gap between the GeV catalogs and the TeV catalogs is filling with new measurements. When this gap is filled, catalogs in these two energy bands will become a single catalog with measurements all the way from 10s GeVs to 10s of TeVs. The expansion of the energy range is necessary to understand the characteristics of the sources, and the measurements of a broad energy range can be turned into a coherent picture of the underlying acceleration

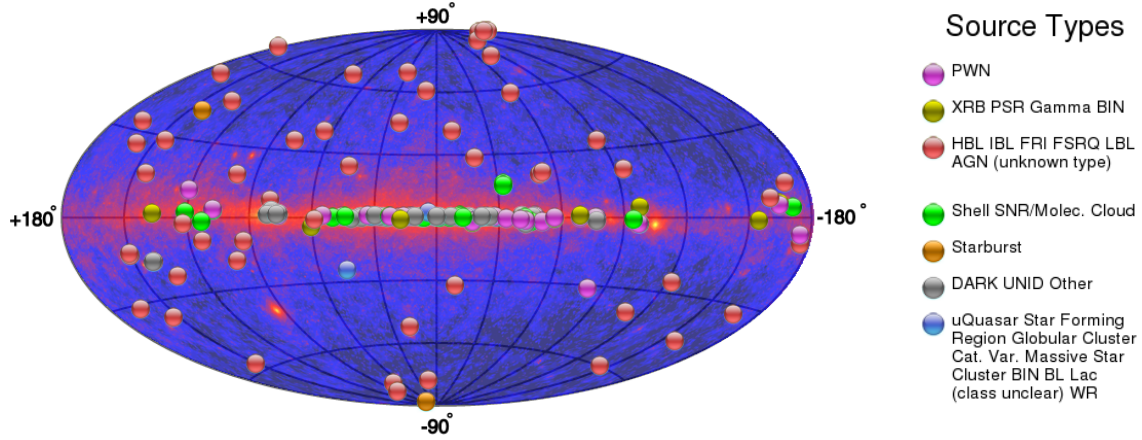


Figure 1.1: The Fermi-LAT sky map derived from gamma-rays of energies between 100 MeV and 10 GeV. Colored circles indicate the TeV sources listed in TeVCat online catalog (<http://tevcad.uchicago.edu/>) as of April 16<sup>th</sup> 2013. This sky map was created using the online tool available in the TeVCat web site.

mechanisms. Even many decades after the first discovery of GeV and TeV sources, the exact acceleration mechanisms that produce gamma-rays observed from individual sources are poorly understood. Most of the generally accepted mechanisms require the acceleration of charged particles to relativistic speeds. These relativistic charged particles produce gamma-rays through leptonic or hadronic interactions, such as curvature radiation, synchrotron radiation, inverse Compton scattering and Bremsstrahlung.

## 1.2 Modern Gamma-ray Detectors

Today's gamma-ray detectors can be divided into two main categories: space-based and ground-based detectors. Fermi-LAT is an example of a space-based GeV gamma-ray telescope. VERITAS and Milagro are examples of ground-based TeV gamma-ray observatories.

### 1.2.1 Space-based Detectors

Space-based detectors are carried by satellites that orbit the earth or sometimes are carried by high altitude balloons. They are capable of detecting gamma-rays directly using the interactions of gamma-rays with the detector material when gamma-rays pass through the detector. The main advantages of this technique are excellent background rejection capability, very good energy resolution and long exposure. A larger duty cycle is also an advantage of space-based detectors over the ground-based observatories that use the Air Cherenkov technique. However, water Cherenkov gamma-ray observatories such as Milagro have comparable duty cycles. The main disadvantage of space-based detectors is the limited effective area due to the limited physical size of the detector. The gamma-ray flux from sources typically decreases as a power law with increasing energy. Therefore the probability of a very high energy photon going through a detector of size  $\sim 1 \text{ m}^2$  becomes very small. This limits the ability to use space-based detectors as gamma-ray observatories above a few 100s of GeVs. At present the most sensitive space-based GeV gamma-ray telescope is the Fermi gamma-ray observatory, which is discussed in Chapter 5.

### 1.2.2 Ground-based Detectors

Ground-based TeV observatories use the by-products of gamma-ray-earth-atmosphere interactions to determine the properties of the primary gamma-ray. When a gamma-ray enters the earth's atmosphere, it produces a relativistic electron-positron pair by pair production. As these particles travel through the atmosphere, they lose energy by producing secondary photons through bremsstrahlung; these photons also produce new electron-positron pairs. This electromagnetic cascade continues until the photon energy drops below the threshold

for pair production. The result of this process is a shower of relativistic charged particles, which is known as an Extensive Air Shower (EAS). When an EAS front propagate through the atmosphere its lateral extent gets broader and the total energy of the shower front dissipates through the atmosphere. The altitude at which the number of particles in the shower reaches its maximum is called the shower maximum altitude. The shower maximum altitude depends on the energy of the initial photon and the altitude of its first pair production. Below the shower maximum altitude the number of particles that can be detected becomes lower. Therefore the altitude of a ground-based detector is important for detecting shower particles.

Typically TeV gamma-rays can create EAS shower fronts with a diameter of lateral extent of  $\sim 100$  m. It is cheaper to built ground-based detectors to cover a large area, compared to space-based detectors. Therefore, it is possible to build ground-based detectors with an effective area of  $\sim 10^5$  m<sup>2</sup> in contrast to the  $\sim 1$ m<sup>2</sup> effective area of space-based detectors. The large effective area of a ground-based detectors increases the probability of detecting gamma-rays with low flux at high energies.

Currently existing ground-based TeV gamma-ray observatories are divided into two categories based on the technique used : Imaging Atmospheric (or Air) Cherenkov Telescopes and Extensive Air Shower Arrays.

## 1.3 Imaging Atmospheric (or Air) Cherenkov Telescopes (IACTs)

Relativistic electrons and positrons in an EAS produce Cherenkov light along the air shower direction. The maximum Cherenkov light emission occurs when the number of particles in the cascade process is the largest. This maximum occurs at an altitude of  $\sim 10$  km for a shower generated from a primary photon with energy in the 100 GeV - 1 TeV range, and this creates a light pool on the ground. After absorption and scattering in the atmosphere, this Cherenkov light arrives on earth as brief flashes of a few nanoseconds duration. These Cherenkov light pulses can be collected to a focal point by placing a reflector telescope inside the light pool. The light collected on the focal point can be detected using a fast photon detector such as Photo Multiplier Tubes(PMTs). Figure 1.2 shows a schematic diagram of this concept.

Not only high energy gamma-rays but also hadronic cosmic rays can create EASs, and the Cherenkov light generated by hadronic cosmic rays are the largest background for IACTs. Cherenkov images that result from gamma-rays appear as narrow elongated ellipses in the focal plane, while hadronic cosmic ray initiated showers produce wider and less regular patterns. These unique features of the Cherenkov images are used to discriminate gamma-ray photon events from hadronic cosmic ray events, and to reconstruct the photon energy and the arrival direction of the initial gamma-ray photon. Examples of modern IACTs are High Energy Stereoscopic System (H.E.S.S.) [Hinton(2004)] and VERITAS [Gibbs et al.(2003)], and an example of a future IACT is the Cherenkov Telescope Array (CTA) [Pareschi et al.(2013)].

The advantages of the IACT technique are high angular resolution ( $< 0.2^\circ$ ), energy resolution ( $\sim 15\%$ ) and point source sensitivity. The sensitivity of modern IACTs is sufficient to

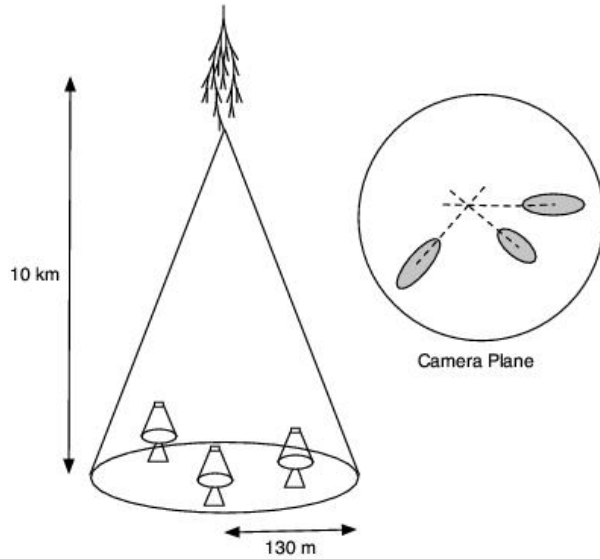


Figure 1.2: A schematic diagram of the technique used in Imaging Atmospheric (or Air) Cherenkov Telescopes (IACTs). The original image was downloaded from [http:// veritas.sao.arizona.edu /about - veritas - mainmenu - 81/ atmospheric- cherenkov - technique- and- veritas- technologies-mainmenu-87](http://veritas.sao.arizona.edu/about-veritas-mainmenu-81/atmospheric-cherenkov-technique-and-veritas-technologies-mainmenu-87)

detect the Crab pulsar wind nebula within order of hours. This sensitivity allowed IACTs to successfully perform multi-wavelength campaigns. On the other hand the main disadvantage of this technique is the limited duty cycle ( $\sim 10\%$ ) and small field-of-view. The limited duty cycle in combination with a small field-of-view makes IACTs harder to use as survey instruments or for observing diffuse sources with large angular extents. Ground-based Extensive Air Shower (EAS) Arrays remove these limitations.

## 1.4 Extensive Air Shower (EAS) Arrays

Examples of different types of modern EAS arrays are the Auger observatory, the Tibet AS-gamma Experiment and the Milagro observatory. The Auger observatory consists mainly of 1,600 water tanks, separated by 1.5 km. These tanks are dark inside except when relativistic particles from an EAS pass through the water in the tank and produce Cherenkov light.

These Cherenkov photons are detected by PMTs placed inside the tanks. Properties of the EAS can be measured by studying the PMT signals. Apart from these water tanks Auger is also equipped with fluorescence detectors to detect the atmospheric Cherenkov light. However, the primary goal of Auger is not to detect EAS initiated by gamma-ray photons, but to detect EAS generated by hadronic cosmic ray particles.

The Tibet AS-gamma experiment consists of scintillation counters made of plastic scintillator plates. These scintillator plates are placed on a lattice. When relativistic particles from an EAS pass through these plates they produce photons that can be detected by the attached PMTs. The properties of the PMT signals are used to reconstruct the properties of the EAS, which can be related to the properties of the gamma-ray that initiated the EAS. The major disadvantages of this technique are the high cost of scintillation plates, the poor sensitivity to low energies, and no background rejection. The Milagro gamma-ray detector overcame these disadvantages by using a water filled pool as the detector medium. Details of the Milagro detector are discussed in Chapter 3.



# Chapter 2

## Gamma-ray sources

TeV gamma-ray emission has been identified from many different types of gamma-ray sources, including Active Galactic Nuclei (AGN), Pulsar Wind Nebulae (PWNe), and Super Nova Remnants (SNRs). Many of the detected sources are AGNs and PWNe. As of June 24<sup>th</sup>, 2013 about 40% of the reported TeV sources in TeVCat were AGNs and about 25% were PWNe. In this chapter I discuss the basics of non-thermal gamma-ray production processes and briefly discuss properties of pulsars and PWNe.

### 2.1 Non-thermal Gamma-ray Production Processes

Non-thermal gamma-rays are produced by several processes. Sometimes those processes are divided into two categories based on the types of high energy particles which produced gamma-rays: leptonic mechanisms and hadronic mechanisms. In leptonic mechanisms high energy leptons produce the gamma-rays, and in hadronic mechanisms high energy hadrons produce the gamma-rays. Sometimes these processes are divided based on their interactions: particle-field interaction mechanisms and particle-matter interaction mechanisms. In

the particle-field interaction mechanisms, the gamma-rays are produced by the interactions between particles and fields, such as synchrotron radiation of electrons in the presence of magnetic fields. In the particle-matter interaction mechanisms, the gamma-rays are produced by the interactions between particles and the matter in the ambient field, such as bremsstrahlung. In the very high energy gamma-ray band the most dominant radiation mechanisms are synchrotron radiation, curvature radiation, inverse compton radiation, relativistic bremsstrahlung, and  $\pi^0$  decays.

### 2.1.1 Synchrotron Radiation

Synchrotron radiation is created when electrons accelerate radially<sup>1</sup>. An electron can be accelerated radially and move in a helical path when it moves with a non zero pitch angle<sup>2</sup> and a non-zero velocity component along the magnetic field. In such motions, accelerating electrons emit photons within an angle of  $\theta \sim m_e c^2 / E$  [Gustavo E.R. and K.S. Cheng (2004)] of its velocity, where  $m_e$  is the electron mass,  $c$  is the speed of light and  $E$  is the energy of the electron. The total energy rate loss by synchrotron radiation generated by a helically moving electron in a magnetic field,  $B$ , can be written as [Gustavo E.R. and K.S. Cheng (2004)],

$$\left(\frac{dE_e}{dt}\right) = -\frac{2}{3}c \left(\frac{e^2}{m_e c^2}\right)^2 B_{\perp}^2 \gamma^2, \quad (2.1)$$

where  $\gamma$  is the Lorentz factor of the electron,  $B_{\perp} = B \sin \theta$ , and  $\theta$  is the pitch angle. By averaging this over an isotropic pitch angle distribution, the average energy rate for all pitch

---

<sup>1</sup>Other charged particles also produce radiation when they accelerate radially, but the mass dependence of equation 2.1 shows that radiation by  $e^+$  and  $e^-$  are much stronger than more massive particles.

<sup>2</sup>Pitch angle is the angle between the velocity vector of the particle and the magnetic field.

angles can be written as:

$$\left(\frac{dE_e}{dt}\right) = 0.66 \times 10^3 B^2 \gamma^2 \text{eV/s}, \quad (2.2)$$

where B is measured in Gauss. If the electron distribution is homogeneous and follows an isotropic power-law distribution with power-law index p,

$$N_e(E_e) dE_e = K_e E_e^{-p} dE_e, \quad (2.3)$$

in a random magnetic field, then the resulting spectrum of the synchrotron radiation can be written as:

$$I(E_\gamma) = a(p) \frac{e^3}{m_e c^2} \left(\frac{3e}{4\pi m_e^3 c^5}\right)^{(p-1)/2} B^{(p+1)/2} K_e L E_\gamma^{-(p-1)/2}, \quad (2.4)$$

where  $L$  is the characteristic size of the emitting region,  $a(p)$  is 0.147, 0.103, 0.0852, and 0.0742 for  $p = 1.5, 2, 2.5,$  and  $3,$  respectively. The spectrum of the synchrotron radiation is a power-law with the power-law index  $\alpha = (p - 1)/2$ .

## 2.1.2 Curvature Radiation

Curvature radiation is created when charged particles move along curved field lines. In the presence of strong magnetic fields, charged particles tend to move along the field lines. If the curvature radius ( $R_C$ ) of the magnetic field lines is small, particles moving along the field lines will radiate photons. The energy loss rate by curvature radiation from an electron moving on a magnetic field line with a curvature radius  $R_C$  and zero pitch angle, can be

written as [Gustavo E.R. and K.S. Cheng (2004)],

$$\left(\frac{dE}{dt}\right) = -\frac{2}{3} \frac{ce^2\gamma^4}{R_c^2}, \quad (2.5)$$

where  $\gamma$  is the Lorentz factor of the electron. When the pitch angle is zero synchrotron radiation losses become zero. However, electrons can move in curved magnetic fields with non zero pitch angles. The critical pitch angle is defined by equating the synchrotron and the curvature radiation losses, which yields:

$$\sin \theta_{cr} = \frac{\gamma m_e c^2}{e B R_c}, \quad (2.6)$$

where  $\theta_{cr}$  is the critical pitch angle.

Curvature radiation becomes the dominant radiation process when the pitch angle is much smaller than the critical pitch angle. However, the synchrotron radiation losses become significant when the pitch angle is of order of the critical pitch angle. Therefore, in this case the total radiation losses can not be explained by either synchrotron radiation or curvature radiation. The radiation losses when the pitch angle is on order of the critical pitch angle is explained by the synchro-curvature radiation, which is a mixture of the two processes (eg. [Cheng & Zhang(1996), Zhang & Yuan(1998), Harko & Cheng(2002)]).

### 2.1.3 Inverse Compton Radiation

Relativistic electrons can be scattered off low energy photons by transferring the energy of the relativistic electrons to the low energy photons. This process goes in the inverse direction of Compton scattering (where high energy photons scatter off low energy electrons

by transferring energy to the electrons). Therefore, this process is called Inverse Compton scattering (IC scattering). When  $E_e E_{ph} \gg (m_e c^2)^2$  the electron can transfer most of its energy to the photon,  $E_\gamma \sim E_e$ , where  $E_{ph}$  is the average energy of the target photons and  $E_\gamma$  is the average energy of the photons after the IC scattering..

Target photons for IC scattering can come from multiple sources, such as microwave photons from the cosmic microwave background, ambient photons from thermal emissions, or high energy photons from synchrotron radiation. One can consider a special case where target electrons for IC scattering come from synchrotron radiation of the same electron population that produces the IC scattering. This special case is called Synchrotron Self-Compton (SSC) scattering. In this scenario the radiation from the synchrotron radiation and from the IC scattering are highly correlated. The spectrum of the inverse compton component is expected to be similar to the synchrotron component [Costamante & Ghisellini(2002)].

## 2.2 Pulsars

Pulsars are highly magnetized, rotating neutron stars that emit two beams of electromagnetic photons in opposite directions. A pulsar can only be seen when a beam is pointing towards the observer. Therefore, the observer sees the pulsar as a pulsating star. The first pulsar was accidentally discovered by Jocelyn Bell Burnell and Antony Hewish on November 28, 1967 [Hewish et al.(1968)]. Since then more than 2000 radio pulsars<sup>3</sup> has been discovered, and the recently published second Fermi-LAT pulsar catalog observed 117 pulsars in the GeV energy band [Abdo et al.(2013)].

---

<sup>3</sup>According to the ATNF online catalog <http://www.atnf.csiro.au/people/pulsar/psrcat/>

## 2.2.1 Properties of Neutron Stars

The composition of neutron stars was predicted in 1939 by Oppenheimer and Volkov, 28 years before the discovery of the first pulsar [Oppenheimer & Volkoff(1939)]. A neutron star is created as a result of the core collapse of a massive star during a supernova. The resulting neutron star retains most of its angular momentum. However, the radius of the star is sharply reduced. Therefore, the angular velocity is sharply increased and the density of the neutron star becomes high. The equation of state for neutron stars, which consist of highly compressed matter, remains uncertain, and the predicted maximum neutron star mass is  $\sim 2M_{\odot}$  [Lattimer & Prakash(2001)]. Measurements of neutron star masses have been found to typically be  $\sim 1.4M_{\odot}$  [Lorimer & Kramer(2012)].

The possible range of radii for neutron stars can be derived using theoretical arguments. The theoretically possible minimum radius for a neutron star is derived based on arguments that the speed of sound should be less than the speed of light in a neutron star, and that the equation of state should have a smooth transition from low to high densities [Lattimer et al.(1990), Glendenning(1992)],

$$R_{min} \simeq 1.5R_s = \frac{3GM}{c^2} = 6.2km \left( \frac{M}{1.4M_{\odot}} \right), \quad (2.7)$$

where  $R_s$  is the Schwarzschild radius. The theoretically possible maximum radius is derived based on the argument that the neutron star has to be stable against break-up due to centrifugal forces leading to,

$$R_{max} \simeq \left( \frac{GMP^2}{4\pi} \right)^{1/3} = 16.8km \left( \frac{M}{1.4M_{\odot}} \right)^{1/3} \left( \frac{P}{ms} \right)^{2/3}, \quad (2.8)$$

where  $P$  is the period of rotation.

Neutron stars are nearly spherical objects. Therefore, the momentum of inertia can be calculated using  $I = kMR^2$ . For a sphere of uniform density  $k = 0.40$ . However, neutron stars are not perfect spheres with uniform density. Therefore, the exact value of  $k$  depends on the density profile, which depends on the equation of state. The typical range of  $k$  predicted by most models is  $0.3 < k < 0.45$  for a mass/radius range of  $0.1M_{\odot}\text{km}^{-1} < M/R < 0.2M_{\odot}\text{km}^{-1}$  [Lorimer & Kramer(2012)]. Most practical calculations adopt  $M = 1.4M_{\odot}$ ,  $R = 10 \text{ km}$  and  $k = 0.4$  to calculate  $I$ , so  $I = 10^{38} \text{ kg m}^2$ .

## 2.2.2 Pulsar Spin Evolution

It has been observed that pulsar periods increase with time,  $\dot{P} = \frac{dP}{dt} > 0$ . Pulsar periods are increasing because of the loss of rotational kinetic energy. Therefore,  $\dot{P}$  can be related to the rate of loss of rotational kinetic energy,

$$\dot{E} \equiv -\frac{dE_{rot}}{dt} = -\frac{d(I\Omega^2/2)}{dt} = -I\Omega\dot{\Omega} = 4\pi^2 I \dot{P} P^{-3}, \quad (2.9)$$

where  $\Omega = 2\pi/P$ . The  $\dot{E}$  of a pulsar is called the spin-down luminosity, which represents the total rate of energy output of the neutron star, by neglecting changes of the energy due to changes in the magnetic field. Equation 2.9 can be rewritten using the typical value for the momentum of inertia,  $I = 10^{38} \text{ kg m}^2$ ,

$$\dot{E} \simeq 3.95 \times 10^{31} \text{ erg s}^{-1} \left( \frac{\dot{P}}{10^{-15}} \right) \left( \frac{P}{\text{s}} \right)^{-3}. \quad (2.10)$$

A small fraction of the  $\dot{E}$  is converted into electromagnetic radiation, and to a wind of electrons and positrons flowing out from the pulsar. The bulk of the  $\dot{E}$  converts into magnetic dipole radiation.

### 2.2.3 Spin-down Luminosity Evolution

A pulsar is a rotating magnetic dipole<sup>4</sup>, which radiates an electromagnetic wave at its rotational frequency,

$$\dot{E}_{dipole} = \frac{2}{3c^3} |\mathbf{m}|^2 \Omega^4 \sin^2 \alpha, \quad (2.11)$$

where  $\mathbf{m}$  is the magnetic moment and  $\alpha$  is the angle between the magnetic moment and the spin axis. Since the bulk of the  $\dot{E}$  converts into the magnetic dipole radiation,  $\dot{E}$  is approximately equal to  $\dot{E}_{dipole}$ . This equality yields:

$$\dot{\Omega} = - \left( \frac{2|\mathbf{m}|^2 \sin^2 \alpha}{3Ic^3} \right) \Omega^3. \quad (2.12)$$

This equation can be more generally expressed as follows:

$$\dot{\Omega} = -K\Omega^n, \quad (2.13)$$

where  $K$  is a constant and  $n$  is the braking index. The braking index can be determined by taking the second derivative of  $\Omega$  and eliminating  $K$ ,

$$n = \frac{\Omega \ddot{\Omega}}{\dot{\Omega}^2}. \quad (2.14)$$

---

<sup>4</sup>Assuming the magnetic field is constant



The braking index of several pulsars were measured and found to have a typical range of 1.4–2.9. These measurements indicate that the assumption of  $n = 3$  is usually not correct.

The theoretical expectation of the rotational energy loss rate of a neutron star is a function of the braking index [Mattana et al.(2009)],

$$\dot{E}(t) = \frac{\dot{E}_0}{(1 + t/t_{dec})^n}, \quad (2.15)$$

where  $\dot{E}_0$  is the  $\dot{E}$  at the time of the pulsar birth,  $t_{dec}$  is a characteristic decay time,  $t$  is the time elapsed since the pulsar's birth, and  $n$  is the braking index.

## 2.2.4 Characteristic Age of a Pulsar

The generalized model for angular velocity evolution that is shown in Equation 2.13 can be expressed in terms of the pulsar period ( $P$ ) and braking index ( $n$ ),

$$\dot{P} = kP^{2-n} \quad (2.16)$$

This is a first-order differential equation, which can be integrated assuming  $k$  is a constant and  $n \neq 1$ ,

$$T = \frac{P}{(n-1)\dot{P}} \left[ 1 - \left( \frac{P_0}{P} \right)^{n-1} \right], \quad (2.17)$$

where  $T$  is the pulsar age and  $P_0$  is the pulsar period at birth. This equation can be rewritten under the assumptions that the current pulsar spin period is much larger than that at the birth of the pulsar ( $P_0 \ll P$ ) and the dominant spin-down is due to magnetic

dipole radiation ( $n = 3$ ),

$$\tau_c = \frac{P}{2\dot{P}}, \quad (2.18)$$

where  $\tau_c$  is the characteristic age. Due to these assumptions  $\tau_c$  does not necessarily estimate the correct age of a pulsar. For example the characteristic age of the Crab pulsar is 1240 years, compared to its known age of 950 years. Another example is the pulsar J0205+6449m which was born in the historical supernova of AD 1181, but has the characteristic age of 5370 years. Therefore, characteristic age cannot be considered a reliable parameter to estimate the real age of a pulsar, and it should be interpreted with some care.

### 2.2.5 Pulsar Magnetosphere

The structure of a pulsar magnetosphere and its acceleration processes can not be solved analytically in a closed form [Lorimer & Kramer(2012)]. Therefore, numerical simulations are used to study the structure and the acceleration processes of pulsar magnetospheres. A simplistic toy model for a neutron star and its magnetosphere is shown in Figure 2.1, where the magnetosphere is the region surrounding the neutron star in which its magnetic field is the predominant effective magnetic field. In a simplistic scenario a neutron star can be considered as a superconducting object. In the case of a pulsar neutron star it is a spinning magnetic dipole. This conducting and spinning magnetic dipole acts as a uni-polar generator, which creates an electric quadrupole field around the neutron star. The electric field component parallel to the magnetic field strips the electrons from the pulsar surface and accelerates them along the magnetic field lines. These accelerated electrons produce curvature radiation. Due to the geometry of the magnetic field, the photons from curvature radiation create two photon beams along the magnetic field axis. The photons from curvature

radiation produce secondary electron-positron pairs (by interacting with the strong magnetic field), which are also accelerated along the magnetic field lines by the electric field.

Co-rotating magnetic field lines are closed loops near the rotating neutron star. However, the co-rotating magnetic field lines become open as they cross the light cylinder. The light cylinder is a co-rotating imaginary cylinder, centered on the pulsar, aligned with the rotational axis, and with a surface speed equal to the speed of light. Electrons and positrons that accelerate along the open field lines create an electron-positron wind flowing out from the pulsar. This wind is called the pulsar wind.

Different acceleration mechanisms require different conditions to accelerate electrons and positrons to very high energies. Some models expect large plasma densities, which are not possible to generate on the superconducting neutron star. These models predict regions in the magnetosphere called gap regions, such as: Polar cap, Outer gap and Slot gap. The Polar cap is the region where open field lines meet the neutron star surface, the Outer gap is the region where  $\Omega \cdot B = 0$ , and the Slot Gap is the edge of the open field region from the neutron star surface to near the light cylinder. These gap regions are shown in the schematic diagram in Figure: 2.2.

## 2.3 Pulsar Wind Nebulae

A Pulsar Wind Nebula (PWN) is a nebula that is powered by the ultra-relativistic pulsar wind of a pulsar. The pulsar wind flows outward from the pulsar along its magnetic field lines. This wind is composed from ultra relativistic electrons and positrons. The total injection rate of electrons and positrons to the PWN by its associated pulsar can be written as [Mattana et al.(2009)]:

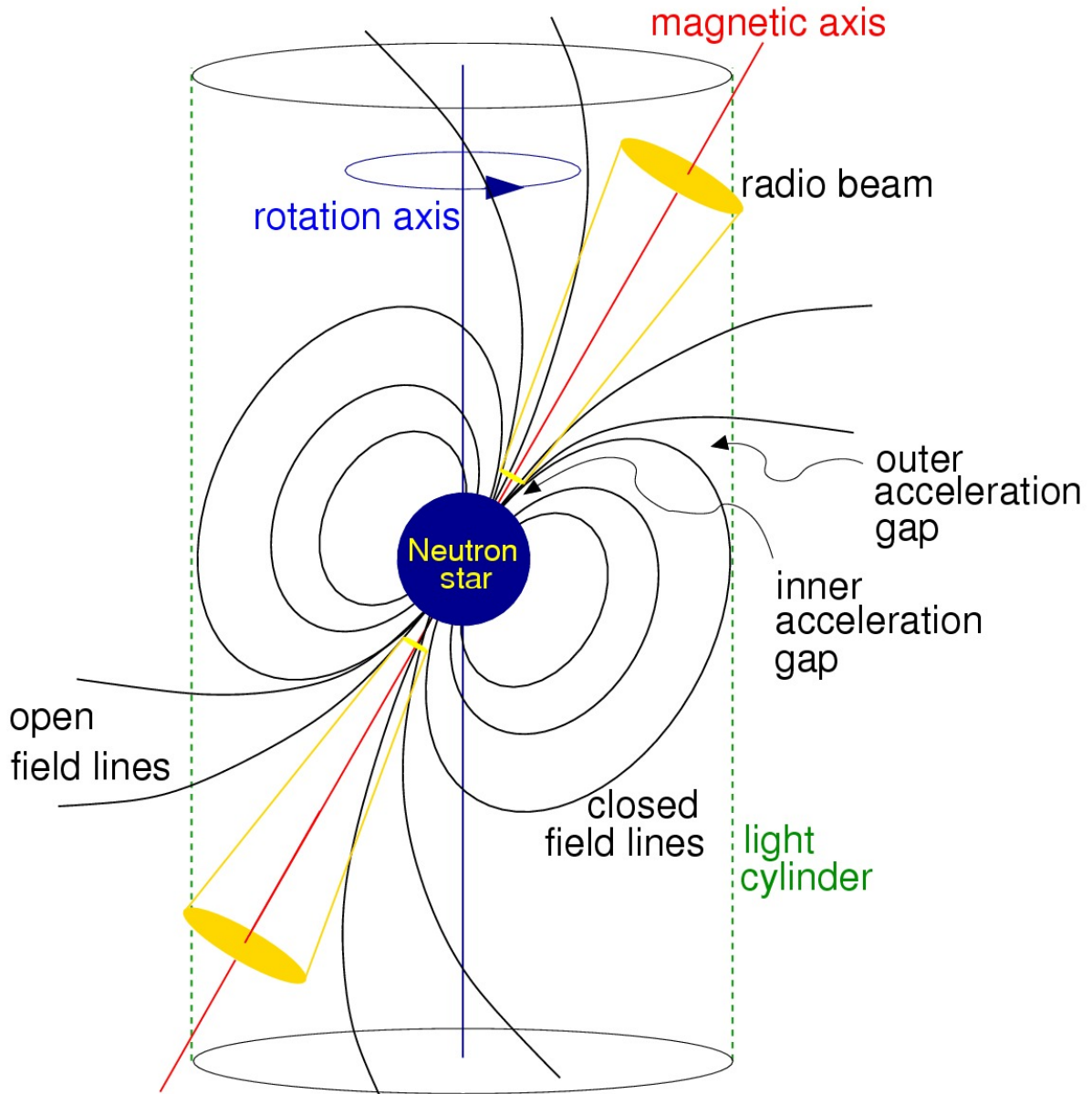


Figure 2.1: A simplistic toy model for a neutron star and its magnetic sphere. Reference: Handbook of Pulsar Astronomy by Lorimer and Kramer.

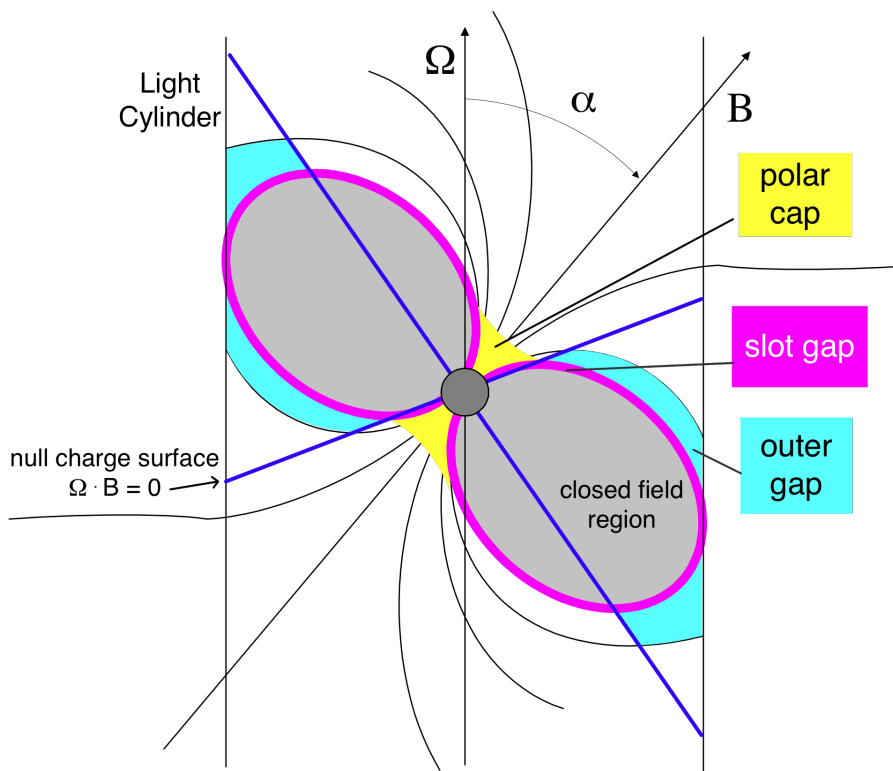


Figure 2.2: Pulsar Gap regions in the pulsar magnetosphere are marked in different colors. Reference: Alice Harding’s presentation “Gamma-Ray Pulsars Theory and Modeling” at Fermi Summer School 2011.

$$\dot{N} = \frac{\dot{E}}{\Gamma_w m_e c^2 (1 + \sigma)}, \quad (2.19)$$

where  $\Gamma_w$  is the bulk Lorentz factor of the wind and  $\sigma$  sets the fraction of the spin-down luminosity ( $\dot{E}$ ) converted into the kinetic energy of the wind. Note that only a very small fraction of the  $\dot{E}$  is converted into the kinetic energy of the wind, therefore  $\sigma \gg 1$ . To simplify the math, in this discussion  $\Gamma_w$  was assumed to be a constant. As I described in Section 2.2.3,  $\dot{E}$  of a pulsar decreases with time. Therefore, the value of  $\dot{N}$  is proportional to the value of the spin-down luminosity,  $\dot{E}(t)$ , at a given time.

When this wind meets the nebula it creates a standing shock, which makes non-zero pitch angles (pitch angle is the angle between the magnetic field and the velocity of the particle). These particles with non-zero pitch angles lose their energy by synchrotron radiation. The electrons also create very high energy gamma-ray photons by Inverse Compton scattering. The cooling time of electrons that cool by Inverse Compton scattering is typically larger than the age of young pulsars [Mattana et al.(2009)]. Therefore, the electrons that accumulated from the birth of a PWN could still produce TeV photons by IC scattering. The total number of electrons that accumulated in the PWN can be written as:

$$n_u \propto \int_0^\tau \dot{E}(t) dt, \quad (2.20)$$

where  $n_u$  is the number of accumulated electrons and  $\tau$  is the pulsar's age.  $\dot{E}(t)$  can be substituted from Equation 2.15, giving:

$$n_u \propto \int_0^\tau \frac{\dot{E}_o}{(1 + t/t_{dec})^{(n+1)/(n-1)}} dt. \quad (2.21)$$

In the case where the dominant spin-down losses are due to magnetic dipole radiation ( $n = 3$ ),

$$n_u \propto \dot{E}_o t_{dec} \left( \frac{\tau}{\tau + t_{dec}} \right). \quad (2.22)$$

Typically  $\tau \gg t_{dec}$  [Mattana et al.(2009)], which yields:

$$n_u(E, t) \propto \dot{E}_o t_{dec}. \quad (2.23)$$

Since the luminosity is roughly proportional to the population of the radiating particles, luminosity is also proportional to  $\dot{E}_o t_{dec}$ . Therefore, one can expect that for PWNe  $L_{TeV} \propto \dot{E}^0$  (PWNe TeV luminosity is proportional to the spin-down luminosity to the power of zero).

# Chapter 3

## The Milagro Observatory

The Milagro gamma-ray observatory was a ground-based water Cherenkov detector located near Los Alamos, New Mexico, USA at latitude  $35.9^\circ$  north, longitude  $106.7^\circ$  west and altitude 2630 m. Milagro was operated from 2001 to 2008 and was sensitive to gamma-ray initiated EASs from a few hundred GeV to  $\sim 100$  TeV. Its high duty cycle ( $> 90\%$ ) and wide field of view ( $\sim 2\text{sr}$ ) made it an excellent instrument to survey the northern hemisphere ( $-7^\circ < \text{DEC} < 80^\circ$ ). The Milagro archived data set is an ideal place to study phenomena of gamma-ray sources as well as hadronic cosmic rays. This chapter describes the working principles, electronics, event reconstruction and background subtraction algorithm of Milagro.

### 3.1 Milagro Detector

The Milagro detector consisted of a light tight pond of 80 m (l)  $\times$  60 m (w)  $\times$  8 m (h) filled with 24 million liters of ultra purified water surrounded by 175 small outrigger tanks. The area of the Milagro detector including the outrigger tanks was about  $40,000\text{ m}^2$ . Figure 3.1





Figure 3.1: An aerial photograph of the Milagro detector. The pond is at the center of this photograph and red circles mark the locations of the outrigger tanks.

shows an aerial photograph of Milagro and the distribution of the outrigger tanks are marked with red circles. Figure 3.2 shows some outrigger tanks. The main pond was instrumented with 723 Photo Multiplier Tubes (PMTs) arranged in two layers and each outrigger tank was instrumented with a single PMT.

### 3.1.1 The Main Pond

A photograph of the inside of the Milagro pond is shown in Figure 3.3. This photograph shows the two layers of the PMTs. The top layer, called the Air Shower (AS) layer is placed 1.5 m below the water surface and consists of 450 PMTs. The bottom layer, called the Muon (MU) layer is placed 6 m below the water surface and consists of 273 PMTs. The PMTs in each of these layers were arranged on a  $2.8 \text{ m} \times 2.8 \text{ m}$  grid and the MU layer is



Figure 3.2: This picture was taken during the cleaning process of the Milagro site a few years after the Milagro shutdown. The Milagro water pond is visible on the left side of this picture and several outrigger tanks are visible around the pond.

horizontally shifted by a half grid space from the AS layer. A schematic side view of this PMT arrangement is shown in Figure 3.4.

When an EAS front lands on the Milagro pond, the EAS's relativistic electrons and positrons travel through the water making Cherenkov light in the water that can be detected by PMTs. In the meantime, the secondary photons generated in an EAS also enter the pond. Since the AS layer is placed 1.5 m below the water surface (equivalent to 4 radiation lengths) these gamma-rays can cascade into electron-positron pairs before reaching this layer. These tertiary electron-positron pairs are also capable of producing Cherenkov light. The secondary showering increases the density of Cherenkov photons inside the water, which increased the sensitivity of Milagro. Since the MU layer is placed 6 m under the water surface (16 radiation lengths of water) the energy of electrons and positrons are not enough to reach that depth. However, muons and hadrons that mostly constitute hadronic showers (showers that initiated from a highly energetic hadronic cosmic particle) can easily penetrate to this depth. Therefore, the ratio between the number of AS layer PMT hits to the number of MU layer PMT hits gives a hint about the origin of the shower. This property was used to reject the background of hadronic generated showers. Aous Ahmad Abdo [Abdo(2007)] was able to identify a more efficient method to reject the hadronically generated showers by combining the AS layer, MU layer and OR tanks.

The PMTs used both in the main water pond and in the outrigger tanks were 20 cm Hamamatsu #R5912SEL with a custom water-proof base made from polyvinyl chloride (PVC). The base protects the electronic connections of the PMT, which carry the high voltage to the PMT and the PMT pulses back to the front-end electronics. As can be seen in Figure 3.3, each PMT is surrounded by a conical collar. The inside of this collar is white

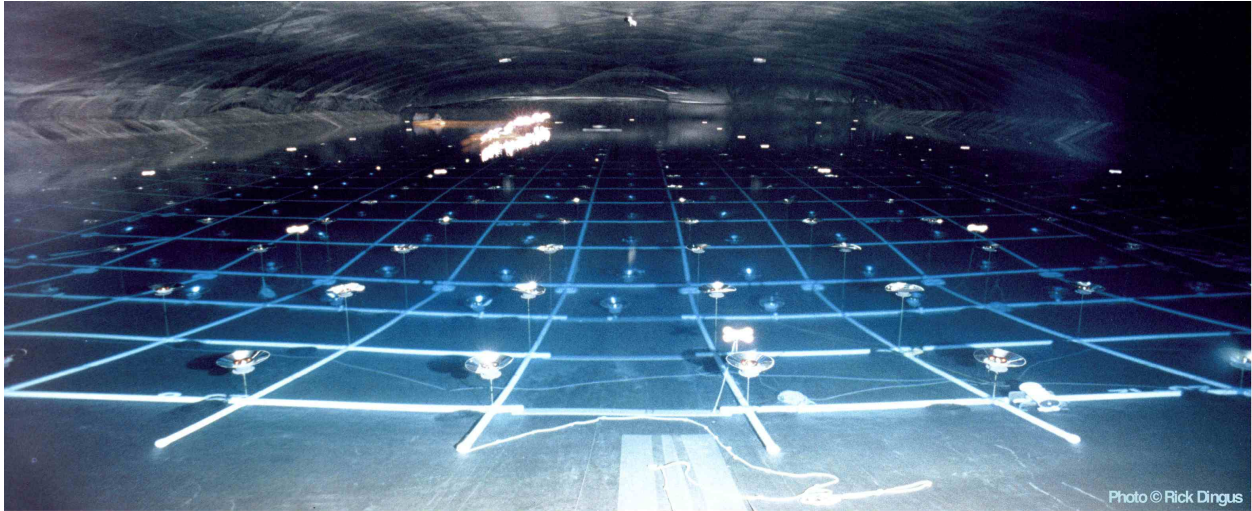


Figure 3.3: This is an inside view of the Milagro pond. Two layers of PMTs are visible in this picture.

and outside is black. The white interior increased the light collection area of each PMT and the black exterior blocked the Cherenkov light generated from horizontally traveling muons.

In order to detect water Cherenkov light using PMTs, the pond had to be dark and the water ultra-pure. Darkness inside the pond was accomplished by covering the pond using a 1 mm thick polypropylene cover. The top surface of the cover is painted with a highly reflective paint to reduce the inside temperature during the day time. The quality of water inside the pond was maintained by constantly recirculating water at a rate of 200 gallons per minute. During the re-circulation process, the water went through a set of filters : a charcoal filter, a 10  $\mu\text{m}$  filter, a 1  $\mu\text{m}$  filter, a carbon filter, a 0.2  $\mu\text{m}$  filter<sup>1</sup> and finally through UV lamps to prevent any biological growth.

---

<sup>1</sup>This filter was removed after the second year.

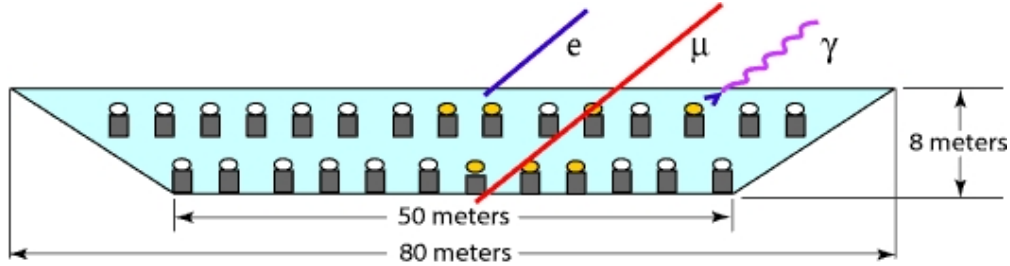


Figure 3.4: This schematic diagram shows the PMT placement inside the Milagro pond. The first layer, the Air Shower Layer, was placed 1.5 m below the water surface. The second layer, the Muon layer, was placed 6 m below the water surface.

### 3.1.2 The Outrigger Array

The outrigger array consisted of 175 tanks of 2.4 m in diameter and 1 m in height. Each tank was filled with ultra-purified water and instrumented with a PMT pointing down. These outrigger tanks were unevenly spread across an area of  $40,000 \text{ m}^2$ . This array allowed for more accurate determination of the shower core location and its arrival direction.

## 3.2 Front-end Electronics and Time to Digital Converter

The Milagro front-end electronics were designed to digitize the analog signal outputs coming from the PMTs. This task was accomplished using two types of custom electronic cards, called analog and digital front-end Boards, and a commercial Time to Digital Converter (TDC). Each analog and digital card pair was connected to 16 PMTs.

The functional block diagram of one channel of the analog cards is shown in Figure 3.5. The input of each channel is the analog signal output coming from a PMT. Then the input signal splits into two and goes to two transconductance amplifiers (where output current is proportional to the amplitude of the input signal) with two different gains. The output of

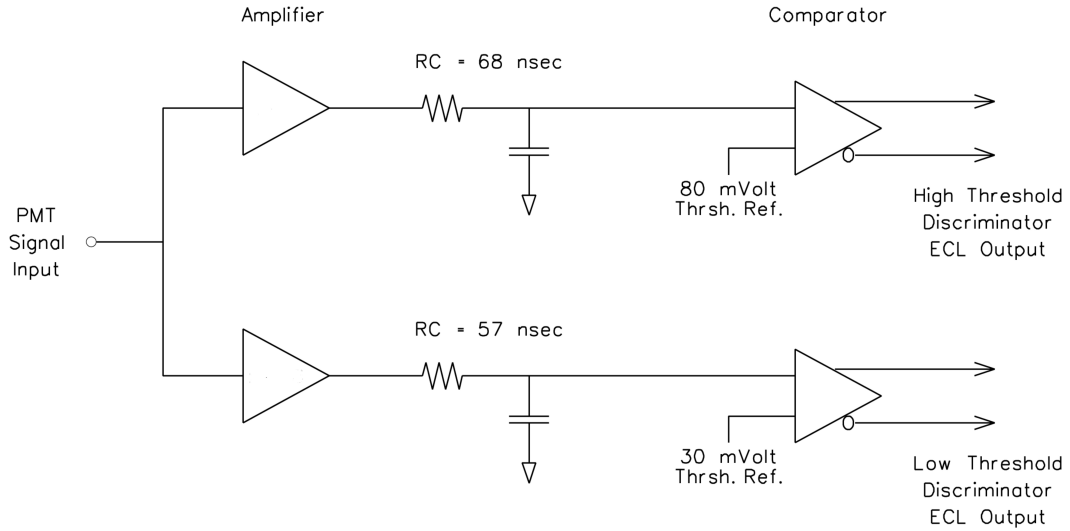


Figure 3.5: Functional block diagram of the Milagro front-end analog electronic board.

each transconductance amplifier is then sent to an RC(Resistor-Capacitor) integrator. The voltage across the RC integrator's capacitor can be written as:

$$V_C \propto \int_0^t V_{in} dt. \quad (3.1)$$

Each  $V_C$  is then sent to one of two discriminators with a preset threshold voltage. One discriminator has a high threshold voltage (of 80 mV) and the other one has a lower threshold voltage (of 30 mV). Whenever the PMT pulse crosses either of these thresholds the discriminator outputs produce an edge as shown in Figure 3.6. Smaller pulses create an edge pair only at the low threshold discriminator output and pulses with larger amplitudes create edge pairs at both discriminator outputs. The width of each digital pulse is equal to the time spent over the preset threshold. Therefore these signals are called Time Over Threshold (TOT) signals.

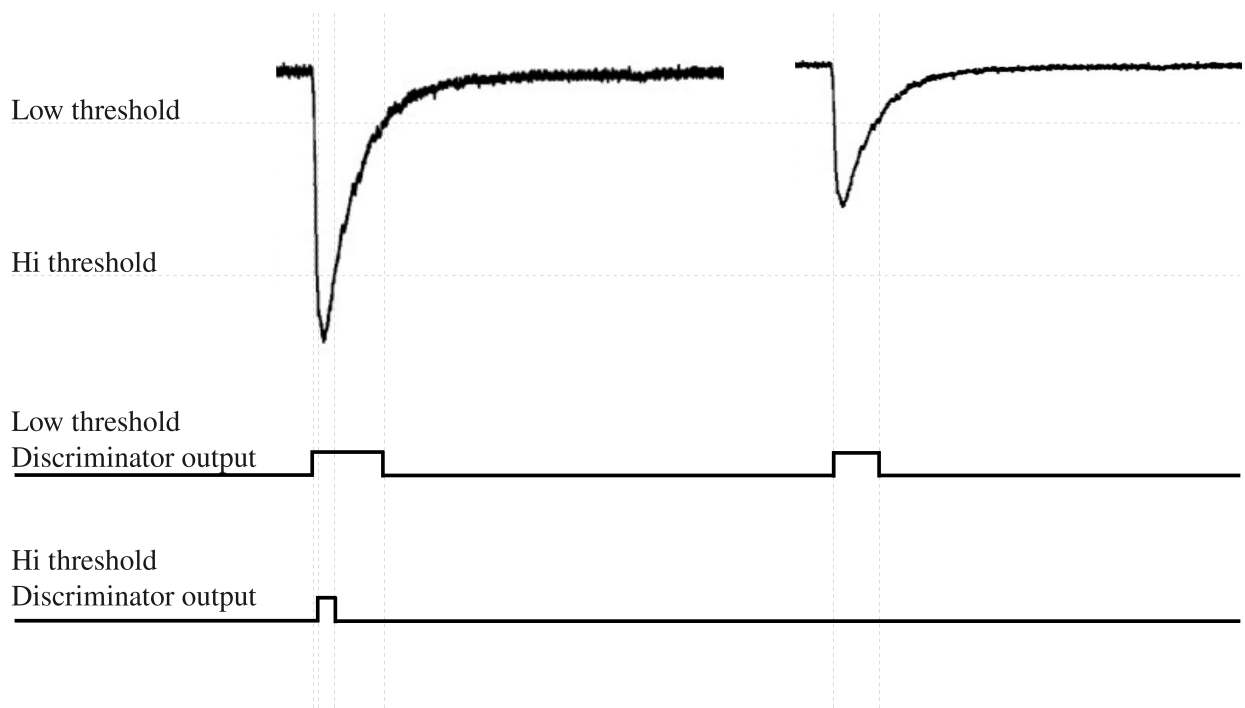


Figure 3.6: The two analog signals shown at the top of this figure represent the shape of a typical PMT output signal. The one on the left has a high amplitude and the one on the right has a lower amplitude. The two digital signals shown at the bottom are the outputs of the two discriminators.

The TOT signals are then sent to digital cards, where two discriminator output signals are combined to make one signal. Figure 3.7 shows the functional block diagram of the digital cards. The basic functionality shown in this figure can be summarized in several steps.

1. Delay the high TOT signal by 20 ns.
2. Invert the high TOT signal.
3. Add the inverted signal to the low TOT signal.

The result of this process is a four edge event with the edge 1 to edge 4 distance equal to the low TOT pulse width, and the edge 2 to edge 3 distance equal to the high TOT pulse width. If the signal is too small to cross the high threshold, it would produce a two edge event.

The next step is to convert these digital signals to a number that can be read by a computer. This was done using LeCroy FASTBUS Time to Digital Convertors (TDCs), that produce an integer proportional to the TOT values. Since these TOT values are a function of the PMT pulse size, these digital numbers can then be calibrated to get the charge generated by the PMTs, under the assumption that all PMT signals have a similar shape.

### **3.3 Trigger**

A better way to have operated the Milagro data acquisition system would have been to record the data continuously and throw out the background events after a high-level data analysis. However, this was not possible to do at the time due to technical limitations at that time. Instead the Milagro data acquisition system only accepted events that fulfilled a



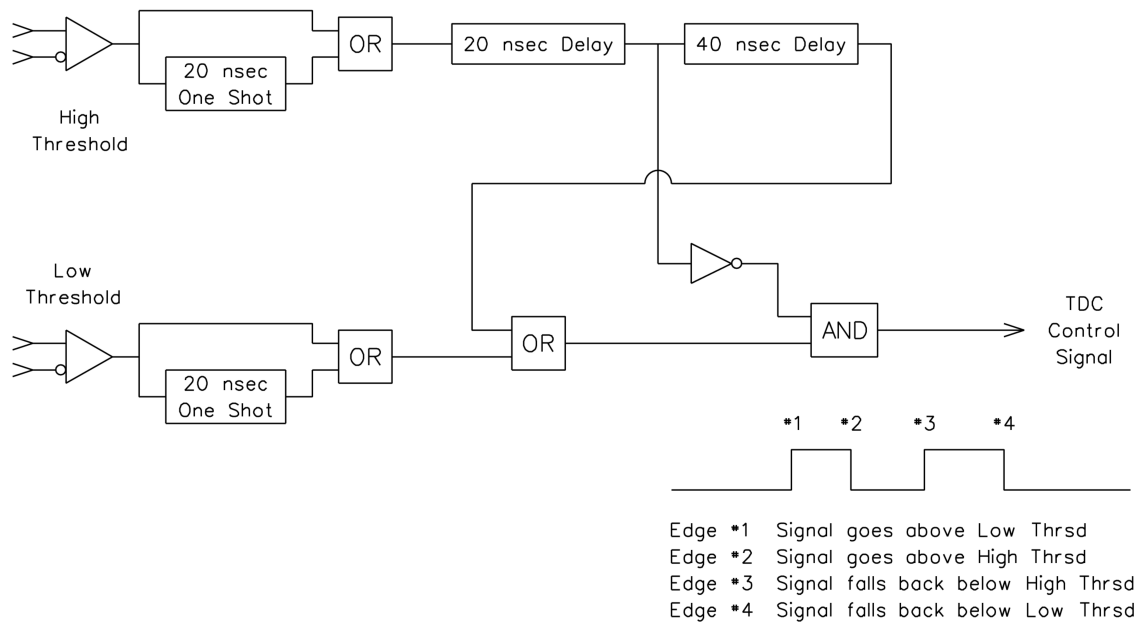


Figure 3.7: Functional block diagram of the Milagro front-end digital electronic board.

trigger condition, then the triggered raw data was saved to Digital Linear Tapes (DLTs). At the beginning of the Milagro operation, the trigger condition was the number of PMTs fired during a given time period, which is called the simple multiplicity trigger (SMT). The trigger conditions of the SMT were changed from time to time but in general the trigger condition was  $\sim 60$  AS layer PMT hits within a 200 ns time window. Lowering this threshold would have increased the sensitivity to low energy gamma-rays, which is physically motivated because of the low flux at very high energies. However, lowering the threshold would have increased the data rate (typical trigger rate was  $\sim 2\text{kHz}$ ), which could not be handled by the data acquisition system.

The dominant background events that create low multiplicities of PMT hits are high energy muons that travel nearly horizontal with respect to the Milagro pond. An alternative way to identify such events is by their time profile. When an air shower lands on the detector the shower front sweeps along the pond faster than a muons travel through water. Therefore muon events can be identified by using their rise time parameter, which is the time interval within which 10% to 90% of the hits occur for a given time. The rise time parameter is larger for muon events compared to events generated by air showers.

The calculation of the rise time parameter was not as easy as the calculation of the multiplicity. Therefore, Milagro designed a customized piece of electronics with programmable logic to perform this task. This device was used for triggers for a while, but had to be removed after it failed.

## 3.4 Reconstruction

The triggered raw data consists of a collection of edge times. The next step is to reconstruct the properties of each shower, such as its core location and incidence angle, from these edge times.

### 3.4.1 Shower Core Location Reconstruction

The shower core is the location where the primary particle would hit the Milagro detector if there were no interactions with the atmosphere. The particle density of a shower is highest at the core location and the core contains the highest energy particles. Therefore the number of photoelectrons (PEs) recorded by the PMTs are highest at the shower core. This property was used in Milagro to identify shower cores, and a conceptual diagram is shown in Figure 3.8. Over Milagro's life time several algorithms were used to identify the shower core location.

The simplest algorithm used in Milagro was the center of mass fitter, which calculates the core location using the weighted sum of the PMTs.

$$x_{core} = \frac{\sum_i \sqrt{PE_i} \times x_i}{\sum_i \sqrt{PE_i}} \quad (3.2)$$

$$y_{core} = \frac{\sum_i \sqrt{PE_i} \times y_i}{\sum_i \sqrt{PE_i}} \quad (3.3)$$

In Equation 3.2 and 3.3,  $(x_{core}, y_{core})$  are the Cartesian coordinates of the shower core location,  $(x_i, y_i)$  are the Cartesian coordinates of the PMTs and  $PE_i$  is the number of PEs detected by the PMT at  $(x_i, y_i)$ . If the shower core location was likely to be on the pond only the PMTs in the pond were used, but if it was likely to be off the pond only the PMTs in the outrigger tanks were used. The likelihood of the core being on or off the

pond was calculated using the ratio of the number of outrigger hits to the number of AS layer PMT hits.

The core fitter algorithm used later in Milagro was based on a 2-D Gaussian least-squares fit. The underlying concept of this algorithm is the same as the previous algorithm. It fits a 2-D Gaussian function by considering  $x_i$  and  $y_i$  as the two dimensions and the number of PEs detected by each PMT as the amplitude. The peak of the Gaussian distribution is the core location.

These simplified versions of the algorithms explained here assume that EAS fronts are flat and have a uniform thickness. However, EAS fronts are not flat and are thin near the shower core, compared to the edge. Therefore the angle reconstruction process makes corrections to remove these effects.

### 3.4.2 Incidence Angle Reconstruction

The incidence angle of an EAS is reconstructed using the timing profile of the PMT hits. This concept is easy to understand using the two dimensional example shown in Figure 3.9. When an EAS front lands on the ground with a non-zero zenith angle, one end of the shower lands on the detector earlier than the other, and then the shower sweeps through the detector. The time that a shower takes to travel from one PMT to the other can be written as,

$$\delta t = \frac{L \sin \theta}{V}, \quad (3.4)$$

where  $\delta t$  is the relative time that the shower takes to travel from one PMT to the other,  $L$  is the gap between PMTs,  $\theta$  is the incidence angle and  $V$  is the velocity of the shower front. Since shower fronts travel with a speed close to the speed of light, this equation can

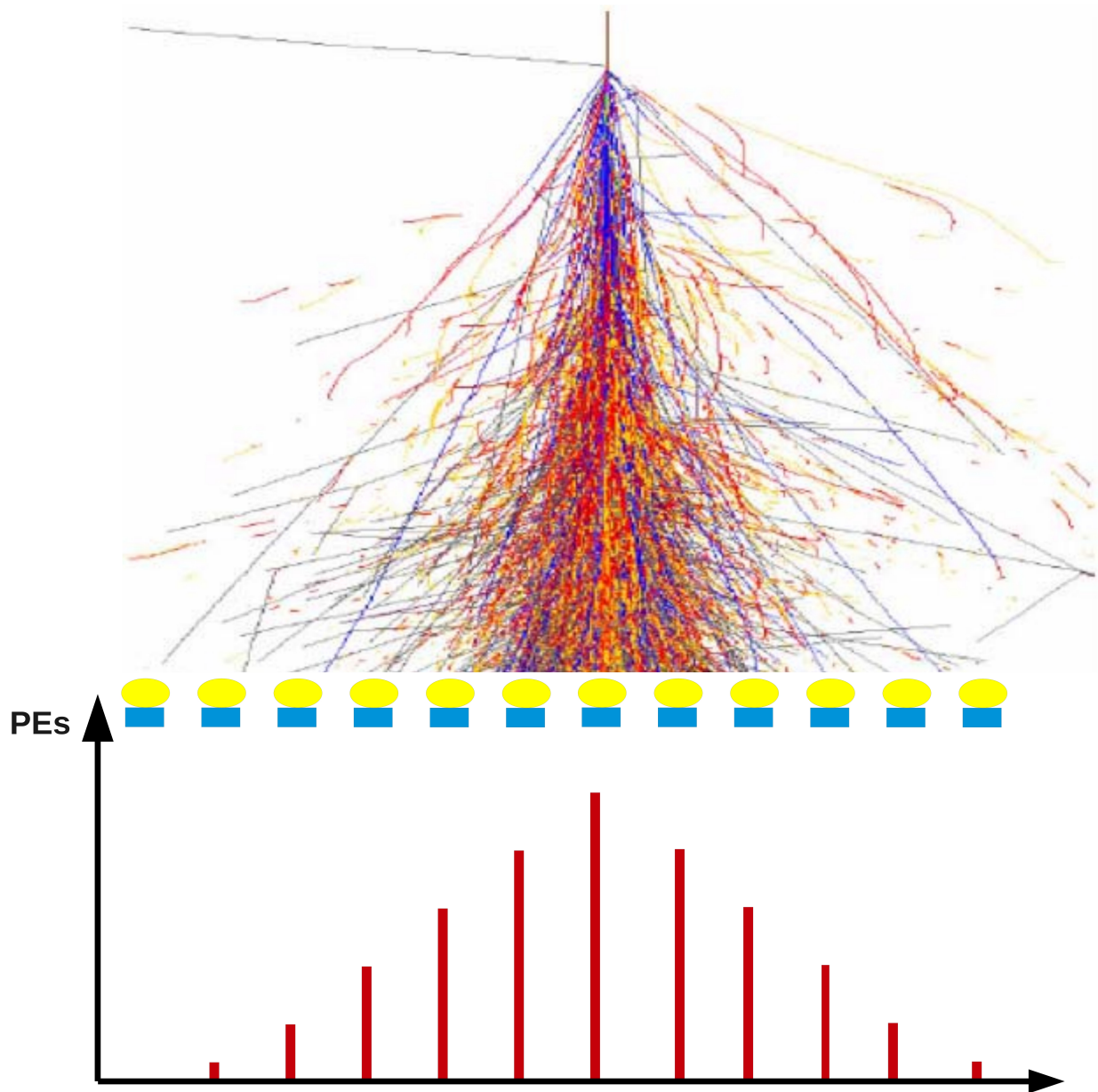


Figure 3.8: A conceptual diagram of the shower core location reconstruction. As an EAS lands on the Milagro detector, PMTs at the core of the shower detect larger numbers of photo electrons (PEs) compared to the PMTs at the edges of the shower. The histogram at the bottom shows the conceptual amplitude distribution of PEs.

be written as follows.

$$\theta = \arcsin\left(\frac{c\delta t}{L}\right) \quad (3.5)$$

Hence,  $\theta$  can be calculated using  $\delta t$  and  $L$  as measurable parameters. In order to get a good fit, the angle fitter algorithm uses all the PMT hits in a shower plane to reconstruct the shower angle.

The angle fitter algorithm used in Milagro was an iterative algorithm that fit a shower plane in 3D space. The iteration starts by assigning a weight to each PMT and a cut based on the number of PEs in each PMT. The PMTs that detected fewer PEs get a lower weight. This weighted timing distribution is then fit to a shower plane using a 3D version of the 2D algorithm explained in the above paragraph. At the end of an iteration, PMTs with poor residuals are removed from the fit and the process is repeated with a looser PE cut. This process is iterated five times and counts the number of PMTs used in the final fit (nFit).

### 3.5 Monte Carlo Simulations

Milagro Monte Carlo (MC) simulations were done in two stages. In the first stage EASs were generated and propagated through the atmosphere using CORSIKA (COsmic-Ray SIMulations for KAskade) v6.5021. CORSIKA simulations start with the first interaction of the primary particle in the atmosphere. Then the shower propagates through the atmosphere with the interactions of the secondary particles until the shower front reaches the ground. In the Milagro MC simulations, both gamma-ray and hadron initiated showers were thrown with a power law spectrum of  $E^{-2.0}$ . Later in the MC simulation chain showers were properly re-weighted to match the hadronic cosmic ray spectrum and to match the ratio of hadron generated showers to gamma-ray generated showers.

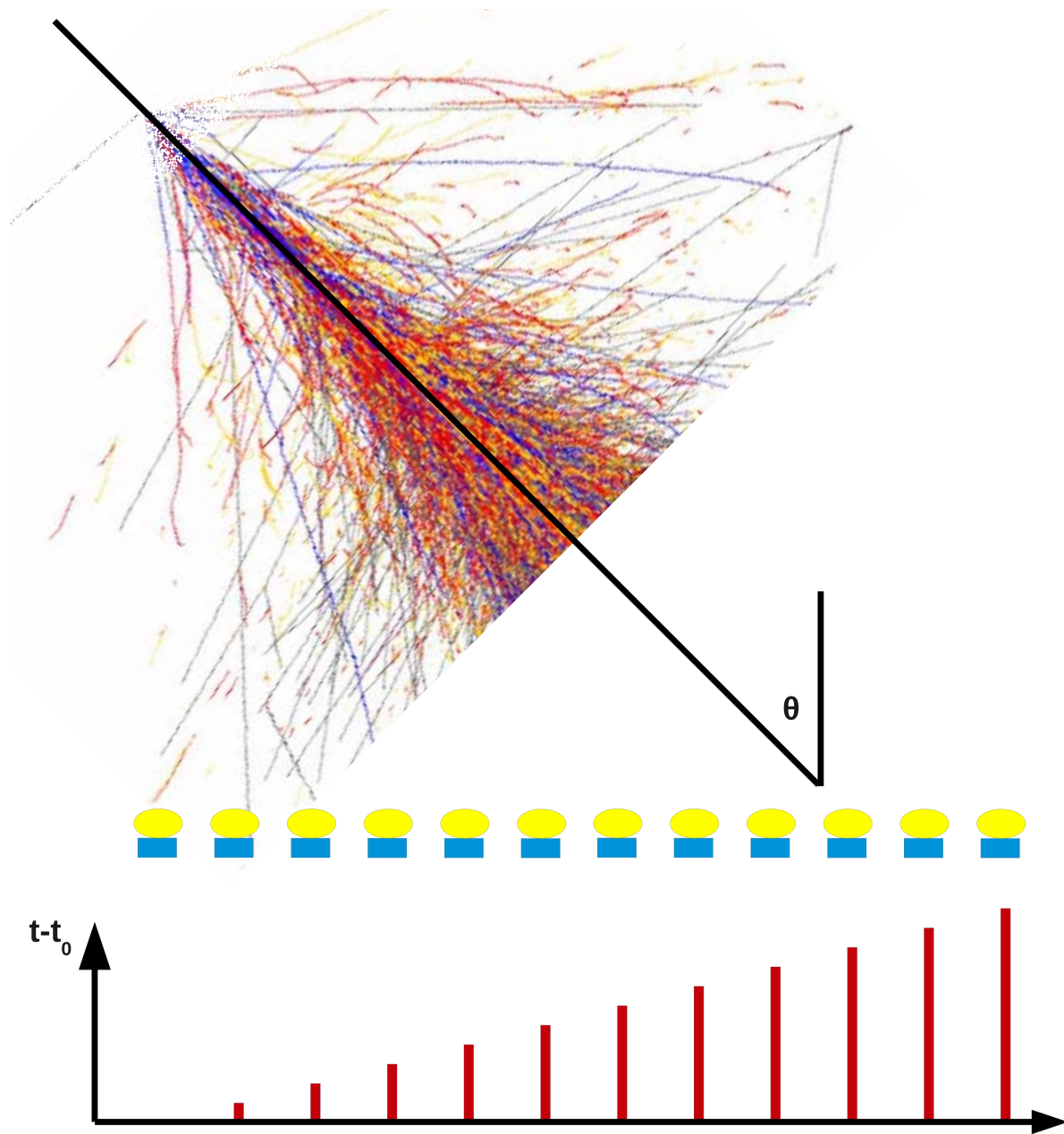


Figure 3.9: A conceptual diagram of the shower incidence angle reconstruction in a 2 dimensional space. As an EAS lands on the Milagro detector with an angle  $\theta$ , one end of the shower lands on the detector earlier than the other end. The histogram at the bottom shows the conceptual distribution of the arrival times of a shower on each PMT relative to the shower arrival time at the first PMT.

The second stage of the MC simulation chain is to simulate the response of the Milagro detector to EASs, which was done using GEANT4(GEometry ANd Tracking). GEANT4 takes the CORSIKA output at ground level and propagates the shower particles through a model of the Milagro detector. The output of GEANT4 includes the number of PEs and the arrival time of each PMT hit, which can be turned into a TOT signal as described in Section 3.2. Then this MC simulated data sample is sent through the reconstruction software to reconstruct the shower properties. The reconstructed shower properties that were used in the work presented in this thesis are shown in Table 3.5.

Data field name	Content
nCalAS	Number of PMT hits in the Air Shower Layer.
nLiveASTubes	Number of live PMTs in the Air Shower Layer.
nCalOR	Number of PMT hits in the Outrigger array.
nLiveORTubes	Number of live PMTs in the Outrigger array.
nCalMU	Number of PMT hits in the Muon Layer.
Theta	Zenith angle of the shower.
XCore	X coordinate of the shower core.
YCore	Y coordinate of the shower core.
nFit	Number of PMTs used in the shower plane fit,
.	Refer to Section 3.4.2 for more details.
A5	This is the gamma-hadron separation parameter, Refer to Section 4.1 for more details.

Table 3.1: The reconstructed shower properties that were used in the work presented in this thesis. The term ‘Cal’ stands for calibrated.



# Chapter 4

## Milagro Data Analysis Framework

The Milagro reconstructed data set is a collection of gamma-ray and hadron initiated EASs. In order to search for gamma-rays coming from celestial gamma-ray sources, this data set needs to be processed into a useful form. This chapter briefly explains the separation of gamma-ray and hadron initiated showers, estimation of the background, calculation of the significance and finally how to calculate the TeV flux of a sky location.

### 4.1 Gamma/Hadron Separation Parameter

The Milagro reconstructed data set consists of both gamma-ray initiated EASs, which are signal events, and hadron initiated EASs, which are background events. Distinguishing the signal from the background with a 100% efficiency is an impossible task. Therefore, the data has been statistically discriminated using the parameter  $A5$ , which was defined as:

$$A5 = 400 \cdot \frac{\left( \frac{N_{AS}}{N_{AS}^{live}} + \frac{N_{OR}}{N_{OR}^{live}} \right) \cdot \zeta(t) \cdot F_{fit}}{MaxPE_{MU}}, \quad (4.1)$$

where  $N_{AS}/N_{AS}^{live}$  is the fraction of live Air Shower layer PMTs that detected Cerenkov light in the event,  $N_{OR}/N_{OR}^{live}$  is the fraction of live Outrigger PMTs that detected Cerenkov light in the event,  $F_{fit}$  is the fraction of live PMTs used in the shower fitting algorithm explained in Section 3.4.2,  $\zeta(t)$  is a run-dependent correction which corrects for the systematic variations of each run such as changes in calibration, the denominator  $MaxPE_{MU}$  is the maximum number of photo-electrons recorded by a PMT in the muon layer and the constant 400 is an arbitrary scaling factor that gives  $A5$  typical values between 0 and 10.

The numerator of  $A5$  is a function of the shower size, which becomes larger for showers with larger size. The denominator of  $A5$  is expected to be larger for hadron initiated EASs relative to the gamma-ray initiated EASs, because of the high muon content in hadron initiated EASs. Therefore,  $A5$  is expected to typically be larger for gamma-ray initiated EASs, and rejecting events with lower  $A5$  values decreases the background contamination in the Milagro data set. Typical data analyses use a cut of  $A5 > 1$  for background rejection. Even after this cut was applied, the Milagro data set was  $\sim 99\%$  background events.

## 4.2 Background Estimation

The search for gamma-ray events in the Milagro data set is obscured by the  $\sim 99\%$  background contamination. Therefore, the correct estimation of the background is a very important step. Underestimation of the background could cause background fluctuations to appear as real signals, and overestimation could cause real signals to be hidden in the data. The work presented in this thesis used the direct integration method [Abdo et al.(2012)] to estimate the background.

For a short time interval (typically 2 hours) the local angular distribution of the back-

ground events can be written as a function  $F(h, \delta)$  depending on the local hour angle ( $h$ ) and declination ( $\delta$ ). This function can be turned into an efficiency distribution for a given declination band by normalizing the function into a unit area,  $\varepsilon(h, \delta) = F(h, \delta) / \int F(h, \delta) dh$ , which gives the efficiency of a hadronic initiated EAS that comes from the local coordinates of  $(h, \delta)$ . The convolution of the efficiency distribution with the all-sky background rate  $R(\tau)$  gives the expected background coming from the local coordinates of  $(h, \delta)$ . Therefore, the background coming from a sky location with coordinates  $(\alpha, \delta)$  can be written as:

$$B(\alpha, \delta) = \int \int \varepsilon(h, \delta) \cdot R(t) \cdot \Gamma(h, R.A., t) dt d\Omega, \quad (4.2)$$

where  $\Gamma(h, R.A., t)$  is 1 if the hour angle, right ascension, and sidereal time are such that the event falls within the right ascension, declination bin of interest, and zero otherwise. In Milagro data analysis, this algorithm was applied to the full Milagro data set with a two hour integration time, because  $\varepsilon$  is a constant for short time intervals but we also have to choose a large enough time interval to get enough statistics. An example of this analysis is shown in Figure 4.1 using a four hour long Milagro data set. After computing  $B(\alpha, \delta)$ , the excess distribution can be obtained by subtracting  $B(\alpha, \delta)$  from signal  $S(\alpha, \delta)$ . This final step is shown in the bottom plot of the Figure 4.1. The example shown in Figure 4.1 extracted the excess distribution of a narrow-declination band as a function of right ascension using a four hour long data sample, with integration time also equal to four hours. The result of this process is an excess map of the celestial sphere in the equatorial coordinate system. Real Milagro maps are two dimensional maps of right ascension and declination. The excess distribution for each declination band was extracted using this algorithm.

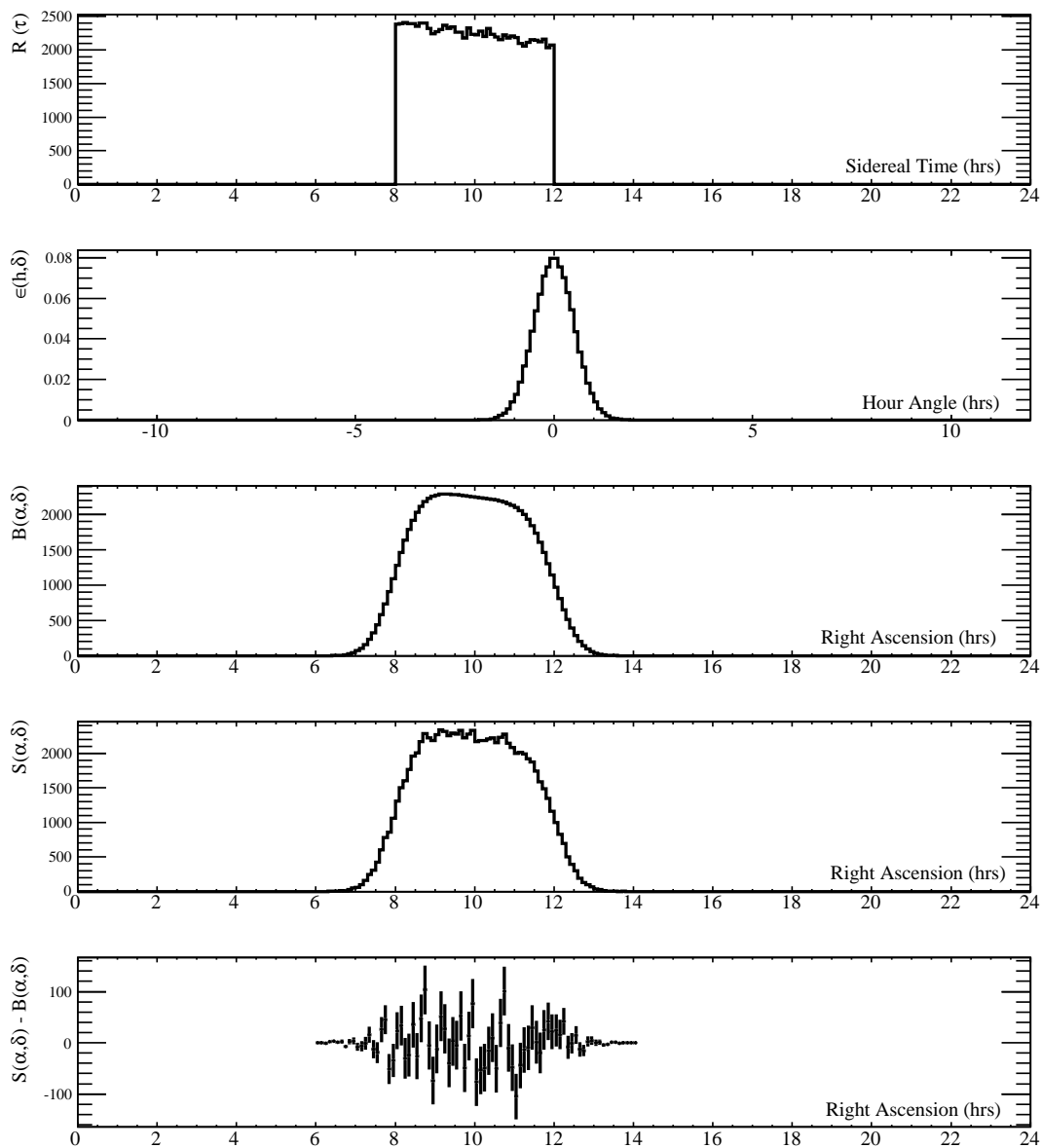


Figure 4.1:  $R(\tau)$  shown in the top histogram is the all sky background event rate.  $\varepsilon(h, \delta)$  shown in the second histogram from the top is the unit-normalized local-coordinate distribution of background event rate.  $B(\alpha, \delta)$  shown in the third histogram from the top is the convolution of the  $R(\tau)$  and  $\varepsilon(h, \delta)$ .  $B(\alpha, \delta)$  is the background estimation of the two hour data set as a function of right ascension  $\alpha$  and declination  $\delta$ . The fourth histogram from the top is the raw signal collected within a 4 hour period,  $S(\alpha, \delta)$ . The histogram at the bottom is the background subtracted signal,  $S(\alpha, \delta) - B(\alpha, \delta)$ .

### 4.3 Significance Maps

The next step after obtaining the excess map is to calculate the statistical significance of the excess. The significance calculation has been done using an extended version of the statistical method explained in Li & Ma(1983) with weighted events. The weights are assigned to optimize the statistical significance of a gamma-ray source in the sky. The Milagro analysis framework applied an event weight to each event based on two factors: the  $A5$  value and the expected signal-to-background ratio for an assumed spectrum as a function of the parameter call FRASOR ( $F$ ):

$$F = \frac{N_{AS}}{N_{AS}^{live}} + \frac{N_{OR}}{N_{OR}^{live}}. \quad (4.3)$$

FRASOR is an energy dependent parameter, therefore the expected number of events in each  $F$  bin<sup>1</sup> depends on the energy spectrum. The expected number of gamma-ray events for a given spectrum can be estimated using the Monte Carlo simulation. In this algorithm, an event that falls in an  $F$  bin with a higher gamma-ray event expectancy gets a higher weight compared to an event that falls in an  $F$  bin with a lower gamma-ray event expectancy. Similarly events with a larger  $A5$  value get a higher weight compared to events with a smaller  $A5$ . Therefore, an event with a larger  $A5$  that falls in an  $F$  bin with a higher gamma-ray event expectancy gets the highest event weight.

In addition to this weight, events are given another weight to account for the angular resolution of Milagro. For a given event, the incident angle can only be reconstructed with a finite angular resolution. Therefore, each recorded event is spread around the reconstructed angle assuming the angular resolution function is a 2-D Gaussian distribution. The width of the Gaussian distribution depends on the  $F$  bin, which ranges from  $1.2^\circ$  for small  $F$  bins

---

<sup>1</sup>Typically  $F$  is binned into 10 equal size bins.

to  $0.35^\circ$  for large  $F$  bins.

Since the weights depend on the assumed spectrum, the sky map obtained with this algorithm has a bias towards the assumed spectrum. Therefore, the Milagro analysis framework produced multiple Milagro sky maps with different spectral assumptions. The analysis presented in this thesis used two Milagro sky maps: a sky map made with a pure power law spectrum of  $E^{-2.5}$  was used to search for galactic sources, and a sky map made with a power law with an exponential cutoff,  $E^{-2.0}e^{-E/5TeV}$ , was used to search for extragalactic gamma-ray sources.

## 4.4 Flux calculation

The differential photon flux for a given source is defined as the number of photons received on the earth from the source per unit energy per unit area per unit time. For a power law (of index  $\alpha$ ) spectrum without a cutoff the differential photon flux can be written as:

$$\frac{dN}{dE} = I_o \left( \frac{E}{1 TeV} \right)^{-\alpha} \text{Photons TeV}^{-1}\text{cm}^{-2}\text{s}^{-1}, \quad (4.4)$$

where  $I_o$  is the flux amplitude (also known as the flux normalization) and  $\alpha$  is the power law index. For a power law spectrum with an exponential cutoff this can be written as:

$$\frac{dN}{dE} = I_o \left( \frac{E}{1 TeV} \right)^{-\alpha} e^{-\frac{E}{E_c}} \text{Photons TeV}^{-1}\text{cm}^{-2}\text{s}^{-1}, \quad (4.5)$$

where  $E_c$  is the cutoff energy. A plot of differential photon flux versus energy (sometimes frequency or wavelength) is called the Spectral Energy Distribution (SED).

The Milagro detector does not observe the photons with a constant efficiency across a

broad energy band. Therefore, the number of electrons measured by Milagro per second is the convolution between the Milagro effective area,  $A_{eff}(E, \theta)$ , and the true SED:

$$N_{observed} = \int \int A_{eff}(E, \theta) \frac{dN}{dE} d\theta dE \quad (4.6)$$

The integral of Equation 4.6 over energy and the Milagro detector's lifetime gives the expected excess that can be expected from the Milagro detector for a given SED:

$$N_E = \int \int A_{eff}(E, \theta(t)) \frac{dN}{dE} dE dt, \quad (4.7)$$

where  $N_E$  is the expected excess for a given energy spectrum.

In the Milagro data analysis framework, the differential photon flux of an observed source is derived from the ratio of the observed excess  $N_O$  to the expected excess  $N_E$ . The  $N_O$  is obtained from a sky map made with an assumed SED, and the  $N_E$  is obtained from Monte Carlo simulations with the same spectral assumption. These two parameters can be combined to derive the flux amplitude of the observed source:

$$I_o = \frac{N_O}{N_E} \times I_o \text{ Simulated}, \quad (4.8)$$

where  $I_o \text{ Simulated}$  is the flux amplitude used in Monte Carlo simulations to obtain  $N_E$ . Once  $I_o$  is derived, the differential flux at any energy can be derived using equation 4.4 or 4.5. Since this algorithm assumed an SED to obtain  $N_O$  and  $N_E$ , the calculated flux has a bias towards the assumed spectrum. This bias for three simulated sources, at a declination of 22, is shown in Figure 4.2. In this figure, I derived the flux in the range of 1 to 100 TeV of three simulated sources with  $\alpha = -2.2, -2.6$  and  $-3.0$ . As it can be seen in this figure,

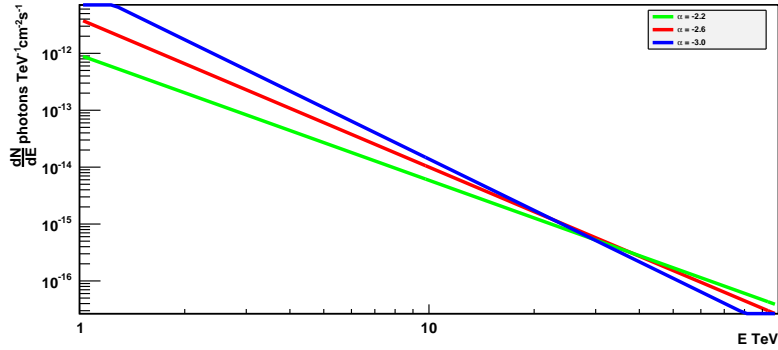


Figure 4.2: Simulated  $\frac{dN}{dE}$  as a function of energy for a pure power law spectrum is shown,  $\frac{dN}{dE} = I_o(E/\text{TeV})^{-\alpha}$ .  $I_o$ 's are selected to give the same excess for three sources with three different spectra, green  $\alpha = 2.2$ , red  $\alpha = 2.6$  and blue  $\alpha = 3.0$ . Flux for all three sources are calculated using spectral optimization of  $\alpha = 2.6$ . The region where the lines intersect indicates the energy range least dependent on the assumed spectrum.

the dependency of the calculated flux on the true spectrum is minimal between 20 and 30 TeV. The energy region with the minimum energy dependence is a function of the source declination, and varies between  $\sim 20$  TeV and  $\sim 50$  TeV for galactic sources. Therefore, the Milagro collaboration chose to publish the flux at 35 TeV for galactic sources and 7 TeV for extragalactic sources.

The work presented in this thesis also used the integral energy flux over an energy range:

$$F = \frac{N_O}{N_E} \times I_o \text{ Simulated} \times \int_{E_1}^{E_2} E \cdot E^\alpha dE \text{ TeV}. \quad (4.9)$$

which can be determined numerically once the flux amplitude is derived.

## 4.5 Energy Reconstruction

The algorithm presented in the previous section can be used to derive the differential photon flux at a given energy. However, that algorithm cannot be used to derive the SED in a given



energy range. Milagro used a parameter called FRASOR (defined in equation 4.3) as an energy estimator to obtain the SED of the Crab pulsar wind nebula using the forward folding technique [Abdo et al. (2012)]. The forward folding technique is only capable of identifying the best SED, that describes the data, among a set of assumed SEDs. Therefore, the forward folding technique depends on how well the true SED can be guessed. In Abdo et al. (2012) a power law with an exponential cutoff was assumed,

$$\frac{dN}{dE} = \left( \frac{I_o}{1 \text{ TeV}} \right) E^{-\alpha} e^{-\frac{E}{E_c}}. \quad (4.10)$$

Then a sample of expected FRASOR distributions was produced using the Milagro Monte Carlo simulations, by changing the  $\alpha$ , ( $I_o$ ) and  $E_c$ . In Milagro technical jargon, the table that summarizes the results from these simulations is called the Gamma-table. More details about the Gamma-table are discussed in Appendix . In the next step each expected FRASOR distribution was compared with the observed FRASOR distribution using the  $\chi^2$  test. The significance contours of the  $\chi^2$  test in  $\alpha - E_c$  space and  $\alpha - I_o$  space is shown in Figure 4.3. These two significance contour plots led the authors of Abdo et al. (2012) to conclude that the SED of the Crab Pulsar Wind Nebula can be best described by:

$$\frac{dN}{dE} = \left( \frac{2.5^{+0.7}_{-0.4} \times 10^{-12}}{1 \text{ TeV}} \right) E^{2.5 \pm 0.4} \exp \left( -\frac{E}{32^{+39}_{-18} \text{ TeV}} \right) \text{cm}^{-2} \text{s}^{-1} \text{TeV}^{-1} \quad (4.11)$$

The accuracy of this spectrum was limited for three reasons: poor energy resolution, poor linear correlation between FRASOR and  $\log_{10}(\text{true energy})$ , and the limitations of the forward folding technique. FRASOR is derived from two parameters: the number of Air Shower layer PMT hits and the number of Outrigger tank hits. These two parameters are

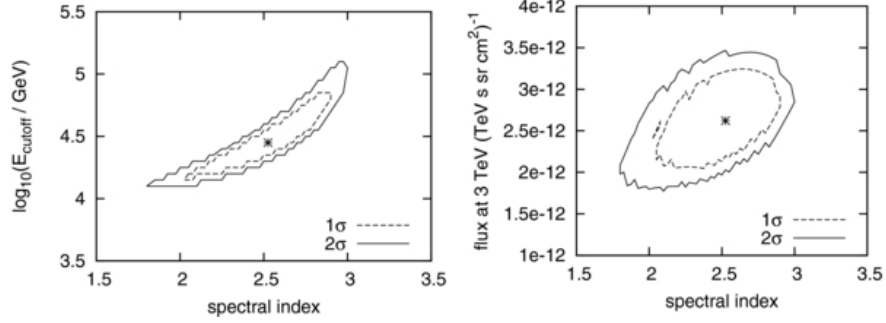


Figure 4.3: Two significance contour plots in the  $\alpha - E_c$  and  $\alpha - I_o$  space obtained from forward folding are shown [Abdo et al. (2012)]. The spectral assumption is a power law with an exponential cutoff, as shown in equation 4.10. The figure on the left shows the  $1\sigma$  and  $2\sigma$  contours in the  $\alpha - E_c$  space. The figure on the right shows the  $1\sigma$  and  $2\sigma$  contours in the  $\alpha - I_o$  space.

highly sensitive to the size of the EAS. However, the size of the EAS depends not only on the energy of the initial gamma-ray photon but also on its zenith angle and shower core location. FRASOR is not sensitive to the zenith angle and the shower core location, these are limiting Milagro's energy resolution. I developed an improved energy estimator by combining the zenith angle, shower core location and some other variables available in Milagro reconstructed data. The performance of my energy estimator is discussed in Appendix .

The main limitation of the forward folding technique is that it picks the SED that best describes the observed data from a set of known SEDs, instead of deriving the true SED from the data. Therefore, picking the correct sample of SEDs is crucial, because it is not possible to generate the expected FRASOR distribution using all possible SEDs. The expected FRASOR distributions are generated from a set of discrete parameters for a limited number of SED functional forms. An alternative method to overcome this issue is unfolding. In my thesis work I applied the unfolding technique to get the true SED shape of a source observed by Milagro. However, it turned out that the energy resolution of the Milagro detector, even with an improved energy estimator, was insufficient to apply unfolding algorithms to the

Milagro data set.

# Chapter 5

## The Fermi Large Area Telescope (Fermi-LAT) GeV Catalogs

The Fermi Gamma-ray Space Telescope (formerly known as the Gamma-ray Large Area Space Telescope, GLAST) was launched by NASA on June 11, 2008 on a Delta II heavy launch vehicle. The Fermi space telescope consists of two on-board instruments: the Gamma-ray Burst Monitor (GBM) and the Large Area Telescope (LAT). Fermi-GBM monitors Gamma-ray bursts in the energy range of 8 keV to 40 MeV, and the Fermi-LAT surveys the sky in the energy range of  $\sim 20$  MeV to  $\sim 300$  GeV. The work presented in this thesis used two catalogs produced by Fermi-LAT: the Fermi Large Area Telescope Second Source Catalog, also known as 2FGL [Nolan et al.(2012)] and the Second Fermi Large Area Telescope Catalog of Gamma-ray Pulsars, also known as 2PC [Abdo et al.(2013)]. This chapter gives a brief introduction to Fermi-LAT, 2FGL and 2PC.

## 5.1 Fermi Large Area Telescope (Fermi-LAT)

The Fermi-LAT consists of 16 precision converter-trackers and 16 calorimeters arranged in a  $4 \times 4$  array. A schematic diagram of Fermi-LAT is shown in Figure 5.1. An internal view of a precision converter-tracker and an incoming gamma-ray is shown at the center of this figure. Each precision converter-tracker consists of alternating layers of tungsten conversion foil and silicon strip detectors, which have two layers of strips oriented perpendicular to each other. At the bottom of each precision converter-tracker is a cesium iodide (CsI) calorimeter.

When a gamma-ray enters a precision converter-tracker it interacts with one of the conversion foils and produces an electron-positron pair. The resulting electron-positron pair is traced by the Silicon Strip Detectors in successive layers. The incidence angle of the initial gamma-ray can be constructed using the traces of the electron and positron. The cascading of a gamma-ray is illustrated in Figure 5.1 using a red-dotted line and two blue-dotted lines.

After passing through the precision converter-tracker the electron-positron pair enters the calorimeter, which consists of 96 optically isolated CsI crystals of size  $2.7 \text{ cm} \times 2.0 \text{ cm} \times 32.6 \text{ cm}$ . These crystals are arranged horizontally in eight layers of 12 crystals each with each layer rotated  $90^\circ$  with respect to its adjacent layers. When the electron or positron passes through a crystal, it converts its the electron's or positron's energy into scintillation light, which is measured by two PIN diodes mounted on each end of the crystal. The sum of the light deposited in the PIN diodes provides a determination of the energy deposited on the crystal. The difference in light levels deposited in the two PIN diodes provides a determination of the position of the energy deposition along the crystal. In addition to these two measurements, the physical location of the crystal in the calorimeter provides two more coordinates of the location of the energy deposit. These measurements can be combined

to measure the energy of the electron-positron pair produced by a gamma-ray, which can be used to reconstruct the energy of the primary photon, and to reconstruct the shower development profile.

The dominant background for the Fermi-LAT is high-energy charged cosmic-ray particles. In order to identify these particles Fermi-LAT was covered with an Anti-Coincident Detector (ACD). The ACD is made from plastic scintillation tiles, and the light from each tile is collected by wavelength shifting fibers that are coupled to two photo multiplier tubes. When a charged cosmic-ray passes through the tiles it produces scintillation light, while a gamma-ray can pass through the tiles without interaction. Therefore, charged cosmic-ray particles produce coincident events both at the ACD and in the precision converter-trackers or in the calorimeters, while gamma-rays produce a signal only in the precision converter-trackers and in the calorimeter. This feature has been used to identify the charged cosmic-ray events.

## 5.2 Fermi-LAT Second Source Catalog (2FGL)

The Fermi-LAT Second source catalog, which is known as 2FGL, is a catalog of high-energy gamma-ray sources detected by Fermi-LAT in the first two years of its operation [Nolan et al.(2012)]. This catalog includes 1873 sources that were observed in the 100 MeV to 100 GeV energy range during the period from August 4, 2008 (15:43 UTC) to August 1, 2010 (01:17 UTC). During this period, Fermi mostly operated in sky-scanning survey mode, which evenly scans the full sky by rocking north and south of the zenith on alternate orbits. With this rocking motion the corresponding exposure at all sky locations are relatively uniform. However, the exposure is minimum at the celestial equator and it is maximum at the north celestial pole. The ratio of maximum exposure to minimum exposure depends on the

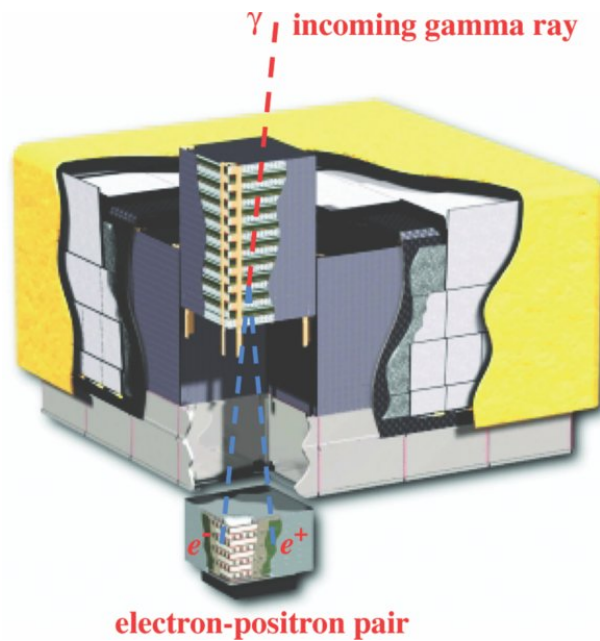


Figure 5.1: Schematic diagram of Fermi-LAT. A precision converter-tracker and calorimeter is shown at the center of the figure. Here the calorimeter is taken apart from the precision converter-tracker. The red dotted line indicates the track of a gamma-ray and the blue dotted lines indicate the tracks of the cascade electron and positron. The physical size of this detector is  $1.8 \text{ m} \times 1.8 \text{ m} \times 0.72 \text{ m}$ . It weighs 2789 kg and in normal operation mode consumes 650 W. This figure was obtained from the publication [Atwood et al.(2009)].

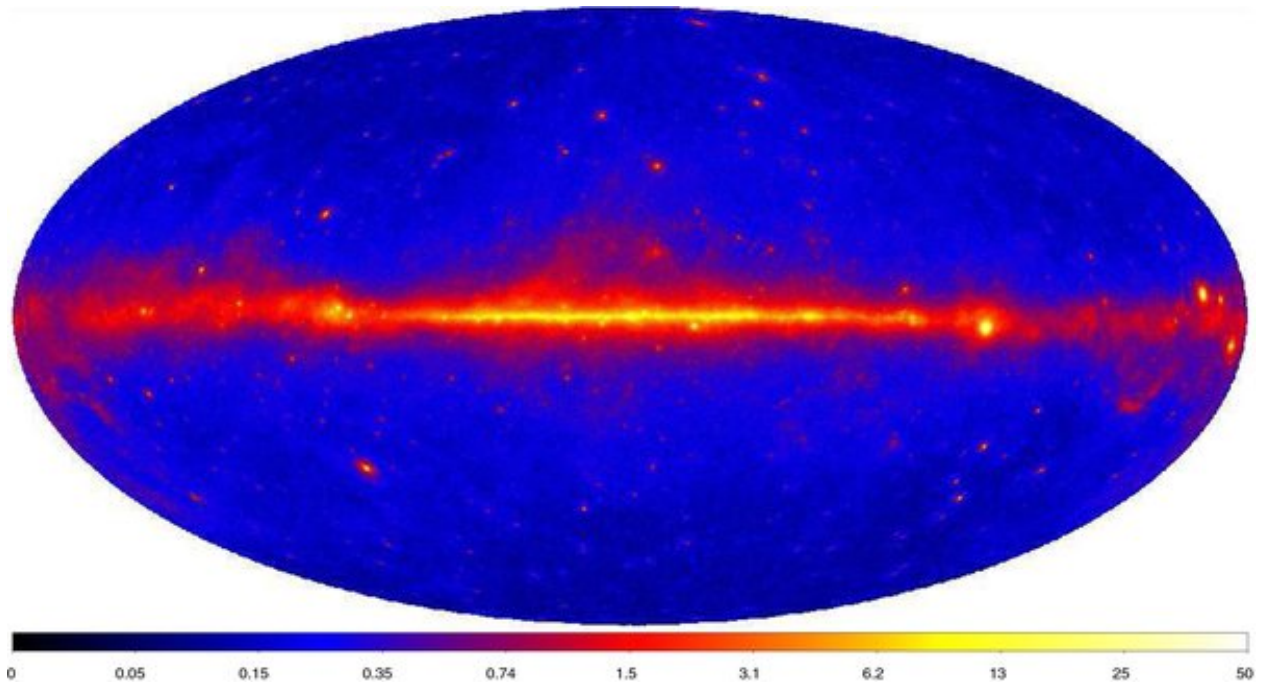


Figure 5.2: The Aitoff projection of the significance sky map derived from the data set used to make the Fermi Large Area Telescope Second Source catalog. This map includes the gamma-ray energy flux measured in the range between 100 MeV and 10 GeV. Refer to [Nolan et al.(2012)] for the original figure and a more detailed description of data. Color scale shows the gamma-ray significance of each sky location.

rocking angle, which was  $35^\circ$  at the beginning of the data collection and later changed to  $50^\circ$ . With a  $35^\circ$  rocking angle the ratio of maximum exposure to minimum exposure was 1.33 in contrast to 1.75 for rocking angle  $50^\circ$ . The sky map of the energy flux derived from this data set is shown in Figure 5.2.

Among the sources reported in this catalog,  $\sim 68\%$  are sources off the Galactic plane (galactic longitude  $> |10^\circ|$ ) that have no association with known galactic sources. From these extra galactic sources 709 are located within Milagro's sky coverage ( $7^\circ < \text{DEC} < 80^\circ$ ). This provided a targeted list of extragalactic candidates for Milagro to search for TeV gamma-ray emission associated with extragalactic GeV sources. The results from a Milagro targeted search on this source list is presented in Chapter 8.



## 5.3 The Second Fermi-LAT Catalog of Gamma-ray Pulsars (2PC)

The second Fermi-LAT Catalog of Gamma-ray Pulsars (2PC) is a catalog of 117 GeV-pulsars measured by Fermi-LAT in the energy range of 0.1 GeV - 100 GeV, using data collected from August 14, 2008 to August 14, 2011[Abdo et al.(2013)]. Similar to the data collection period for 2FGL, Fermi mostly operated in the sky-scanning mode during this period. They excluded the data when Fermi-LAT was not operating in the science operations mode, the rocking angle exceeded  $52^\circ$ , or the gamma-rays were detected with a zenith angle greater than  $100^\circ$ . This data set was searched for GeV pulsars using these different methods: a targeted search using known pulsars measured in radio or X-ray energies, a targeted search with a candidate list made from known GeV point sources (e.g. SNR), and a blind search. The first method searched for GeV pulsation in the LAT data using 2286 known pulsar ephemerides and identified 60 GeV pulsars. This is the most sensitive method for observing pulsars with low gamma-ray fluxes. However, this method can not identify radio and X-ray quiet pulsars. The other two methods were able to discover 57 new GeV pulsars.

From these 117 GeV pulsars, 32 were located within Milagro's sky coverage ( $7^\circ < \text{DEC} < 80^\circ$ ). I performed a Milagro targeted search on this list of 32 pulsars and the results are presented in Chapter 9. The analysis presented in Chapter 9 used the pulsar period ( $P$ ), the first derivative of the pulsar period ( $\dot{P}$ ), the spin-down luminosity ( $\dot{E}$ ), the phase averaged integrated energy flux in the 0.1 to 100 GeV energy band ( $G_{100}$ ) and the distance to the pulsars, all of which are readily available in the 2PC.

The 2PC obtained the  $P$  and  $\dot{P}$  of a pulsar from observed data, and  $\dot{E}$  was derived from

the  $P$  and  $\dot{P}$  using equation 5.1.

$$\dot{E} = 4\pi I_{\circ} \dot{P} / P^3, \quad (5.1)$$

where  $I_{\circ} = 10^{45} \text{g cm}^2$ . Full derivation of this equation is given in Section 2.2.2. The integrated energy flux in the 0.1 to 100 GeV energy band was derived by integrating the Spectral Energy Density (SED). The SEDs were obtained by forward folding a power law with an exponential cutoff,

$$\frac{dN}{dE} = I_{\circ} \left( \frac{E}{E_{\circ}} \right)^{-\alpha} \exp \left( -\frac{E}{E_{cut}} \right). \quad (5.2)$$

The pivot energy  $E_{\circ}$  was arbitrarily defined as 1 GeV for pulsars unassociated with 2FGL sources. For the pulsars associated with 2FGL the  $E_{\circ}$  listed in 2FGL was used. The  $I_{\circ}$ ,  $\alpha$  and  $E_{cut}$  are the input parameters, and the best fit values of these input parameters were obtained using a likelihood analysis method. Once the best SED was identified, the  $G_{100}$  was derived by integrating the SED,

$$G_{100} = \int_{100 \text{ MeV}}^{100 \text{ GeV}} E \frac{dN}{dE} dE \quad (5.3)$$

## 5.4 Source Naming Convention

Both the 2FGL catalog and the second pulsar catalog use the same naming convention, XXXX JHHMM.m+DDMM[c]. The first set of characters, XXXX denotes the name of the catalog. In the 2FGL catalog XXXX is 2FGL, and in the second pulsar catalog XXXX is PSR. In the 2FGL catalog ‘2’ refers to the second-year catalog and ‘FGL’ represents Fermi Gamma-ray LAT. HHMM.m is the right ascension written in hours and truncated to 0.1

decimal minutes. DDMM is the declination written in degrees and truncated to 1 degree. The suffix 'c' is optional, which indicates that the source is considered to be potentially confused with Galactic diffuse emission.

# Chapter 6

## The High Altitude Water Cherenkov Observatory (HAWC)

The High Altitude Water Cherenkov observatory (HAWC) is the successor to the Milagro observatory. HAWC is currently under construction near the Volcano Sierra Negra, Mexico at latitude  $18^{\circ}59'48''$  North, longitude  $97^{\circ}18'34''$  West and altitude 4100m. As a part of my thesis work I developed the firmware for HAWC's GPS Timing and Control (GTC) system. In this chapter I briefly present the design of the HAWC observatory and the working principles of the GTC system.

### 6.1 The HAWC Detector

The HAWC detector is designed on the same principles as Milagro. The primary difference between Milagro and HAWC is that instead of a large water pond HAWC consists of densely packed steel water tanks of 7.3 m in diameter and 4.5 m in height. Each of these tanks holds a light-tight bladder filled with about 200,000 liters of ultra purified water, and 4 PMTs

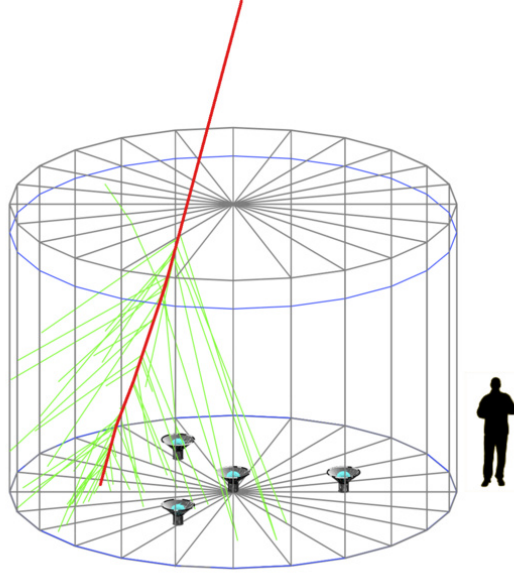


Figure 6.1: A drawing of a HAWC tank with 4 PMTs at the bottom.

are placed near the bottom of the bladder. A drawing of the tank and the 4 PMTs at the bottom is shown in Figure 6.1. The PMT at the center is a Hamamatsu 10'' high quantum efficiency, 7081HE PMT, and the other three PMTs are 8'' Hamamatsu R5912 PMTs reused from Milagro. HAWC also reused the front-end electronics boards from Milagro. CAEN VX 1190A TDCs are used to digitize the TOT signal outputs of the front-end electronics boards. Each of these TDCs can digitize 128 input signals. Currently HAWC has 111 tanks operational, which uses 4 TDCs. When HAWC is completed in 2014, it will have 300 tanks and use 9 full TDCs and 48 channels from a 10th TDC to digitize the PMT signals. Other than the 10 TDCs used to record PMT signals, an 11<sup>th</sup> TDC will be used to record 32 signals coming from the GPS Timing System. These signals are similar to the TOT signals, but they are encoded with the current GPS time, which is the time-stamp of an event. Further details of the time-stamps are discussed in section 6.2.2.

CAEN Vx 1190A TDCs are designed to record TOT measurements within a given time window around a trigger signal, and are equipped with an output buffer to store the recorded

data until they are read out. As each TDC buffer fills with data, a GE XVB602 Intel Core i7 based VME Single Board Computer (SBC) reads each individual TDC in parallel and delivers the data to the online reconstruction farm. However, each SBC cannot perform the readout process at the same rate. Therefore, the online reconstruction farm receives different fragments of a single event at different times. The HAWC online reconstruction software identifies the event fragments belonging to a given trigger using the event identification number (Event ID), which is a 12 bit number that is stamped on each event by the TDCs. After identifying the fragments of a single event, the online reconstruction process combines the fragments into a single event and decodes the time-stamp into a computer readable data type. This defragmentation is possible only if all the TDCs are working synchronously and maintain a unique Event ID for a given trigger. This was achieved by the control part of the GTC system that controlled the TDCs through its control bus.

The controlling of the TDCs is done using three signals of the TDC control bus: TRG, CLR and CRST. The TRG is the trigger signal to the TDCs. In HAWC, the trigger signal is a periodic signal that is provided by the GTC system. In a typical data run the periodic trigger frequency is 40 kHz (period = 25  $\mu$ s) and the TDCs record the data in a 25.2  $\mu$ s window around each trigger. The data saved in a given time window is called an event. The CLR is the clear command, which clears the data from the output buffer, resets the event counter, and performs a TDC global reset. The CRST is the reset command, which performs the same actions as the CLR, in addition to resetting some of the other internal counters of the TDC. Further details of the interface between the control bus and the GTC system are discussed in section 6.2.3.

## 6.2 GPS Timing and Control System (GTC System)

Because of its central role, the GTC system is considered the central nervous system of HAWC. As its name suggests the GTC system combines two sub-systems: the GPS Timing system and the Control system. The primary tasks of the GPS Timing system is to provide a time-stamp for each recorded event, which is the absolute time of the trigger, and to derive a low jitter 40 MHz signal to use as the global clock signal for HAWC. The primary task of the Control system is to provide the clock and the control signals to the TDCs and to provide trigger and detector status information to the scaler system.

### 6.2.1 GPS Timing System Hardware

The GPS Timing system consists of a GPS receiver and a customized piece of electronics called the Clock type H\_Clock card. A functional block diagram of the GPS Timing system is shown in Figure 6.3. The NAVSYNC CW46 GPS receiver is a commercial GPS receiver that carries three signals to the Clock type H\_Clock Card. H\_Clock cards are general-purpose custom cards, and Clock type refers to a version of the H\_Clock cards. A photograph of a fully assembled H\_Clock card is shown in Figure 6.2.

An H\_Clock card is a 2 unit wide 6U VME-64X module that is equipped with a Phase Lock Loop (PLL), 10 LVDS type General Purpose Input Output (GPIO) connectors, a 16 pin connector to the GPS receiver, a A24D16 VME interface and a Virtex II FPGA on a mezzanine board. In Figure 6.2 the ten GPIO connectors are on the left. Each of these ports has 17 signal pairs; 16 of them are LVDS GPIO signals to/from the FPGA, and the 17<sup>th</sup> pair is a 40 MHz clock signal which is also a LVDS type signal. The direction of the GPIO ports are reversible by replacing the IO driver chips. Clock type H\_Clock cards are created

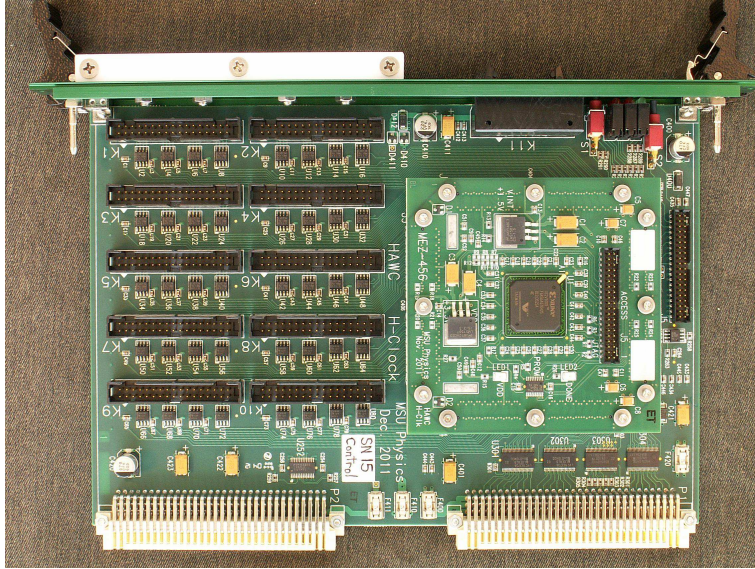


Figure 6.2: A photograph of a fully assembled H-Clock card is shown. The Clock version of the H-Clock card with 2 general purpose input ports and 8 general purpose output ports are used in the Clock System. The Control version of the H-Clock card used in the Control System has 4 general purpose input ports and 6 general purpose output ports.

by configuring H-Clock cards with two input ports and eight output ports. The FPGA is mounted in a mezzanine card (on the right in the picture). Since the performance and the resources of the Virtex II family FPGAs are adequate for the requirements of HAWC, a Virtex II xc2v1000-4fg456 FPGA is used. A stock of this FPGAs was also available at MSU. However, if a future upgrade needs to change the FPGA, it can be done by making a new mezzanine card.

The GPS receiver is used to obtain the GPS time and a low jitter 10 MHz sine wave signal. The internal PLL of the Clock type H-Clock Card uses this 10 MHz sine wave signal to derive a low jitter 40 MHz digital clock signal and makes several exact copies that are delivered to the Control type H-Clock Card, to the FPGA and to the 17<sup>th</sup> signal pair of all the GPIO connectors. This 40 MHz signal is used as the global clock signal for HAWC. The GPS receiver also transmits a one pulse per second (1PPS) pulse stream and a set of data strings via the RS232 protocol. The rising edges of these 1PPS pulses mark the top of each



second. The firmware running inside the FPGA uses this 1PPS signal and the data strings to replicate the current GPS time.

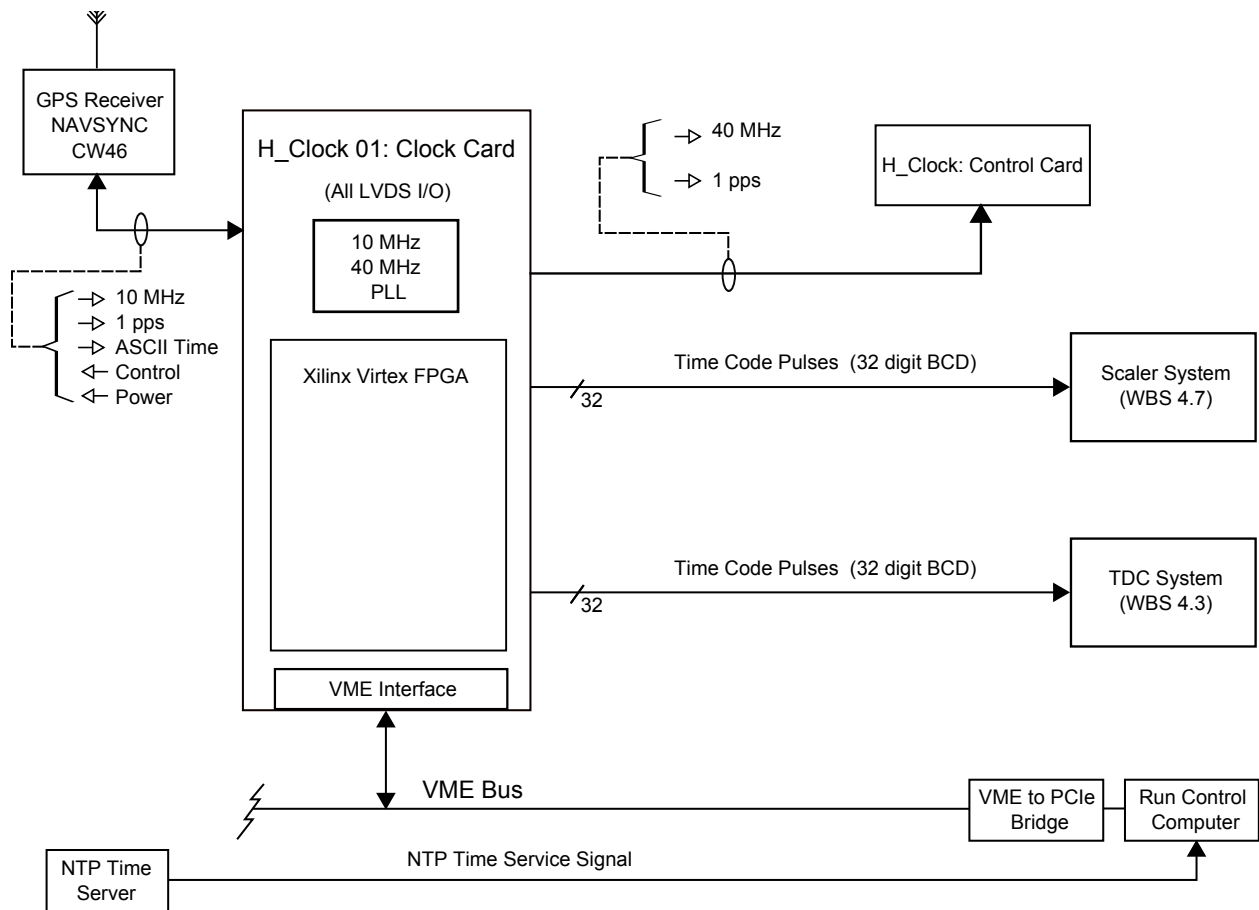


Figure 6.3: A block diagram of the Clock System is shown. The NAVSYNC CW46 GPS receiver and the Clock Card are the two main components of the Clock system. The GPS receiver is used to obtain the GPS time and a low jitter 10 MHz signal. The Clock Card produces a 40 MHz global clock signal and two time-stamps for the scaler system and for the TDC system. The communication between the Clock Card and the control computer is accomplished through a A24D16 VME interface.

## 6.2.2 GPS Timing System Firmware

The logic operations of the GPS Timing system are done by the firmware running in the FPGA. Part of my PhD thesis work was to develop, test and implement this firmware. A simplified functional block diagram of this firmware is shown in Figure 6.4. This is a

sequential logic design with several state machines implemented using VHDL. In this section I briefly discuss the functionality of this firmware.

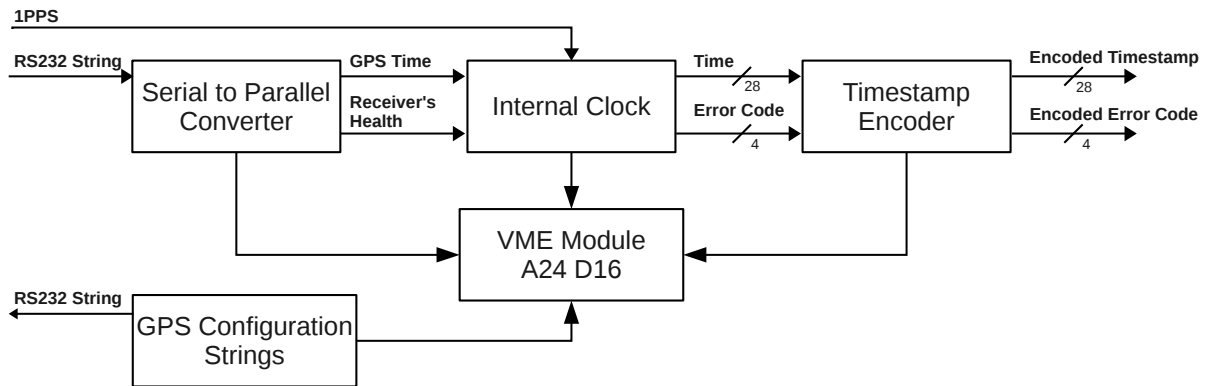


Figure 6.4: A simplified functional block diagram of the Clock firmware is shown. This firmware maintains an internal clock synchronized with the GPS time and produces TDC readable time-stamps. The communication between this module and the control computer was done by a A24D16 VME interface.

The first module of the firmware, the Serial to Parallel Converter, reads the serial data strings coming from the GPS receiver and extracts the current GPS time and the GPS receiver’s health information from the GPS signals. The GPS receiver installed at the HAWC site is configured to send three data strings followed by a 1PPS pulse. These three strings (POLYT, GPGSA and POLYP) are standard NMEA 0183 strings, which carry the current GPS time, GPS receiver operating mode, satellites used to derive the time, and dilution of precision (DOP) values. The Serial to Parallel Converter module extracts the current GPS time from the POLYT string, GPS Fix status from the GPGSA string<sup>1</sup>, and dilution of precision measurements from the POLYP string. Then the GPS time and health information goes to the Internal Clock module, which is a continuously running 8 digit binary-coded

<sup>1</sup>GPS Fix is an integer between 1 and 3. If the GPS receiver is not getting enough GPS signals and it is unable to fix, GPS Fix is 1. If GPS receiver is being able to become to a 2D or 3D fix this GPS Fix becomes 2 or 3 respectively. Refer to the CW25 GPS Receiver User Manual for more information.

decimal (BCD) clock that runs using the 40 MHz clock signal as the reference frequency.

The least significant digit of the internal clock is microseconds and the most significant digit is tens of seconds. Apart from the signals coming from the Serial to Parallel Converter module, the Internal Clock module also receives the 1PPS signal that comes from the GPS receiver, which is used to identify the top of each second. At the top of each second, the Internal Clock module compares its clock time with the GPS clock time, and overwrites the internal clock if the time does not match (and the GPS receiver is in good health). This allows the GPS Timing System to have an internal clock that runs synchronously with the GPS clock.

The second stage is the Timestamp Encoder module, where the time of the internal clock is encoded into a 32 bit TDC readable time-stamp and then transmitted to the TDCs every  $\Delta T \mu s$  interval ( $\Delta T \mu s$  can be configured to  $10 \mu s$  or  $20 \mu s$ ). The first 28 bits of the time-stamps are 7 BCD-digits that carry the time in the format: 10's of s, 1's of s, 100's of milliseconds, 10's of milliseconds, 1's of milliseconds, 100's of microseconds and 10's of microseconds. The last four digits of a time-stamp are the error code of the time-stamp, which is described in Table 6.1. The encoding of this time-stamp to a TDC readable format is done using a simple algorithm. Each bit is denoted by a pulse; a  $1 \mu s$  wide pulse denotes a logic zero bit, a  $2 \mu s$  wide pulse denotes a logic one bit. As an example, the timing diagram shown in Figure 6.5 is the encoding for the time 12.34567 seconds with the error code 0000. This TOT-like encoding allows HAWC to use the same software to read both the FEB outputs and the time-stamps.

Besides these major modules, the Clock Firmware has a VME module that provides an A24D16 VME interface and several FIFOs. These FIFOs are filled with the information that users need to monitor the health of the GPS Timing System.

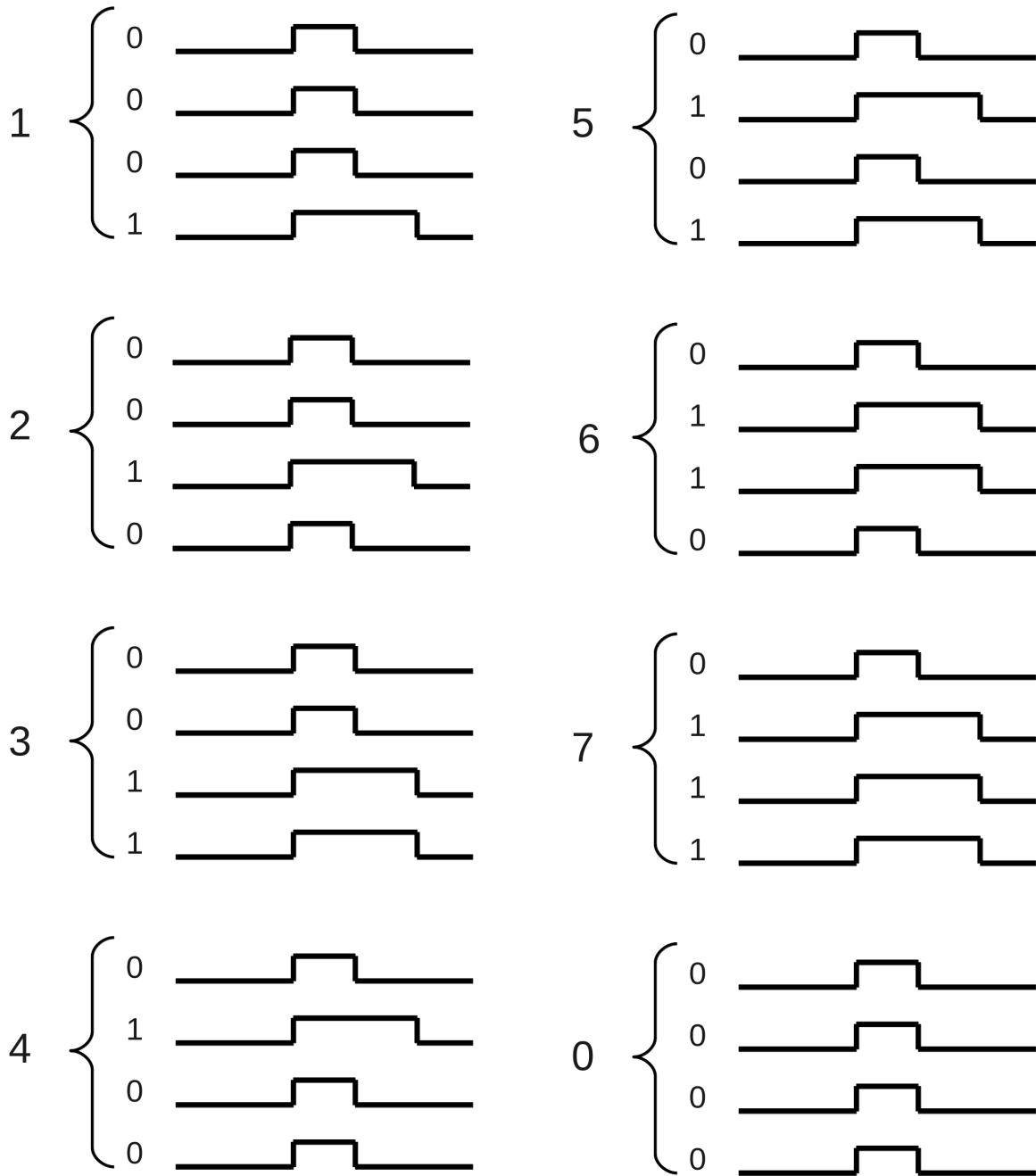


Figure 6.5: Encoding of the time-stamp 12.34567 seconds with no errors is shown. Each digit is encoded into a 4 bit binary number, and each binary number is then encoded into a pulse. A  $1\mu\text{s}$  wide pulse is used to indicate logic 0 and, a  $2\mu\text{s}$  wide pulse is used to indicate logic 1.

Error Code	Error
xxx1	Internal Clock was over written by the current GPS clock.
xx1x	GTC system lost communication with the GPS receiver.
x0xx	GPS receiver do not have enough satellite reception to make a GPS Fix.
1xxx	NMEA string coming from the GPS receiver has errors.

Table 6.1: The error status corresponding to each time-stamp is encoded into the 4 most significant bits of the time-stamp The meaning of each error code is shown.

### 6.2.3 Control System Hardware

The Control System is made from two custom VME boards to provide several services to HAWC: 1) keep all the TDCs working synchronously , 2) issue a synchronous trigger signal to the TDCs, and 3) issue a trigger signal and send the status of the detector to the scaler system. The functional block diagram of the Control system is shown in Figure 6.6.

The H\_Clock: Control card and CB\_Fan card shown in Figure 6.6 are the two custom VME boards. The H\_Clock card used in the Control system (Control type H\_Clock) is a version of the H\_Clock card with 6 input ports and 4 output ports. The CB\_Fan card is a 2 unit wide 6U VME-64X module that is designed primarily to provide appropriate level conversions and fan-outs for the interface between the Control type H\_Clock Card and the TDCs. A photograph of a fully assembled CB\_Fan card is shown in Figure 6.7.

In contrast to the Clock type H\_Clock card, the Control type H\_Clock card gets the 40 MHz global clock signal from the Clock card. Then the Control type H\_Clock Card makes several copies of this 40 MHz clock signal, and distributes them to the 17<sup>th</sup> signal pair of the 10 GPIO connectors and to the FPGA. One input GPIO port and one output GPIO port of the Control type H\_Clock card is connected to the scaler system. The other GPIO ports are connected to two CB\_Fan cards.

The interface of the Control type H\_Clock Card to the Scaler system consists of 4 output signals and one input signal: 10 MHz reference, Pause Pulses, Busy Pulses, LNE, and LNE

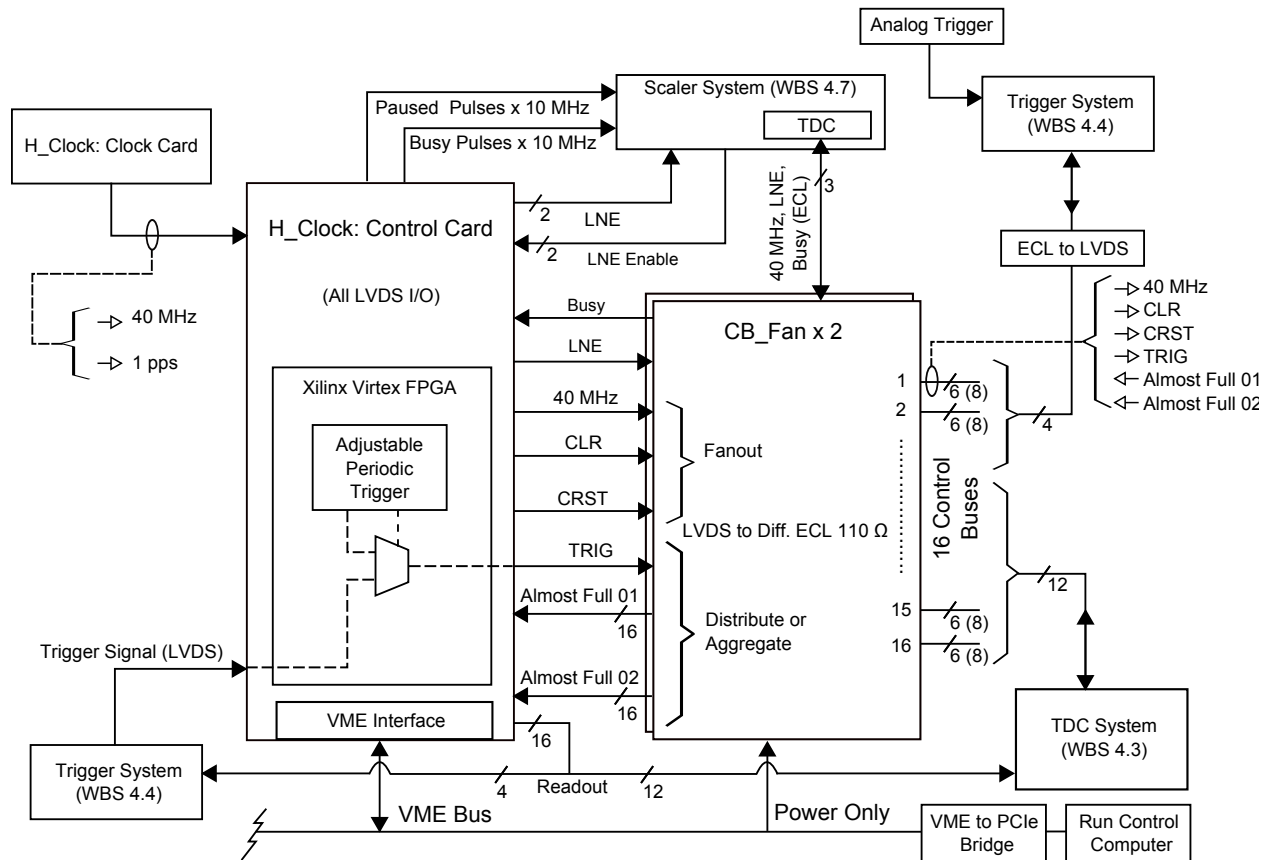


Figure 6.6: A block diagram of the Control System. The Control system consists of two VME cards: the Control Card and CB\_Fan card. The Control card does all the logical operations and the CB\_Fan card does the appropriate level conversion to interface TDCs to the Control Card.

Enable input. The 10 MHz reference is a continuous 10 MHz square wave signal output. The Pause Pulses produce a 10 MHz signal in-phase with the 10 MHz reference when the Control system is in the pause state. The scaler system counts both of these signals. The ratio of the number of pause pulses to the number of 10 MHz reference pulses gives the dead time of the detector. The functionality of the Busy Pulse output is similar to the Pause Pulses except Busy Pulses produce a 10 MHz signal when at least one TDC is almost full. The LNE (Load Next Event) is the trigger signal for the scaler system, which is a periodic signal.

The interface of the Control type H.Clock Card to the CB\_Fan cards consist of four

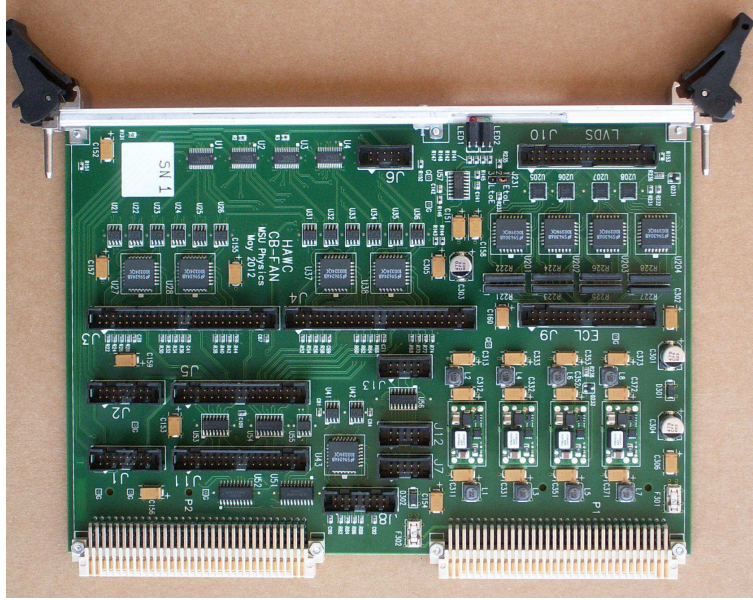


Figure 6.7: A photograph of the fully assembled CB\_Fan card is shown. A CB\_Fan card is able to provide the level conversions and Fan-outs required to handle 6 TDCs.

output signals and 16 input signals per card: 40 MHz, CLR, CRST, TRIG and 16 Almost Full. The Control card makes four identical copies of all its output signals and can accept up to 64 inputs. Therefore, one Control type H\_Clock Card can be connected to four CB\_Fan cards. The four output signals (40 MHz, CLR, CRST, TRIG) and the input signals (Almost Full) of the Control type H\_Clock Card are the control bus signals of the TDC. But the TDCs can not directly connect to the Control type H\_Clock Card, because these I/Os are LVDS signals but the TDC control bus is compatible with only ECL signals. Therefore, the CB\_Fan card is designed to provide the level shifting from Control type H\_Clock Card LVDS outputs to ECL and TDC ECL outputs to LVDS. Apart from the level shifting, the CB\_Fan card makes 6 identical copies of the 40 MHz, CLR, CRST and TRIG signals. Therefore, one CB\_Fan card can be used to control up to 6 TDCs. Since one Control type H\_Clock Card can interface with 4 CB\_Fan cards, the GTC system is capable of controlling up to 24 TDCs. Each CB\_Fan card also fan-out three copies of the LVDS signal type control buses. These

control buses are not used in the current design.

## 6.2.4 Control System Firmware

A simplified functional block diagram of the Control firmware is shown in Figure 6.8. Similarly to the Clock firmware, this firmware is a sequential logic design implemented in VHDL. However, unlike the Clock firmware, individual modules of the Control firmware are not connected sequentially. Coordination of these modules are done through the VME module.

The first module shown in Figure 6.8 is the Trigger module, which coordinates the trigger signals that go to the TDCs. The trigger module can work in three modes: pause, periodic trigger and external trigger. In the pause mode, the trigger module is not issuing any triggers. In the periodic trigger mode, the trigger module issues a periodic trigger signal with a known frequency that is set by the VME module. In the external trigger mode, the trigger module issues a trigger signal upon a request coming from the external trigger. This trigger mode so far not has been used in HAWC. In a typical HAWC data taking run, the trigger module runs in the periodic trigger mode with a trigger frequency of 40 kHz. At the end of each run, the HAWC experiment control system sends a request to the VME module to switch the trigger module to the pause mode. The 40 kHz periodic trigger frequency was chosen because it is the optimum trigger frequency that could be handled by the HAWC DAQ system. However, this periodic trigger frequency can be changed by the run control system sending a request to the VME module. The CLR and CRST modules issue the clear and reset signals to the TDCs upon a request coming from the VME module. These requests come to the VME module from the run control system at the beginning of each run.

The next three modules in Figure 6.8 provide signals to the scaler system. The func-



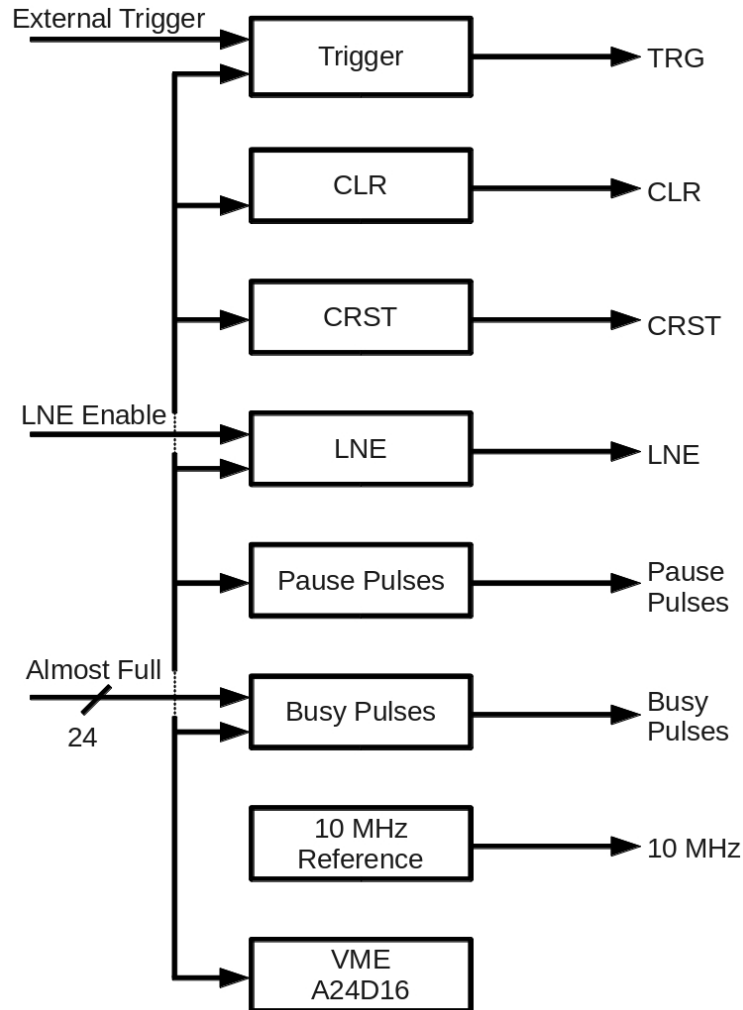


Figure 6.8: A simplified functional block diagram of the Control firmware is shown. The Trigger, CLR, and CRST modules generate the TDC control signals, and LNE, Pause Pulses, Busy Pulses and 10 MHz Reference produces signals to the scaler system. Similar to the Control firmware, communication between the Control system and the control computer was done by a A24D16 VME interface.

tionality of the Pause Pulse module is equivalent to a multiplexer with two inputs and one output: Logic Lo input, 10 MHz square wave input and Pause Pulse output. When the Trigger module is in the Pause state the Pause Pulse output switches to the 10 MHz square wave. When the Trigger module is not in the Pause state, the output switches to the Logic Lo level. The Busy Pulse module has a similar functionality, except selection between Logic Lo and 10 MHz square is done using the OR of the Almost Full signals. If any of the Almost

Full inputs are Logic Hi, the Busy Pulse output gets connected with the 10 MHz square wave, otherwise the out put stays in the Logic Lo level. The 10 MHz Reference module is a 10 MHz square wave signal generator that generates a reference pulse stream to the scaler system.

### 6.3 Performance of the GTC system

The fully functional GTC system was integrated with the HAWC 30 array (30 tanks) in October, 2012. The operation of HAWC 30 with 4 PMTs in each tank needed only 120 TDC channels ( $30 \times 4$ ) to record PMT signals. Therefore, 1 TDC was enough to record the PMT signals, and 32 channels from a second TDC was used to record the time-stamps.

At the beginning of HAWC 30 operations we were concerned about getting missing edges of the time stamps. Therefore, we configured the GTC system to issue a periodic time-stamp every  $10 \mu s$ , and the TDCs to record the data in a  $25.2 \mu s$  time window. In this configuration two time-stamps are guaranteed for each trigger window. After analyzing data from 8 months we did not find any time-stamps with missing edges. Therefore, the frequency of time-stamps was reduced to one time-stamp per  $20 \mu s$ . With these settings, only one time-stamp is guaranteed for each trigger window. This new configuration reduces the band width of the TDC readout by 50%.

The health of the GTC system has been continuously monitored since early 2013, and it has revealed that the 1PPs signal has a jitter of less than 50 ns with respect to the 10 MHz output. Each time the 1PPs signal jitters more than 25 ns the GPS clock over writes the GTC internal clock, and the firmware produces an error flag in the time-stamp. The average rate of this error flag was 11 per hour. This jitter introduced an upper limit of 50 ns accuracy

to the GTC generated time-stamp. The 25 ns accuracy is well below the required accuracy of  $1\mu\text{s}$  for HAWC. The Clock firmware was upgraded in October 2013 to be immune to this jitter.

The GTC health monitoring system is also continuously monitoring the GPS Fix status and Time Dilution of Precision. During the period from October 2012 to November 2013 the GPS Fix was lost only once. The GPS receiver was able to recover the lost GPS Fix within 5 minutes. The internal clock was not over written by the GPS time after the GPS receiver recovered from the lost GPS Fix. This observation yields the conclusion that the internal clock of the GTC system was able to maintain its internal clock during that 5 minutes without the assistance of the GPS receiver. During the period from October 2012 to November 2013 the Time Dilution of Precision (TDOP) was in the excellent range ( $\text{TDOP} < 2$ ) for 95% of the time and was in the good range ( $2 < \text{TDOP} < 5$ ) 4.9% of the time. There were few occurrences, 0.1% of the time, with moderate ( $5 < \text{TDOP} < 10$ ) Time Dilution of Precision.

## 6.4 Additional Capabilities of H\_Clock cards

Since H\_Clock cards are made with a re-programmable FPGA, H\_Clock cards can be used for different applications. As a part of my service work projects, I developed the HAWC pattern generator and Scaler Time Stamp reader using spare H\_Clock cards. The HAWC pattern generator was made from a Clock type H\_Clock card. This pattern generator is able to produce TOT-like signals that are similar to the output signals of the front-end electronic boards. A key feature of this pattern generator is that the patterns are not hard-coded. The patterns can be configured through special software.

The Scaler Time Stamp reader was made from a Control type H\_Clock card. The purpose of the Scaler Time Stamp reader is to read time-stamps produce by the GPS Timing system and store them in a FIFO to be read through the VME back-plane. The Scaler Time Stamp reader was integrated with the scaler system in May 2013.

# Chapter 7

## Data Analysis Methodology

In the Milagro skymaps, the expected significance at a sky location with no true emission is a Gaussian random variable with mean 0 and unit standard deviation [Atkins et al.(2004)]. A common treatment of  $N$  candidate searches is to use a trials correction technique. Here one can choose a significance threshold, calculate the tail probability (p-value)  $\lambda$ , and adjust the p-value threshold to  $\frac{\lambda}{N}$ . The purpose of the trials correction is to maintain, at the value  $\lambda$ , the probability of a background fluctuation producing one or more false discoveries among the  $N$  searches. The False Discovery Rate (FDR) technique discussed in [Miller et al.(2001)] offers some advantages over the trials correction technique. In Section 7.1 I briefly discuss the FDR technique. The FDR technique can be used to search for individual candidates with a TeV association. A stacking analysis can be used to search for evidence of collective TeV emission among the undetected candidates by studying their mean flux. In Section 7.2 I briefly discuss the stacking analysis used in this thesis.

## 7.1 False Discovery Rate method

Instead of controlling the expected probability of having even one false detection, FDR controls the expected fraction of false discoveries among a set of detections; that is, it controls the contamination fraction of the lists of associations, rather than the probability of a random individual association being accepted. The key input parameter is again a probability  $\lambda$ , but now  $\lambda$  represents the expected fractional contamination of any announced set of detections. Based on this input parameter, the method dynamically adjusts the detection threshold but in a way that depends on the properties of the entire list of search significances (converted into p-values). This dynamic adjustment is sensitive to whether the distribution of p-values is flat (as would be expected if there were no detectable sources) or skewed to small p-values (i.e. large significances). This adjustment lowers the significance threshold for detection if a list is a “target-rich environment” in such a way that the expected fraction of false discoveries among the announced detections remains at the fraction  $\lambda$ . In particular, the most significant candidate is required to have a p-value of  $\lambda/N$  just as in the trials-correction method, but the  $n$ -th most significant candidate need only have a p-value less than  $\lambda \times n/N$ . As a result, this technique has a higher efficiency for finding real detections, while producing the same results as a trials-correction method in target-poor environments where the only decision is whether to report zero or one detection. The method adjusts for both the length of the search list and the distribution of the significances found within the search list. Note that as a result, a given candidate location might pass the FDR criteria on one search list, but fail in another. Also note that  $\lambda$  controls the expected contamination, i.e. averaged over potential lists of associations, not the contamination fraction on a specific list.

### 7.1.1 Calculation

Calculation of the FDR threshold have 4 main steps. First the parameter  $\lambda$  has to be selected, such that  $0 < \lambda < 1$ . The FDR procedure guarantees that the average rate of false discoveries is less than or equal to  $\lambda$ . The second step is to calculate the corresponding  $P$  values for each candidate. Let  $P_1, \dots, P_j, \dots, P_N$  denote the P-values correspond to  $N$  candidates that are listed from smallest to largest P-value. The third step is to find the maximum  $j$  value that satisfies,

$$j_{max} = \max\{j : P_j < \frac{j\lambda}{c_N N}\}, \quad (7.1)$$

where  $c_N = 1$  when the P-values are based on statistically independent tests. If the P-values are dependent,

$$c_N = \sum_{i=1}^N i^{-1}. \quad (7.2)$$

The last step is to reject all hypotheses with  $P_j < P_{j_{max}}$ .

## 7.2 Stack Analysis

A stacking analysis can be used to search for evidence of collective TeV emission among the undetected candidates by studying their mean flux. This thesis used the stacking methodology of Section 3 in [Kurczynski & Gawiser(2010)]. The significance of the stacked flux is given by Equation 7.3 below.

$$\text{Significance} = \frac{\langle I \rangle}{\sqrt{V(\langle I \rangle)}}, \quad (7.3)$$

where  $\langle I \rangle$  is the weighted average flux as defined in Equation 7.4 below and  $\vee \langle I \rangle$  is its variance, defined in Equation 7.5.

$$\langle I \rangle = \frac{\sum \frac{I_i}{\sigma_i^2}}{\sum \frac{1}{\sigma_i^2}} \quad (7.4)$$

$$\vee \langle I \rangle = \frac{\sum \frac{1}{\sigma_i^2}}{\sum \left( \frac{1}{\sigma_i} \right)^2} \quad (7.5)$$

Here  $I_i$  is the flux of each candidate and  $\sigma_i$  is the standard deviation of flux of each candidate.



# Chapter 8

## Milagro Observations of Extragalactic Sources

The Milagro collaboration performed blind searches of the Milagro sky maps and found a number of TeV sources ([Atkins et al.(2004)] and [Abdo et al. (2007)]). Blind searches for excess events over the full sky have a high probability of picking up random fluctuations. Therefore after trials correction, a full sky blind search is less sensitive than searches using a predefined list of potential TeV emitting candidates. Therefore, I performed three targeted searches for extragalactic sources using the existing Milagro sky maps. This chapter discusses the results from these three targeted searches.

The first extragalactic candidate list is compiled from the extragalactic sources in the Fermi-LAT second source catalog (2FGL) [Nolan et al.(2012)]. The second extragalactic candidate list is made from the extragalactic sources in the TeVCat catalog [Wakely & Horan(2008)]. All of the TeVCat extragalactic sources were detected by IACTs. Measurements available in TeVCat include the transient states of variable extragalactic sources. The analysis pre-

sented in Section 8.2 searched for the time average flux of those candidates by averaging their flux over approximately 8 years. The third and last extragalactic candidate list is compiled from a list of potential TeV emitting BL Lac objects that were theoretically predicted by L. Costamante and G. Ghisellini 2002. The analysis presented in Section 8.3 searched for the TeV emission associated with these BL Lac objects.

In order to optimize the sensitivity to extragalactic sources, these three searches used a Milagro sky map made with a power law spectrum with an exponential cutoff,  $E^{-2.0} e^{-\frac{E}{5\text{TeV}}}$ . This choice reflects the fact that when TeV gamma-rays travel cosmological distances they are attenuated due to interactions with photons from the extragalactic background light [Dwek & Krennrich(2005)]. This means that the energy spectrum of extragalactic sources is cut off at high energies. This spectral assumption is similar to the power law spectral index and the cut-off energy measured for Markarian 421 and Markarian 501 by VERITAS [Krennrich et al.(2001)]. The detection thresholds for these searches were obtained using the False Discovery Rate (FDR) technique, discussed in Section 7.1, with a 1% contamination fraction.

## 8.1 Targeted Search for 2FGL Extragalactic Sources

The 2FGL catalog has 1808 sources off the Galactic plane ( $|l| > 10^0$ ) that have no associations with known galactic sources. From these extragalactic sources 709 were within Milagro's sky coverage ( $-7^\circ < \text{DEC} < 80^\circ$ ), of which 72% have spatial associations with blazars. Among these blazars 4 are firmly identified as BL Lac blazars and 12 are firmly identified as FSRQ<sup>1</sup> type blazars.

---

<sup>1</sup>Flat Spectrum Radio Quasar

In this list only 2FGL J1104.4+3812 (also known as Markarian 421) is classified as a source by the FDR procedure with a 1% contamination. The Milagro sky map of a  $5^\circ \times 5^\circ$  region around the Fermi-LAT position of the Markarian 421 is shown in Figure 8.1. This is a  $9.57\sigma$  detection and the measured differential photon flux is  $3.89 \pm 0.4 \times 10^{-15}$  photons  $\text{TeV}^{-1}\text{s}^{-1}\text{cm}^{-2}$  at 7 TeV. Table 8.2 gives the 95% confidence level flux upper limit for the brightest 20% in the energy band of 3 to 10 GeV in this list.

### 8.1.1 Comparison with Previous $\gamma$ -ray Flux Measurements

Markarian 421 is one of the closest ( $z=0.030$ ) known, best studied TeV photon emitting blazars. Markarian 421 was discovered to emit TeV photons by Whipple in 1992 [Punch et al.(1992)]. Since then, Markarian 421 has been observed by several gamma-ray observatories and identified as the source with the fastest observed TeV flux variation [Albert et al.(2007)]. The gamma-ray emission from Markarian 421 is known to have multiple states: high flux states and a low flux states. The gamma-ray flux at a high flux state was measured by the H.E.S.S. observatory between April and May of 2004. The measured gamma-ray flux between 1.5 and 10 TeV was found to vary by a factor of  $\sim 4$  on a time scale of days, and the averaged differential energy distribution was consistent with a power law with an exponential cutoff of:

$$\frac{dN}{dE} = \left(1.55 \pm 0.08_{stat} \pm 0.4_{sys} \times 10^{-10}\right) (E \text{ TeV})^{-2.1 \pm 0.1_{stat} \pm 0.3_{sys}} \exp\left(-E/(3.1 \pm 0.4_{stat} \pm 0.9_{sys} \text{ TeV})\right) \quad (8.1)$$

The MAGIC telescope observed Markarian 421 between November, 2004 and April, 2005 [Albert et al.(2007)], when it was considered to be in a low flux state. The measured gamma-

State	Differential flux photons $\times 10^{-15}$ $\text{TeV}^{-1}\text{s}^{-1}\text{cm}^{-2}$ at 7 TeV
Milagro Average Flux	$3.89 \pm 0.4$
High Flux State	$270^{+170}_{-110}$ (H.E.S.S.)
Low Flux State	$4.98^{+9.45}_{-3.69}$ (MAGIC)

Table 8.1: The gamma-ray flux of Markarian 421 at 7 TeV in the high flux state, low flux state and the average flux is summarized

ray flux between 100 GeV and 3 TeV was also found to vary by a factor of 4 on a scale of days, and the averaged differential energy distribution was consistent with a power law with an exponential cutoff of:

$$\frac{dN}{dE} = \left(0.45 \pm 0.01 \times 10^{-10}\right) (E)^{-2.20 \pm 0.08} \exp(-E/(1.44 \pm 0.27 \text{ TeV})) \quad (8.2)$$

Contrasted with these two measurements, the Milagro flux measurement is the average flux over approximately eight years. The gamma-ray flux of Markarian 421 at 7 TeV in the high flux state, low flux state and the average flux is summarized in Table 8.1.1. The Milagro flux measurement of the average flux over approximately eight years is less than the flux measured by MAGIC at a low flux state. Therefore, the Milagro time average flux measurement suggests that Markarian 421 has lower flux states than the low flux state measured by MAGIC, and Markarian 421 stays in a lower flux state for most of the time.

### 8.1.2 Undetected Candidates

Milagro also observed a signal excess at the Fermi-LAT sky locations of Markarian 501 ( $2.9\sigma$ ), TXS 1720+102 ( $2.8\sigma$ ) and 1ES 0502+675 ( $2.5\sigma$ ). Their significances are 2.93, 2.84 and 2.53 respectively, which is insufficient to pass the FDR cut of 1% contamination ( $\lambda = 0.01$ ). Among these three candidates, Markarian 501 and 1ES 0502+675 have been already reported

as TeV sources in TevCat. However, TXS 1720+102 has not yet been identified as a source with TeV emission. This is a radio quasar type blazar identified at a red shift of 0.732 [Afanas'Ev et al.(2005)]. The lowest FDR cut that TXS 1720+102 passes is  $\lambda = 0.32$ . With this looser FDR cut, three candidates become TeV associations: Markarian 421, Markarian 501 and TXS 1720+102. However, the expected contamination of the resulting candidates list is 32% so it is likely that TXS 1720+102 is a background fluctuation. While it is hard to advocate a dedicated IACT observation of TXS 1720+102, a clearer answer to whether this is a background fluctuation will be provided by HAWC, which is a survey type instrument.

The FDR method is capable of identifying individual candidates which have a TeV association. However, there might be some collective TeV emission coming from the candidates that fail the  $\lambda = 0.01$  FDR cut. I searched for evidence of collective TeV emission on the candidates that fail the  $\lambda = 0.01$  FDR cut by using the stacking method described in Section 7.2 . I stacked the 2FGL Extragalactic candidates in two different ways: first all FDR False 2FGL Extragalactic sources and then the FDR False sources among the brightest 20% in the Fermi energy band 3-10 GeV. These two lists had  $0.7\sigma$  and  $0.6\sigma$  significance, respectively. Neither of these stacking results indicate statistically significant collective gamma-ray emission from the rejected candidates.

## 8.2 Targeted Search for TeVCat Extragalactic Sources

As of February 8th, 2012 the TeVCat catalog ([Wakely & Horan(2008)], <http://tevcat.uchicago.edu>) had 135 sources, of which 31 sky locations were off the Galactic plane and within Milagro's sky coverage. These 31 candidates were IACT detections and 23 are identified as BL Lac objects. Among these 31 TeVCat sources only Markarian 421 is classified as a source in Milagro

maps with a 1% contamination. Stacking the TeVCat candidates other than Markarian 421, gives a  $0.9\sigma$  upward fluctuation. This is a slightly higher upward fluctuation than the 2FGL extragalactic sources stacking. However, this still does not indicate a significant collective gamma-ray emission from the rejected candidates.

Among the candidates that fail the  $\lambda = 0.01$  FDR cut, TeVCat reports Markarian 501 as a well studied, nearby ( $z=0.034$ ) TeV emitting blazar. Milagro observed a  $2.93\sigma$  positive excess for Markarian 501, and the measured 95% confidence upper limit is  $1.8 \times 10^{-15}$  photons  $\text{cm}^{-2}\text{s}^{-1}\text{TeV}^{-1}$  at 7 TeV. Similar to Markarian 421, Markarian 501 is also known as a blazar with extreme spectral variability [Acciari et al.(2011)]. Most of the studies of Markarian 501 were done during its high flux states. The HEGRA observatory observed that during the high flux states (during the strong outburst in 1997) Markarian 501's spectral energy distribution has an exponential cut off at  $\approx 6 - 8$  TeV [Aharonian et al.(1999)] and [Aharonian et al.(2001)]. However, only a few gamma-ray observations have been performed when Markarian 501 is in the low flux state (also known as the quiescent-state). In 2001, a group of physicists performed a combined multiwavelength observation campaign to measure the Markarian 501 flux at its quiescent state [Acciari et al.(2011)]. In this campaign both VERITAS and MAGIC were utilized to measure the TeV flux in the energy range from  $\sim 0.2$  to  $\sim 3$  TeV. The TeV gamma-ray spectrum measured by both instruments was compatible with a simple power law spectrum.

$$\frac{dN}{dE} = I_0 \times 10^{-12} \times \left( \frac{E}{1 \text{ TeV}} \right)^{-\alpha} \quad (8.3)$$

For the VERITAS measurements, the best-fit parameters are  $\alpha = 2.72 \pm 0.15_{stat} \pm 0.1_{sys}$  and  $I_0 = 5.78 \pm 0.83_{stat} \pm 1.16_{sys}$ , and for the MAGIC measurement, the best-fit parameters

are  $\alpha = 2.67 \pm 0.21_{stat} \pm 0.2_{sys}$  and  $I_0 = 8.34 \pm 1.53_{stat} \pm 2.50_{sys}$ . The extrapolation of these spectra gives the differential flux of  $2.9^{+1.5}_{-1.0} \times 10^{-14}$  and  $4.6^{+3.5}_{-2.1} \times 10^{-14}$  photons  $\text{cm}^{-2}\text{s}^{-1}\text{TeV}^{-1}$  at 7 TeV. Both of these extrapolated fluxes without a cutoff are above the Milagro upper limit within their error bars. Therefore, I can conclude that the flux derived at 7 TeV by extrapolating a pure power law SED of Markarian 501 is an over-estimate. This suggests a power law spectrum with an exponential cut between 3 and 7 TeV for the Markarian 501 spectrum.

### 8.3 Targeted Search for Potential TeV Emitting BL Lac Objects

The observations of blazars by the Energetic Gamma-Ray Experiment Telescope (EGRET) on NASA's Compton Gamma-Ray Observatory satellite led to the discovery that blazars emit most of their power in the gamma-ray band [Costamante & Ghisellini(2002)]. The EGRET measured spectral energy distributions (SEDs) of the blazars were best characterized by two broad peaks, which are explained as synchrotron and Inverse Compton radiation. L. Costamante and G. Ghisellini studied these two-peak SEDs from the EGRET and three other blazar samples available at that time (before year 2002), and developed a model to predict a list of TeV emitting blazars from a subclass of blazars known as BL Lacs [Costamante & Ghisellini(2002)]. Of this candidate list, 27 fall within the Milagro sky coverage ( $-7^\circ < \text{DEC} < 80^\circ$ ). One method to constrain this model is to search for TeV emission from these 27 BL Lac candidates and compare with the predictions. Therefore, Elizabeth A. Hays performed a targeted search for this list of BL Lac candidates in the 2.7 year long Milagro archived data set [Hays(2004)]. In her search, she did not find significant

TeV emission from any of these TeV BL Lac candidates.

Since then the Milagro archived data set has grown by about a factor of three, and Milagro's background rejection capability has substantially improved [Abdo(2007)]. Therefore, I re-performed a targeted search for this list of TeV BL Lac candidates in the eight year long Milagro archived data set. In addition to the larger data set and the new background rejection capability, the Milagro map I used in my analysis was optimized for a spectral distribution of  $E^{-2.0} \exp(-E/5 \text{ TeV})$ , which increases the sensitivity to extragalactic sources.

Even though the new search was performed in a more sensitive Milagro data set, it was still not sensitive enough to detect these TeV BL Lac candidates [Abeysekara & Milagro Collaboration(2013)]. Stacking of these candidates shows only a  $0.28\sigma$  deviation from the background, which does not indicate a significant collective gamma-ray emission. A graphical comparison between the theoretically predicted TeV flux at 7 TeV, Milagro's upper limit of each sky location at 7 TeV, and the 95% expected upper limit of the flux for extragalactic sources in each declination band corresponding to zero excess derived at 7 TeV is shown in Figure 8.2.

These results show that Milagro doesn't observe collective or individual gamma-ray emission from these candidates. Therefore, the Milagro measurements were not able to constrain L. Costamante and G. Ghisellini's proposed model. However, these Milagro measurements do provide upper limits to estimate the TeV cutoffs for new models. Since Figure 8.2 provides the expected upper limit at 95% confidence level for all the declination bands between  $-7^\circ$  and  $80^\circ$ , a theoretician can use these limits to estimate the TeV cutoffs of any source in Milagro sky coverage.



Fermi Name 2FGL	RA (deg)	DEC (deg)	l (deg)	b (deg)	Flux/Flux Limit ( $\times 10^{-17} \text{TeV}^{-1}$ $\text{s}^{-1} \text{cm}^{-2}$ )	Source Type	Significance $\sigma$	Associated source
J0007.8+4713	1.97	47.23	115.3	-15	< 65.06	bzb	-0.78	MG4 J000800+4712
J0009.1+5030	2.29	50.51	116.09	-11.8	< 85.8	agu	-0.26	NVSS J000922+503028
J0022.5+0607	5.64	6.12	110.02	-56.02	< 279.67	bzb	-0.1	PKS 0019+058
J0045.3+2127	11.34	21.45	121.04	-41.4	< 120.71	bzb	0.48	GB6 J0045+2127
J0100.2+0746	15.06	7.78	126.74	-55.03	< 378.43	bzb	1.69	GB6 J0100+0745
J0106.5+4854	16.65	48.91	125.49	-13.88	< 95.99		0.21	
J0108.6+0135	17.17	1.59	131.85	-60.98	< 566.7	bzq	0.64	4C 1.02
J0112.1+2245	18.03	22.76	129.15	-39.86	< 63.03	bzb	-1.29	S2 0109+22
J0112.8+3208	18.21	32.14	128.19	-30.51	< 48.2	bzq	-1.71	4C 31.03
J0115.4+0358	18.87	3.97	134.43	-58.37	< 296.62	bzb	-0.59	PMN J0115+0356
J0136.5+3905	24.14	39.09	132.42	-22.95	< 70.3	bzb	-0.46	B3 0133+388
J0136.9+4751	24.24	47.86	130.78	-14.32	< 117.84	bzq	0.89	OC 457
J0144.6+2704	26.16	27.08	137.29	-34.31	< 85.04	bzb	-0.03	TXS 0141+268
J0153.9+0823	28.49	8.4	148.21	-51.38	< 209.19	bzb	-0.2	GB6 J0154+0823
J0211.2+1050	32.81	10.84	152.59	-47.39	< 106.04	bzb	-1.48	MG1 J021114+1051
J0217.4+0836	34.35	8.61	156.17	-48.63	< 138.64	bzb	-1.14	ZS 0214+083
J0217.9+0143	34.48	1.73	162.2	-54.41	< 347.2	bzq	-0.84	PKS 0215+015
J0221.0+3555	35.27	35.93	142.6	-23.49	< 85.82	bzq	0.21	S4 0218+35
J0222.6+4302	35.66	43.04	140.14	-16.77	< 85.18	BZB	0.13	3C 66A
J0237.8+2846	39.47	28.78	149.48	-28.55	< 101.74	bzq	0.58	4C 28.07
J0238.7+1637	39.68	16.62	156.78	-39.1	< 131.21	BZB	0.24	AO 0235+164
J0316.1+0904	49.05	9.08	172.1	-39.59	< 339.0	bzb	1.59	GB6 J0316+0904
J0319.8+4130	49.97	41.51	150.58	-13.25	< 74.54	rdg	-0.15	NGC 1275
J0326.1+0224	51.55	2.41	180.74	-42.45	< 802.03	bzb	1.66	1H 0323+022
J0333.7+2918	53.43	29.31	160.49	-21.49	< 103.39	agu	0.62	TXS 0330+291
J0423.2-0120	65.81	-1.34	195.28	-33.15	< 1039.11	BZQ	1.35	PKS 0420-01
J0433.5+2905	68.39	29.09	170.52	-12.62	< 114.07	bzb	0.93	MG2 J043337+2905
J0442.7-0017	70.69	0.29	197.21	-28.44	< 863.75	bzq	1.04	PKS 0440-00
J0448.9+1121	72.24	11.36	187.4	-20.77	< 198.53	bzq	0.41	PKS 0446+11
J0508.0+6737	77.01	67.63	143.8	15.9	< 648.35	bzb	2.53	1ES 0502+675
J0509.4+0542	77.37	5.7	195.4	-19.62	< 320.94	bzb	0.34	TXS 0506+056
J0532.7+0733	83.19	7.56	196.84	-13.71	< 275.2	bzq	0.68	OG 50
J0534.8-0548c	83.72	-5.81	209.36	-19.66	< 942.7		-1.51	
J0541.8-0203c	85.45	-2.06	206.69	-16.41	< 1007.43		0.66	
J0547.1+0020c	86.8	0.34	205.15	-14.1	< 666.58		0.24	
J0607.4+4739	91.87	47.66	165.64	12.87	< 76.14	bzb	-0.4	TXS 0603+476
J0612.8+4122	93.21	41.37	171.83	10.92	< 86.2	bzb	0.24	B3 0609+413
J0650.7+2505	102.7	25.1	190.24	11.02	< 45.99	bzb	-2.17	1ES 0647+250
J0654.2+4514	103.57	45.24	171.2	19.36	< 77.21	bzq	-0.14	B3 0650+453
J0654.5+5043	103.65	50.72	165.68	21.14	< 164.55	bzq	1.79	GB6 J0654+5042
J0714.0+1933	108.51	19.57	197.68	13.61	< 103.44	bzq	-0.03	MG2 J071354+1934
J0719.3+3306	109.83	33.11	185.06	19.85	< 115.37	bzq	1.02	B2 0716+33
J0721.9+7120	110.48	71.35	143.97	28.02	< 512.3	bzb	0.49	S5 0716+71
J0725.3+1426	111.33	14.44	203.63	13.93	< 169.64	BZQ	0.49	4C 14.23
J0738.0+1742	114.52	17.7	201.85	18.06	< 152.56	bzb	0.83	PKS 0735+17

Table 8.2: Summary of the search with  $\lambda = 0.01$  for TeV emission from the 2FGL list that are identified as candidates off the galactic plane. (Note that we used the same abbreviations for the source type as the 2FGL, agu = active galaxy of uncertain type, bzb = BL Lac type of blazar and bzq = FSRQ type of blazar.) The Milagro flux derived at 7 TeV is given for candidates that passed the  $\lambda = 0.01$  FDR cut and the 95% confidence level flux upper limit is given for the rest.

Table 8.2: (cont'd)

Fermi Name 2FGL	RA (deg)	DEC (deg)	l (deg)	b (deg)	Flux/Flux Limit ( $\times 10^{-17} \text{TeV}^{-1}$ $\text{s}^{-1} \text{cm}^{-2}$ )	Source Type	Significance $\sigma$	Associated source
J0739.2+0138	114.82	1.65	216.96	11.39	< 293.61	bzq	-1.35	PKS 0736+01
J0805.3+7535	121.34	75.59	138.88	30.79	< 1032.12	bzb	-0.11	RX J0805.4+7534
J0807.1-0543	121.78	-5.72	227	13.99	< 1883.54	bzb	0.61	PKS 0804-05
J0809.8+5218	122.46	52.31	166.26	32.91	< 136.9	bzb	1.07	0806+524
J0818.2+4223	124.57	42.4	178.21	33.41	< 113.39	bzb	1.15	S4 0814+42
J0831.9+0429	127.99	4.49	220.72	24.36	< 417.64	bzb	0.4	PKS 0829+046
J0854.8+2005	133.71	20.1	206.83	35.83	< 93.21	BZB	-0.35	OJ 287
J0905.6+1357	136.4	13.96	215.04	35.96	< 190.04	bzb	0.88	MG1 J090534+1358
J0909.1+0121	137.29	1.37	228.93	30.92	< 576.86	bzq	0.19	PKS 0906+01
J0909.7-0229	137.43	-2.5	232.8	28.99	< 476.09	bzq	-1.54	PKS 0907-023
J0915.8+2932	138.96	29.54	196.67	42.93	< 134.29	bzb	1.58	B2 0912+29
J0920.9+4441	140.24	44.7	175.7	44.81	< 107.06	bzq	0.84	S4 0917+44
J0957.7+5522	149.43	55.38	158.59	47.94	< 86.48	bzq	-0.63	4C 55.17
J1012.6+2440	153.17	24.68	207.74	54.36	< 77.99	bzq	-0.37	MG2 J101241+2439
J1015.1+4925	153.79	49.43	165.53	52.73	< 124.22	bzb	1.04	1H 1013+498
J1016.0+0513	154.01	5.23	236.51	47.04	< 412.37	bzq	0.74	TXS 1013+054
J1033.9+6050	158.48	60.84	147.8	49.13	< 136.0	BZQ	-0.18	S4 1030+61
J1037.6+5712	159.42	57.21	151.77	51.77	< 89.82	bzb	-0.82	GB6 J1037+5711
J1058.4+0133	164.61	1.57	251.5	52.77	< 451.8	bzb	0.01	4C 1.28
J1058.6+5628	164.67	56.48	149.57	54.42	< 110.53	bzb	0.02	TXS 1055+567
<b>J1104.4+3812</b>	<b>166.12</b>	<b>38.21</b>	<b>179.82</b>	<b>65.03</b>	<b>389.74±40.7</b>	<b>bzb</b>	<b>9.57</b>	<b>Mkn 421</b>
J1117.2+2013	169.31	20.23	225.63	67.39	< 90.1	bzb	-0.45	RBS 958
J1121.5-0554	170.39	-5.91	266.27	50.45	< 2362.34	bzq	1.39	PKS 1118-05
J1132.9+0033	173.23	0.56	264.33	57.42	< 798.62	bzb	1.3	PKS B1130+008
J1150.5+4154	177.63	41.91	159.14	70.67	< 80.64	bzb	0.12	RBS 1040
J1159.5+2914	179.88	29.25	199.41	78.37	< 79.56	bzq	-0.11	Ton 599
J1217.8+3006	184.47	30.11	188.93	82.06	< 74.31	bzb	-0.25	1ES 1215+303
J1221.3+3010	185.35	30.18	186.33	82.74	< 77.42	bzb	-0.12	PG 1218+304
J1221.4+2814	185.37	28.24	201.69	83.28	< 113.67	bzb	0.9	W Comae
J1224.9+2122	186.23	21.38	255.07	81.66	< 168.32	BZQ	1.59	4C 21.35
J1226.0+2953	186.52	29.9	185.02	83.78	< 60.44		-0.87	
J1229.1+0202	187.28	2.04	289.95	64.35	< 459.81	BZQ	0.01	3C 273
J1231.7+2848	187.94	28.81	190.66	85.34	< 54.27	bzb	-1.28	B2 1229+29
J1239.5+0443	189.88	4.73	295.18	67.42	< 405.6	bzq	0.73	MG1 J123931+0443
J1243.1+3627	190.78	36.45	133.13	80.51	< 67.63	bzb	-0.45	Ton 116
J1248.2+5820	192.06	58.35	123.74	58.77	< 107.89	bzb	-0.44	PG 1246+586
J1253.1+5302	193.28	53.05	122.36	64.08	< 72.69	bzb	-0.99	S4 1250+53
J1256.1-0547	194.04	-5.79	305.1	57.06	< 1072.78	BZQ	-1.07	3C 279
J1303.1+2435	195.78	24.6	349.62	86.35	< 117.62	bzb	0.85	MG2 J130304+2434
J1309.4+4304	197.37	43.08	111.17	73.64	< 87.93	bzb	0.26	B3 1307+433
J1310.6+3222	197.67	32.38	85.59	83.29	< 65.29	bzq	-0.68	OP 313
J1312.8+4828	198.21	48.47	113.32	68.25	< 71.38	bzq	-0.57	GB 1310+487
J1418.4-0234	214.6	-2.57	341.56	53.64	< 1091.11	bzb	1.01	BZB J1418-0233
J1427.0+2347	216.76	23.8	29.48	68.2	< 96.03	bzb	0.13	PKS 1424+240
J1438.7+3712	219.68	37.21	63.72	65.27	< 50.77	bzq	-1.33	B2 1436+37B

Table 8.2: (cont'd)

Fermi Name 2FGL	RA (deg)	DEC (deg)	l (deg)	b (deg)	Flux/Flux Limit ( $\times 10^{-17} \text{TeV}^{-1}$ $\text{s}^{-1} \text{cm}^{-2}$ )	Source Type	Significance $\sigma$	Associated source
J1454.4+5123	223.62	51.4	87.66	56.46	< 109.12	bzb	0.49	TXS 1452+516
J1501.0+2238	225.28	22.64	31.46	60.34	< 114.2	bzb	0.55	MS 1458.8+2249
J1504.3+1029	226.1	10.49	11.37	54.58	< 185.18	BZQ	0.0	PKS 1502+106
J1520.8-0349	230.22	-3.83	358.11	42.48	< 820.68	bzb	-0.48	NVSS J152048-034850
J1522.1+3144	230.54	31.74	50.18	57.02	< 101.94	bzq	0.64	B2 1520+31
J1542.9+6129	235.73	61.49	95.38	45.4	< 93.21	bzb	-1.34	GB6 J1542+6129
J1553.5+1255	238.39	12.93	23.77	45.21	< 109.28	bzq	-0.97	PKS 1551+130
J1555.7+1111	238.94	11.19	21.92	43.95	< 160.64	bzb	-0.17	PG 1553+113
J1607.0+1552	241.77	15.88	29.4	43.42	< 85.05	bzb	-1.16	4C 15.54
J1625.2-0020	246.3	0.33	13.92	31.83	< 762.2		0.66	
J1635.2+3810	248.81	38.17	61.13	42.34	< 58.66	bzq	-0.95	4C 38.41
J1637.7+4714	249.43	47.24	73.38	41.88	< 68.76	bzq	-0.6	4C 47.44
J1640.7+3945	250.18	39.76	63.35	41.38	< 122.41	BZQ	1.31	NRAO 512
J1642.9+3949	250.18	39.76	63.48	40.95	< 122.41	BZQ	1.31	3C 345
J1640.7+3945	250.75	39.83	63.35	41.38	< 115.23	BZQ	1.11	NRAO 512
J1642.9+3949	250.75	39.83	63.48	40.95	< 115.23	BZQ	1.11	3C 345
J1653.6-0159	253.4	-2	16.59	24.93	< 847.78		0.15	
J1653.9+3945	253.48	39.76	63.61	38.85	< 186.65	BZB	2.93	Mkn 501
J1700.2+6831	255.06	68.52	99.58	35.19	< 316.95	bzq	-0.1	TXS 1700+685
J1709.7+4319	257.45	43.32	68.41	36.21	< 113.14	bzq	1.01	B3 1708+433
J1719.3+1744	259.83	17.74	39.53	28.07	< 183.16	bzb	1.41	PKS 1717+177
J1722.7+1013	260.68	10.23	32.22	24.3	< 425.7	bzq	2.84	TXS 1720+102
J1725.0+1151	261.27	11.87	34.11	24.47	< 288.43	bzb	1.82	1H 1720+117
J1734.3+3858	263.58	38.98	64.04	31.02	< 95.96	bzq	0.48	B2 1732+38A
J1748.8+7006	267.22	70.11	100.54	30.69	< 275.01	bzb	-1.01	1749+70
J1751.5+0938	267.88	9.64	34.91	17.65	< 183.43	bzb	0.0	OT 81
J1754.3+3212	268.58	32.2	57.75	25.38	< 60.01	bzb	-0.97	RX J1754.1+3212
J1800.5+7829	270.15	78.48	110.06	29.07	< 1134.67	bzb	-0.91	S5 1803+784
J1806.7+6948	271.68	69.8	100.1	29.18	< 497.66	bzb	0.75	3C 371
J1811.3+0339	272.83	3.66	31.62	10.59	< 279.71	bzb	-0.73	NVSS J181118+034114
J1824.0+5650	276	56.84	85.72	26.09	< 65.02	bzb	-1.93	4C 56.27
J1838.7+4759	279.7	47.99	76.9	21.82	< 107.68	bzb	0.63	GB6 J1838+4802
J1849.4+6706	282.35	67.1	97.5	25.03	< 287.58	bzq	0.2	S4 1849+67
J1852.5+4856	283.13	48.94	78.6	19.94	< 41.8	bzq	-2.49	S4 1851+48
J1903.3+5539	285.84	55.67	85.96	20.51	< 77.36	bzb	-1.1	TXS 1902+556
J1927.0+6153	291.77	61.9	93.31	19.71	< 123.93	bzb	-0.79	1RXS J192649.5+615445
J2000.0+6509	300.02	65.16	98.02	17.67	< 208.54	bzb	-0.07	1ES 1959+650
J2116.2+3339	319.05	33.66	79.82	-10.64	< 124.07	bzb	1.32	B2 2114+33
J2121.0+1901	320.26	19.03	69.25	-21.25	< 168.15	bzq	1.26	OX 131
J2133.9+6645	323.49	66.75	105.17	10.96	< 316.94		0.47	
J2143.5+1743	325.88	17.72	72.09	-26.08	< 108.01	bzq	-0.21	OX 169
J2147.3+0930	326.84	9.51	65.85	-32.28	< 162.46	bzq	-0.35	PKS 2144+092
J2202.8+4216	330.71	42.27	92.6	-10.46	< 47.82	bzb	-1.53	BL Lacertae
J2203.4+1726	330.87	17.44	75.68	-29.63	< 164.9	bzq	0.9	PKS 2201+171
J2236.4+2828	339.1	28.48	90.12	-25.66	< 86.69	bzb	0.05	B2 2234+28A

Table 8.2: (cont'd)

Fermi Name 2FGL	RA (deg)	DEC (deg)	l (deg)	b (deg)	Flux/Flux Limit ( $\times 10^{-17} \text{TeV}^{-1}$ $\text{s}^{-1} \text{cm}^{-2}$ )	Source Type	Significance $\sigma$	Associated source
J2243.9+2021	341	20.36	86.59	-33.37	< 84.11	bzb	-0.7	RGB J2243+203
J2244.1+4059	341.03	40.99	98.5	-15.77	< 100.26	bzb	0.69	TXS 2241+406
J2253.9+1609	343.5	16.15	86.12	-38.18	< 135.72	BZQ	0.23	3C 454.3
J2311.0+3425	347.77	34.43	100.42	-24.02	< 62.49	bzq	-0.78	B2 2308+34
J2323.6-0316	350.91	-3.28	77.78	-58.23	< 552.24	bzq	-1.9	PKS 2320-035
J2323.8+4212	350.95	42.2	106.06	-17.78	< 81.89	bzb	0.13	1ES 2321+419
J2325.3+3957	351.33	39.96	105.52	-19.98	< 47.82	bzb	-1.62	B3 2322+396
J2334.8+1431	353.72	14.53	96.56	-44.39	< 167.75	bzb	0.7	BZB J2334+1408
J2339.6-0532	354.91	-5.54	81.36	-62.47	< 2061.09		0.84	

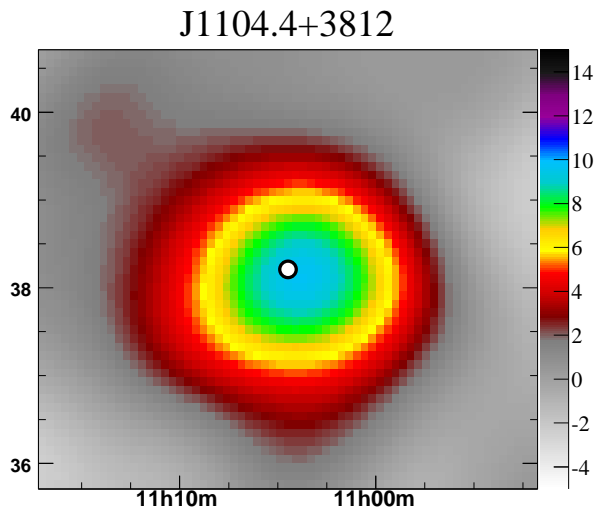


Figure 8.1: This map shows the  $5^\circ \times 5^\circ$  region around Markarian 421. The Fermi-LAT source position is marked by a white dot. This map is made with the spectral optimization  $dN/dE \propto E^{-2.0} e^{-\frac{E}{5 \text{TeV}}}$  and the data have been smoothed by a Gaussian point spread function. The color of a bin shows the statistical significance (in standard deviations) of that bin. The horizontal axis is right ascension in hours and the vertical axis is declination in degrees.

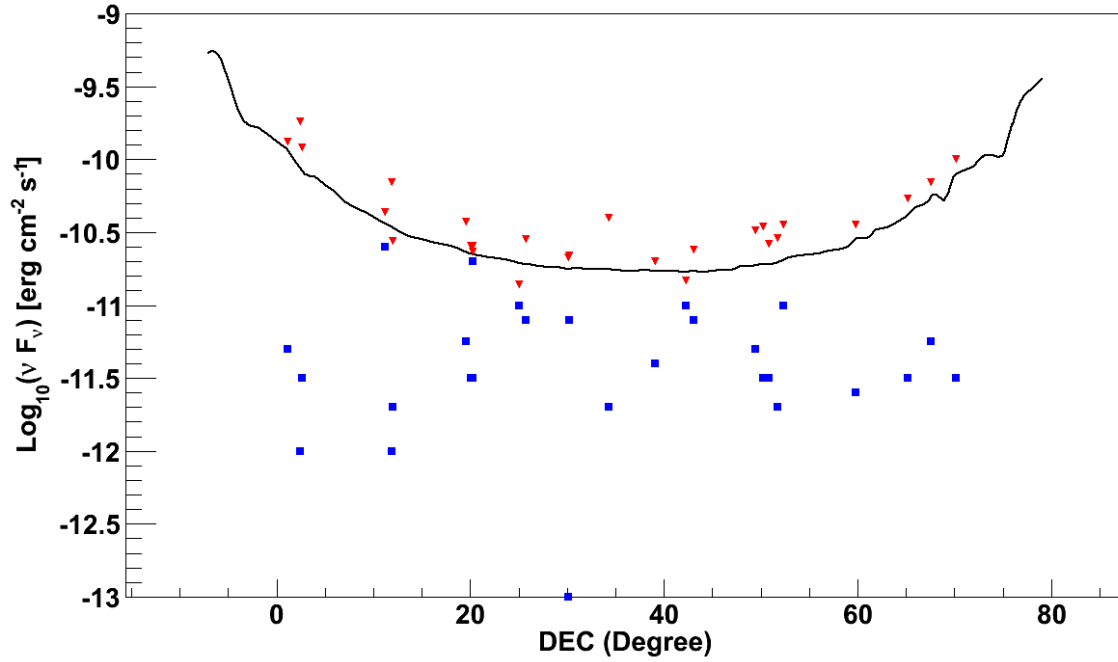


Figure 8.2: The horizontal axis is the declination in the Milagro sky coverage. The vertical axis is the energy flux in  $\text{erg cm}^{-2} \text{s}^{-1}$ . The red triangle data points are Milagro upper limits of BL Lac objects at 7 TeV, the blue square data points are the theoretically predicted flux at 7 TeV and the black solid line is the 95% confidence level expected upper limit of the flux for extragalactic sources corresponding to zero excess derived at 7 TeV for each declination band of the Milagro sky maps made with spectral assumption  $E^{-2.0} \exp -E/5\text{TeV}$ .

# Chapter 9

## The Milagro Targeted Search for GeV Pulsars.

In 2009, the Milagro collaboration performed a targeted search [Abdo et al.(2009a)] of the galactic sources in the Fermi Bright Source List (also known as Fermi-BSL) [Abdo et al.(2009b)], and 14 of these sources were observed by Milagro above  $3\sigma$ . Among these 14 sources, 9 have spatial associations with pulsars. However, in the Fermi-BSL these 9 sources are not confirmed as GeV pulsars, and the GeV pulsed emissions were not isolated from the unpulsed GeV emission. Therefore, these 9 sources can not be used to study the correlation between the pulsar GeV emission and the associated TeV emission. This issue was resolved when the Fermi-LAT collaboration published their second catalog of gamma-ray pulsars [Abdo et al.(2013)] with 117 high-confidence  $\geq 0.1$  GeV gamma-ray pulsar detections, using a three year long data set acquired by the Fermi-LAT. Of these 117 GeV pulsars 32 are located in the Milagro sky coverage.

I performed a targeted search for the Fermi-LAT GeV pulsars in the Milagro sky coverage

using a Milagro sky map made with the spectral assumption of a pure power law with spectral index of -2.6 and no cutoff. The detection threshold for this search was obtained using the False Discovery Rate (FDR) technique, discussed in Section 7.1, with a 1% contamination fraction. In this list of 32 GeV pulsars, 14 passed the FDR cut. Milagro sky maps of a  $5^\circ \times 5^\circ$  region around the Fermi-LAT position of these 14 pulsars are shown in Figure 9.1. The differential photon flux of the sources that were identified with TeV associations were calculated at 35 TeV to minimize the dependency of the derived flux on the spectral assumption (refer to Section 4.4). The 95% confidence upper limit was derived for the Fermi GeV pulsars that did not pass the FDR cut. The results of this search is summarized in Table 9.1, and some other useful parameters of the Fermi-LAT pulsars are summarized in Table 9.2.

The authors of [Abdo et al.(2009a)] mention that the Milagro measured TeV emission associated with pulsars might come from the pulsar and/or from the associated PWN. However, it is very unlikely to get a significant contribution from the pulsar to the TeV flux measured by Milagro. The best example is the Crab pulsar, which is the brightest TeV object measured by Milagro. The VERITAS Collaboration [VERITAS Collaboration et al.(2011)] observed pulsed gamma-rays from the Crab pulsar in the energy range of  $\sim 100$  GeV to  $\sim 200$  GeV. The measured energy spectrum for pulsed gamma-rays is well described by a simple power law, without a cut-off:

$$\frac{dN}{dE} = \left(4.2 \pm 0.6_{stat} \pm 1.4_{syst}\right) \times 10^{-11} \left(\frac{E}{150 \text{ GeV}}\right)^{-3.8 \pm 0.5_{stat} \pm 0.2_{syst}} \text{ TeV}^{-1} \text{ cm}^{-2} \text{ s}^{-1}. \quad (9.1)$$

An extrapolation of this energy spectrum gives a differential photon flux of  $4.2 \times 10^{-20}$  photons  $\text{TeV}^{-1} \text{ cm}^{-2} \text{ s}^{-1}$  at 35 TeV. This is 0.003% of the TeV flux observed by Milagro coincident with the Crab pulsar. In addition, the theoretical model proposed in

[Aharonian et al.(2012)] predicts a sharp cut-off below  $\sim 500$  GeV, so the extrapolated flux at 35 TeV from the pulsar might be even lower. These considerations led me to conclude that the TeV emissions observed coincident with pulsars come predominantly from their associated PWNe.



Pulsar Name PSR	R.A. (deg)	DEC (deg)	Significance ( $\sigma$ 's)	$F_{PWN}$ $\times 10^{-14} \text{ s}^{-1} \text{ cm}^{-2}$
J0007+7303	1.75	73.05	2.66	$2.22 \pm 0.83$
J0106+4855	16.5	48.92	0.09	$< 0.81$
J0205+6449	31.25	64.82	-0.95	$< 0.67$
J0248+6021	42	60.35	1.4	$< 1.55$
J0357+3205	59.25	32.08	-0.23	$< 0.7$
J0534+2200	83.5	22	17.59	$6.45 \pm 0.36$
J0622+3749	95.5	37.82	1.57	$< 1.28$
J0631+1036	97.75	10.6	3.45	$1.67 \pm 0.48$
J0633+0632	98.25	6.53	1.25	$< 2.07$
J0633+1746	98.25	17.77	3.43	$1.38 \pm 0.4$
J0659+1414	104.75	14.23	0.84	$< 1.43$
J1838-0537	279.5	-5.62	1.27	$< 6.56$
J1836+5925	279	59.42	-0.92	$< 0.54$
J1846+0919	281.5	9.32	-1.06	$< 0.64$
J1907+0602	286.75	6.03	6.86	$4.22 \pm 0.61$
J1952+3252	298.5	28.6	4.41	$1.45 \pm 0.32$
J1954+2836	298	32.87	-0.61	$< 0.57$
J1957+5033	299.25	50.55	1.86	$< 1.35$
J1958+2846	299.5	28.77	3.98	$1.31 \pm 0.32$
J2021+3651	305.25	36.85	12.38	$4.18 \pm 0.33$
J2021+4026	305.25	40.43	4.15	$1.37 \pm 0.33$
J2030+4415	307.5	44.25	1.51	$< 1.21$
J2028+3332	307	33.53	-0.29	$< 0.68$
J2030+3641	307.5	36.68	4.43	$1.48 \pm 0.33$
J2032+4127	308	41.45	7.81	$2.53 \pm 0.32$

Table 9.1: Summary of the search with  $\lambda = 0.01$  for TeV emission from the pulsars in the second Fermi-LAT pulsar catalog. The Milagro photon flux derived in the energy band from 34.5 TeV to 35.5 TeV is given for the candidates that passed the  $\lambda = 0.01$  FDR cut and 95% confidence level flux upper limits are given for the rest.

Table 9.1: (cont'd)

Pulsar Name PSR	R.A. (deg)	DEC (deg)	Significance ( $\sigma$ 's)	$F_{PWN}$ $\times 10^{-14} \text{ s}^{-1} \text{ cm}^{-2}$
J2043+2740	310.75	27.67	-0.88	< 0.47
J2055+2539	313.75	25.65	-0.12	< 0.76
J2111+4606	317.75	46.1	1.11	< 1.13
J2139+4716	324.75	47.27	-0.61	< 0.56
J2229+6114	337.25	61.23	6.59	$2.76 \pm 0.41$
J2238+5903	339.5	59.05	4.77	$1.85 \pm 0.38$
J2240+5832	340	58.53	3.22	$1.25 \pm 0.38$

## 9.1 Comparison With IACT Flux Measurements

From this list of GeV pulsars J0534+2200, the Crab pulsar, was found to be the brightest TeV association. It is the brightest TeV PWN in the northern hemisphere and is one of the best measured TeV point sources by gamma-ray observatories. According to TeVCat, the Crab was seen by Whipple, HEGRA, CAT, H.E.S.S., MAGIC, Milagro, Telescope Array, CANGAROO, TACTIC, VERITAS, ARGO-YBJ and FACT observatories. Among these observations the Milagro observatory measured the Crab spectral energy distribution at the highest TeV energies[Abdo et al.(2012)], while H.E.S.S. measured the spectral energy distribution in the second highest energy band. The spectral energy distribution measured by H.E.S.S.[Aharonian et al.(2006a)] between 400 GeV and 40 TeV was found to follow a power law with an exponential cutoff,

$$\frac{dN}{dE} = (3.76 \pm 0.07) \times 10^{-11} \times E^{-2.39 \pm 0.03} \exp(-E/14.3 \pm 2.1) \text{ TeV}^{-1} \text{ s}^{-1} \text{ cm}^{-2}. \quad (9.2)$$

Pulsar Name	$G_{100}$	$\log_{10} \left( \frac{\dot{E}}{1 \text{ erg s}^{-1}} \right)$	$p$	$\dot{p}$	Distance
PSR	$\times 10^{-11}$ ( $\text{erg cm}^{-2} \text{s}^{-1}$ )		(ms)	$\times 10^{-15}$	kpc
J0007+7303	$40.1 \pm 0.4$	35.6	315.9	357	$1.4 \pm 0.3$
J0106+4855	$1.9 \pm 0.2$	34.4	83.2	0.43	$3^{+1.1}_{-0.7}$
J0205+6449	$5.4 \pm 0.2$	37.4	65.7	190	$1.95 \pm 0.04$
J0248+6021	$5.2 \pm 0.4$	35.3	217.1	55	$2 \pm 0.2$
J0357+3205	$6.4 \pm 0.2$	33.7	444.1	13.1	$< 8.2$
J0534+2200	$129.3 \pm 0.8$	38.6	33.6	420	$2 \pm 0.5$
J0622+3749	$1.4 \pm 0.1$	34.4	333.2	25.4	$< 8.3$
J0631+1036	$4.7 \pm 0.3$	35.2	287.8	104	$1 \pm 0.2$
J0633+0632	$9.4 \pm 0.5$	35	297.4	79.6	$< 0.87$
J0633+1746	$423.3 \pm 1.2$	34.5	237.1	11	$0.2^{+0.2}_{-0.1}$
J0659+1414	$2.5 \pm 0.2$	34.5	384.9	55	$0.28 \pm 0.03$
J1838-0537	$18.8 \pm 0.9$	36.7	145.7	465	$< 24.1$
J1836+5925	$60.6 \pm 0.4$	34	173.3	1.5	$0.5 \pm 0.3$
J1846+0919	$2.4 \pm 0.2$	34.5	225.6	9.9	$< 22$
J1907+0602	$25.4 \pm 0.6$	36.4	106.6	86.7	$3.2 \pm 0.3$
J1952+3252	$10.3 \pm 0.4$	36	39.5	5.8	$< 18.6$
J1954+2836	$13.8 \pm 0.3$	36.5	92.7	21.2	$2 \pm 0.5$
J1957+5033	$2.6 \pm 0.1$	33.6	374.8	6.8	$< 14.5$
J1958+2846	$9.1 \pm 0.4$	35.5	290.4	212	$< 18.5$
J2021+3651	$49.4 \pm 0.8$	36.5	103.7	95.6	$10^{+2}_{-4}$
J2021+4026	$95.5 \pm 0.9$	35	265.3	54.2	$1.5 \pm 0.4$
J2030+4415	$5.8 \pm 0.4$	34.3	227.1	6.5	$< 15.7$
J2028+3332	$5.8 \pm 0.4$	34.5	176.7	4.9	$< 17.2$
J2030+3641	$3.1 \pm 0.3$	34.5	200.1	6.5	$3 \pm 1$
J2032+4127	$10.6 \pm 0.6$	35.4	143.2	20.4	$3.7 \pm 0.6$

Table 9.2: Properties of the Fermi-LAT pulsars in the Milagro sky coverage. Column 2 ( $G_{100}$ ) is the the phase-averaged integral energy flux in the 0.1 to 100 GeV energy band. Column 3 is the  $\text{Log}_{10}$  of the pulsars spin-down luminosity. Column 4 is the pulse period. Column 5 is the first time derivative of the pulse period. Column 6 is the distance to pulsar. All of these values are taken from the Fermi-LAT second pulsar catalog.

Table 9.2: (cont'd)

Pulsar Name PSR	$G_{100}$ $\times 10^{-11}$ ( $\text{erg cm}^{-2}\text{s}^{-1}$ )	$\log_{10} \left( \frac{\dot{E}}{1 \text{ erg s}^{-1}} \right)$	$p$ (ms)	$\dot{p}$ $\times 10^{-15}$	Distance kpc
J2043+2740	$1 \pm 0.1$	34.7	96.1	1.2	$1.8 \pm 0.3$
J2055+2539	$5.4 \pm 0.2$	33.6	319.6	4.1	$< 15.3$
J2111+4606	$4.4 \pm 0.3$	36.1	157.8	143	$< 14.8$
J2139+4716	$2.3 \pm 0.2$	33.4	282.8	1.8	$< 14.1$
J2229+6114	$25.3 \pm 0.4$	37.3	51.6	77.9	$0.8^{+0.15}_{-0.2}$
J2238+5903	$6.4 \pm 0.3$	35.9	162.7	97	$< 12.4$
J2240+5832	$1.1 \pm 0.3$	35.3	139.9	15.2	$7.7 \pm 0.7$

Using this energy spectrum the flux derived in the energy band from 34.5 TeV to 35.5 TeV is  $2.4^{+6}_{-2} \times 10^{-14} \text{ TeV}^{-1} \text{ s}^{-1} \text{ cm}^{-2}$ . Within error bars the H.E.S.S. measurement is consistent with the TeV flux measured by Milagro of:  $5.4 \pm 0.3 \times 10^{-14} \text{ TeV}^{-1} \text{ s}^{-1} \text{ cm}^{-2}$ .

Among the other candidates that passed our standard FDR cut, IACTs have measured the TeV flux coincident with three of these sources: J0007+7303, J2032+4127 and J2229+6114. The names given to their spatially associated IACT TeV sources are CTA1, TeV J2032+4130 and Boomerang, respectively. The most precise spectral distributions of CTA1 and Boomerang were measured by VERITAS [Aliu et al.(2013), Acciari et al.(2009)] and for TeV J2032+4130 the best fit spectral distribution is measured by H.E.S.S. [Aharonian et al.(2005)]. Among the candidates that failed our standard FDR cut, IACTs have measured the TeV flux coincident with two sources: J0633+0632 and J1838-0537. The names given to their spatially associated IACT TeV sources are HESS J0632+057 and HESS J1837-069. The parameters of the best fit spectral distributions of these two sources are measured by H.E.S.S. [Aharonian et al.(2007), Aharonian et al.(2006c)]. The integral photon flux de-

rived in the energy band from 34.5 TeV to 35.5 TeV of these five PWNe using the spectral parameters measured by IACTs are summarized in column 2 of Table 9.3, and the integral photon flux in the same energy band measured by Milagro is summarized in column 3. As shown in this table the Milagro flux measurements and the IACT flux measurements of the candidates that passed the FDR cut are consistent within their error bars. For the two candidates that failed the FDR cut the Milagro upper limits are above the IACT flux measurements. Therefore, I can conclude that the Milagro measurements are in agreement with the IACT measurements.

Fermi Name	TeVCat Name	IACT Flux $\times 10^{-14} \text{TeV s}^{-1} \text{cm}^{-2}$ <i>a</i>	Milagro Flux $\times 10^{-14} \text{TeV s}^{-1} \text{cm}^{-2}$
J0007+7303	CTA1	$1.4^{+5}_{-1.1}$ <i>b</i>	$2.2 \pm 0.83$
J2032+4127	TeV J2032+4130	$3.5^{+2.7}_{-1.6}$ <i>a</i>	$2.1 \pm 0.3$
J2229+6114	Boomerang	$1.3^{+15}_{-1.2}$ <i>a</i>	$2.76 \pm 0.41$
J0633+0632	HESS J0632+057	$0.4^{+0.7}_{-0.3}$ <i>b</i>	$< 2.07$
J1838-0537	HESS J1837-069	$5.4^{+1.6}_{-1.2}$ <i>b</i>	$< 24.1$

Table 9.3: The energy flux derived in the energy band from 34.5 TeV to 35.5 TeV is summarized. The first column is the name given in the Fermi-LAT second pulsar catalog. The second column is the name given in the TeVCat catalog. The third column is the flux measured by IACTs. The fourth column is the flux measured by Milagro. (a) Flux measurements were derived from VERITAS measurements. (b) Flux measurements were derived from H.E.S.S. measurements.

## 9.2 Population Study of Associated TeV emissions

In this section, I discuss the correlations between pulsar properties and the TeV flux of the associated PWN. Table 9.2 lists the phase-averaged integral energy flux in the 0.1 to 100 GeV energy band ( $G_{100}$ ),  $\text{Log}_{10}$  of the pulsar's spin-down luminosity  $\dot{E}$ , pulse period (P), the first time derivative of the pulse period ( $\dot{P}$ ) and the distance (d) to each pulsar. The luminosity of a PWN ( $L_{PWN \text{ TeV}}$ ) is related to its flux  $F_{PWN}$  by:

$$L_{PWN \text{ TeV}} = 4\pi d^2 F_{PWN}. \quad (9.3)$$

However, the luminosity of pulsars ( $L_{PSR \text{ GeV}}$ ) depends on the beaming factor ( $f_{\Omega}$ ) (refer to Section 2.2) in addition to the flux and distance:

$$L_{PSR \text{ GeV}} = 4\pi d^2 f_{\Omega} G_{100}. \quad (9.4)$$

It is not possible to derive the  $f_{\Omega}$  that corresponds to each pulsar using the pulsar's properties measured by Fermi-LAT. Therefore, it is not possible to calculate the pulsar luminosity in the 0.1 to 100 GeV energy band. However, the Pulsar GeV luminosity normalized with respect to the beaming factor can be calculated by:

$$L_{PSR \text{ GeV}}/f_{\Omega} = 4\pi d^2 G_{100}. \quad (9.5)$$

First, I examined the correlation between Pulsar GeV luminosity normalized with respect to the beaming factor ( $L_{PSR \text{ GeV}}/f_{\Omega}$ ) and TeV luminosity of the associated PWNe ( $L_{PWN \text{ TeV}}$ ). Figure 9.2 shows the correlation between  $L_{PSR \text{ GeV}}/f_{\Omega}$  and  $L_{PWN \text{ TeV}}$ . The blue

squares are the luminosity of the PWNe that passed the  $\lambda = 0.01$  FDR cut and the red triangles are the upper limit of the luminosity of the other sources. The large error bars on this plot are due to the distance uncertainties. The candidates that passed the  $\lambda = 0.01$  FDR cut yielded a linear correlation coefficient of 0.73. Furthermore, the best fit of the candidates that passed the  $\lambda = 0.01$  FDR cut, assuming a linear function, yielded

$$\text{Log}_{10}(L_{PWN} \text{ TeV}) = (0.79 \pm 0.05) \times \text{Log}_{10}(L_{PSR} \text{ GeV}) + 3.5 \pm 1.8, \quad (9.6)$$

with  $\chi^2/NDF = 129.531/9$ . The best fit of the same candidates, assuming a constant (slope of the best fit line is zero), yielded:

$$\text{Log}_{10}(L_{PWN} \text{ TeV}) = 31.3 \pm 0.03, \quad (9.7)$$

with  $\chi^2/NDF = 326.25/10$ . This means that the improvement of the best fit to a linear function is equivalent to  $13.9\sigma$ . The linear correlation coefficient and the comparison between the two fits demands a common underlying cause for the two emission mechanisms.

Next, in Figure 9.3 and Figure 9.4, I examined the correlation between the observed flux on earth in the 34.5 to 35.5 TeV energy band ( $F_{PWN}$ ) and the  $\dot{E}/d^2$  of each PWNe. Motivations to choose the parameter  $\dot{E}/d^2$  are:  $\dot{E}$  is a good estimator for the rate of the energy that is deposited in the PWN by the associated pulsar, making a PWN associated with a high  $\dot{E}$  pulsar have more energetic leptons to create TeV photons, and  $\dot{E}$  was divided by  $d^2$  to consider the effect that the flux density decreases quadratically with the distance to a source. The authors of [Carrigan et al.(2008)] argue that the probability of detecting very high energy gamma-rays from a PWN should vary with  $\dot{E}/d^2$ , and they showed that for the

radio loud pulsars the fraction of PWNe detected with H.E.S.S. is about 70% for pulsars with  $\dot{E}/d^2 > 10^{35} \text{ ergs}^{-1}\text{kpc}^{-2}$  while for pulsars with  $\dot{E}/d^2 < 10^{33} \text{ ergs}^{-1}\text{kpc}^{-2}$  it is 5%. Before my thesis work started, the Milagro collaboration also investigated the association between the detected PWNe and the  $\dot{E}/d^2$  of the associated GeV pulsars [Abdo et al.(2009a)]. They noted that “the four high-confidence Milagro detections associated with pulsars of known periodicity and distance” have  $\dot{E}/d^2 > 10^{35}$ .

In Figure 9.3 I examined the distribution between  $\dot{E}/d^2$  and  $F_{PWN}$  for the GeV pulsars. The fraction of the PWNe that passed the  $\lambda = 0.01$  FDR cut in one-decade bins of the  $\dot{E}/d^2$  is shown in Figure 9.4. The slope of the best fit line for these data points is  $0.02 \pm 0.1$ , which is consistent with zero. Therefore, these results do not demonstrate a connection between the probability of detecting TeV gamma-rays from a PWN and the  $\dot{E}/d^2$  of the associated GeV pulsar, as H.E.S.S. observed for radio loud pulsars. (Note that H.E.S.S. studies radio loud pulsars and I studied GeV loud pulsars. So their are different selection effects between the two samples.).

Next, I examined the distribution of the PWNe luminosity in the 34.5 to 35.5 TeV energy band ( $L_{PWN \text{ TeV}}$ ) as a function of the spin-down luminosity ( $\dot{E}$ ) and characteristic age ( $\tau_c$ ) of the associated pulsars. In 2009, Mattana et al. investigated the  $L_{PWN \text{ TeV}}$  vs.  $\dot{E}$  correlation, and the  $L_{PWN \text{ TeV}}$  vs.  $\tau_c$  correlation using the PWNe observed by the H.E.S.S. observatory, and they discussed the theoretical expectations of these two distributions in the leptonic scenario [Mattana et al.(2009)], where the PWNe are energized by the relativistic electrons injected into the PWNe by the associated pulsars. In Chapter 2 I summarized their argument, which leads one to theoretically expect that the PWN luminosity in TeV energies should not be a function of the  $\dot{E}$  or  $\tau_c$  of the associated pulsar,  $L_{PWN \text{ TeV}} \propto \dot{E}^0$  and  $L_{PWN \text{ TeV}} \propto \tau_c^0$ .



In Figure 9.5(a) and Figure 9.5(b), I examined the distribution of PWNe luminosity in the 34.5 to 35.5 TeV energy band ( $L_{PWN\ TeV}$ ) vs. the spin-down luminosity of the associated pulsars, and the  $L_{PWN\ TeV}$  vs. the characteristic age ( $\tau_c$ ) of the associated pulsars. The linear correlation coefficient between the  $Log_{10}(\dot{E})$  and  $Log_{10}(L_{PWN\ TeV})$ , calculated only using the candidates that passed the  $\lambda = 0.01$  FDR cut was, 0.3. Furthermore, the best fit of the candidates that passed the  $\lambda = 0.01$  FDR cut, assuming a linear function, yielded

$$Log_{10}(L_{PWN\ TeV}) = (0.06 \pm 0.03) \times Log_{10}(\dot{E}) + 29 \pm 1, \quad (9.8)$$

with  $\chi^2/NDF = 327/9$ . The best fit of the same candidates assuming a constant (slope of the best fit is zero) yielded

$$Log_{10}(L_{PWN\ TeV}) = 31.3 \pm 0.03, \quad (9.9)$$

with  $\chi^2/NDF = 326.25/10$ . This means the linear assumption is consistent with zero with a  $2\sigma$  error bar and the improvement of the best fit to a linear function is only a  $1.1\sigma$  equivalent. Therefore, the  $L_{PWN\ TeV}$  vs.  $\dot{E}$  distribution derived from Milagro observations is not consistent with the theoretical expectations of [Mattana et al.(2009)] within  $1\sigma$  error bar, but they become consistent with  $2\sigma$  error bars. Note that these error bars are estimated only using the statistical errors. Therefore, these error bars become larger with inclusion of the systematic errors. I re-examined this correlation in Chapter 10, adding 7 data points measured by VERITAS and H.E.S.S. With those new data points the slope of the best fit for the  $L_{PWN\ TeV}$  vs.  $\dot{E}$  distribution became consistent with zero, within  $1\sigma$  error bar.

The linear correlation coefficient between  $Log_{10}(L_{PWN\ TeV})$  and  $Log_{10}(\tau_c)$ , calcu-

lated using only the candidates that passed the  $\lambda = 0.01$  FDR cut was -0.28. Furthermore, the best fit of the candidates that passed the  $\lambda = 0.01$  FDR cut, assuming a linear function, yielded

$$\text{Log}_{10} (L_{PWN \text{ TeV}}) = (-0.036 \pm 0.056) \times \text{Log}_{10} (\dot{E}) + 31.42 \pm 0.09, \quad (9.10)$$

with  $\chi^2/NDF = 327/9$ . The slope of the best fit with a linear assumption is consistent with zero. Therefore, I can conclude that the  $L_{PWN \text{ TeV}}$  vs.  $\tau_c$  distribution derived from Milagro data set is consistent with the theoretical expectation derived by [Mattana et al.(2009)].

Lastly, I examined the TeV efficiency of the PWNe at 35 TeV ( $\varepsilon_\gamma$ ) as a function of  $\dot{E}$  and  $\tau_c$ . The efficiency is defined as:

$$\varepsilon_\gamma = \frac{L_{PWN \text{ TeV}}}{\dot{E}}, \quad (9.11)$$

where  $\varepsilon_\gamma$  is the fraction of the spin-down luminosity that becomes the TeV flux in the 34.5 to 35.5 TeV energy band. The distributions of  $\text{Log}_{10} (\varepsilon_\gamma)$  vs.  $\text{Log}_{10} (\dot{E})$  and  $\text{Log}_{10} (\varepsilon_\gamma)$  vs.  $\text{Log}_{10} (\tau_c)$  are shown in Figure 9.6(a) and Figure 9.6(b), respectively. The linear correlation coefficient between  $\text{Log}_{10} (\dot{E})$  and  $\text{Log}_{10} (\varepsilon_\gamma)$ , calculated using only the candidates that passed the  $\lambda = 0.01$  FDR cut was -0.6. However, this correlation was mostly driven by the two pulsars with  $\dot{E} > 10^{37} \text{ erg s}^{-1}$ . The linear correlation coefficient of this distribution excluding those pulsars is 0.08. Therefore, these results were not favorable to concluding that there is a dependency between  $\varepsilon_\gamma$  and the  $\dot{E}$  of the associated pulsars. However, the  $\varepsilon_\gamma$  of the two PWNe that have associated pulsars with  $\dot{E} > 10^{37} \text{ erg s}^{-1}$  are more than an order of magnitude less than the  $\varepsilon_\gamma$  of those associated with low  $\dot{E}$  pulsars. The distribution

of  $\text{Log}_{10}(\tau_c)$  vs.  $\text{Log}_{10}(\varepsilon_\gamma)$  also had similar features. The linear correlation coefficient between  $\text{Log}_{10}(\tau_c)$  and  $\text{Log}_{10}(\varepsilon_\gamma)$ , calculated using only the candidates that passed the  $\lambda = 0.01$  FDR cut was 0.6. However, this correlation was mostly driven by the two pulsars that have  $\tau_c < 10^{1.1}$  kyr. The linear correlation coefficient of this distribution excluding those pulsars become 0.08. Therefore, these results were not favorable to conclude that there is a dependency between  $\varepsilon_\gamma$  and  $\tau_c$  of the associated pulsars.

### 9.3 Discussion

The most widely discussed gamma-ray emission mechanisms are either hadronic or leptonic. In the hadronic scenario, gamma-rays are produced by secondary  $\pi^0$  decays, which are produced by the collisions between the highly energetic hadrons and nuclei in the ambient medium [Gabici et al.(2009)]. In the leptonic scenario, gamma-rays are produced by relativistic electrons and positrons. Most of the pulsar gamma-ray emission models predict that the GeV photons in the 0.1 to 100 GeV energy range should be dominated by curvature radiation of the relativistic leptons emitted by the rotating neutron star [Muslimov & Harding(2004)]. Most of the PWN TeV gamma-ray emission models predict that TeV photons are produced from inverse Compton(IC) up-scattering of ambient photon fields, such as cosmic microwave background, stellar radiation, infrared emission from dust, or synchrotron radiation by the ultra-relativistic electrons/positrons [de Jager & Djannati-Ataï(2009), de Jager et al.(2009)]. This suggests that in the leptonic scenario both the pulsar GeV luminosity in the 0.1 to 100 GeV energy range ( $L_{PSR\ GeV}$ ) and the PWN TeV luminosity ( $L_{PWN\ TeV}$ ) are tightly related to the properties of the electron-positron wind coming from the rotating neutron star. Therefore, the studies of correlations between  $L_{PWN\ TeV}$  and pulsar properties (such as

$\dot{E}$ ,  $\tau_c$  and  $L_{PSR} \text{ GeV}$ ) are important to constrain the leptonic scenario.

The correlation between  $L_{PSR} \text{ GeV}$  and  $L_{PWN} \text{ TeV}$  shown in Figure 9.2 leads one to suspect a common underlying cause for the two emission mechanisms. In the leptonic scenario, one property relevant to both emissions is the electron-positron current emitted by the rotating neutron star,  $\dot{N}_e$ . The GeV energy flux from pulsars is thought to be directly related to the instantaneous value of  $\dot{N}_e$ , because the GeV pulsed emission from the magnetosphere is often thought to be produced from curvature emission by the most recently produced electron-positron population from the rotating neutron star.

Inside PWNe, TeV photons are often thought to be produced by IC. Therefore,  $L_{PWN} \text{ TeV}$  should depend both on the relativistic electron-positron population and the ambient photon population in the PWN. By considering the cooling time [Mattana et al.(2009)] suggested that the electron-positron population that produces TeV photons by IC becomes proportional to the integral of  $\dot{N}_e$  over the pulsar lifetime, instead of being proportional to the instantaneous value of  $\dot{N}_e$ . Hence, [Mattana et al.(2009)] argued that  $L_{PWN} \text{ TeV}$  should be proportional to the integral of  $\dot{N}_e$  over the pulsar lifetime. However, [Mattana et al.(2009)] did not account for the ambient photon field density ( $\rho_{ph}$ ) when deriving  $L_{PWN} \text{ TeV}$ . I suggest that the proportionality between  $L_{PWN} \text{ TeV}$  and  $L_{PSR} \text{ GeV}$  might occur due to a proportionality between the ambient photon field density ( $\rho_{ph}$ ) and  $\dot{N}_e$ .

There are two different ambient photon fields which could be relevant to the production of TeV gamma-rays and directly related to  $\dot{N}_e$ : photons from synchrotron radiation and far-infrared photons [Atoyan & Aharonian(1996)]. The density of synchrotron radiation photons in the x-ray energy band is roughly proportional to the density of the freshly injected pulsar wind [Mattana et al.(2009)]. In addition, far-infrared seed photons can be made by heating the pulsar wind, as described in Section 2.2 of [Arons(1996)]. Therefore  $\rho_{ph}$  may be roughly

proportional to  $\dot{N}_e$ , instead of the integral of  $\dot{N}_e$ . While these considerations are suggestive, a more detailed theoretical study is clearly needed to fully understand this correlation, which is beyond the scope of the work presented in this dissertation.

Using Figure 9.3 and Figure 9.4, I investigated the detectability of a TeV PWN as a function of  $\dot{E}$ . The lack of correlation between the detectability and  $\dot{E}/d^2$  suggests that the rate of energy that a pulsar feeds to the associated PWN is not the only parameter relevant for the PWN TeV flux. The PWN TeV flux could also result from some other mechanisms that are correlated with the pulsar or PWN, such as the age of the pulsar and adiabatic cooling. For example, if the age of a pulsar is shorter than the cooling time of electrons that produce TeV photons, then the relic electrons from earlier epochs might also contribute to the PWN TeV emission.

Using Figure 9.6(a) and Figure 9.6(b), I investigated the efficiency ( $\varepsilon_\gamma$ ) of PWN TeV emission at 35 TeV as a function of  $\dot{E}$  and  $\tau_c$ . Neither, the  $\varepsilon_\gamma$  vs.  $\dot{E}$  nor the  $\varepsilon_\gamma$  vs.  $\tau_c$  distribution demonstrate strong evidence for correlations. However, the two PWNe associated with the youngest and highest  $\dot{E}$  pulsars have an  $\varepsilon_\gamma$  more than an order of magnitude less than the other PWNe. These results are consistent with the IC model discussed by Mattana et al (2009). When a PWN gets older it accumulates relativistic electrons that produce TeV photons, and the current injection rate of electrons becomes negligible. Therefore, relatively older PWNe might have a larger population of relativistic electrons to produce TeV photons. However, the population of the relativistic electrons in a PWN cannot continue to increase forever, because of cooling effects and that the magnetic field strength decays with time. Mayer et al.(2012) have shown that the IC peak is expected to have a negative correlation with the pulsar's characteristic age, because the strong magnetic field strength decays with time, and the cooling effects. My data set was not able to constrain the Mayer et al.(2012)'s

argument, because of the lack of older pulsars.

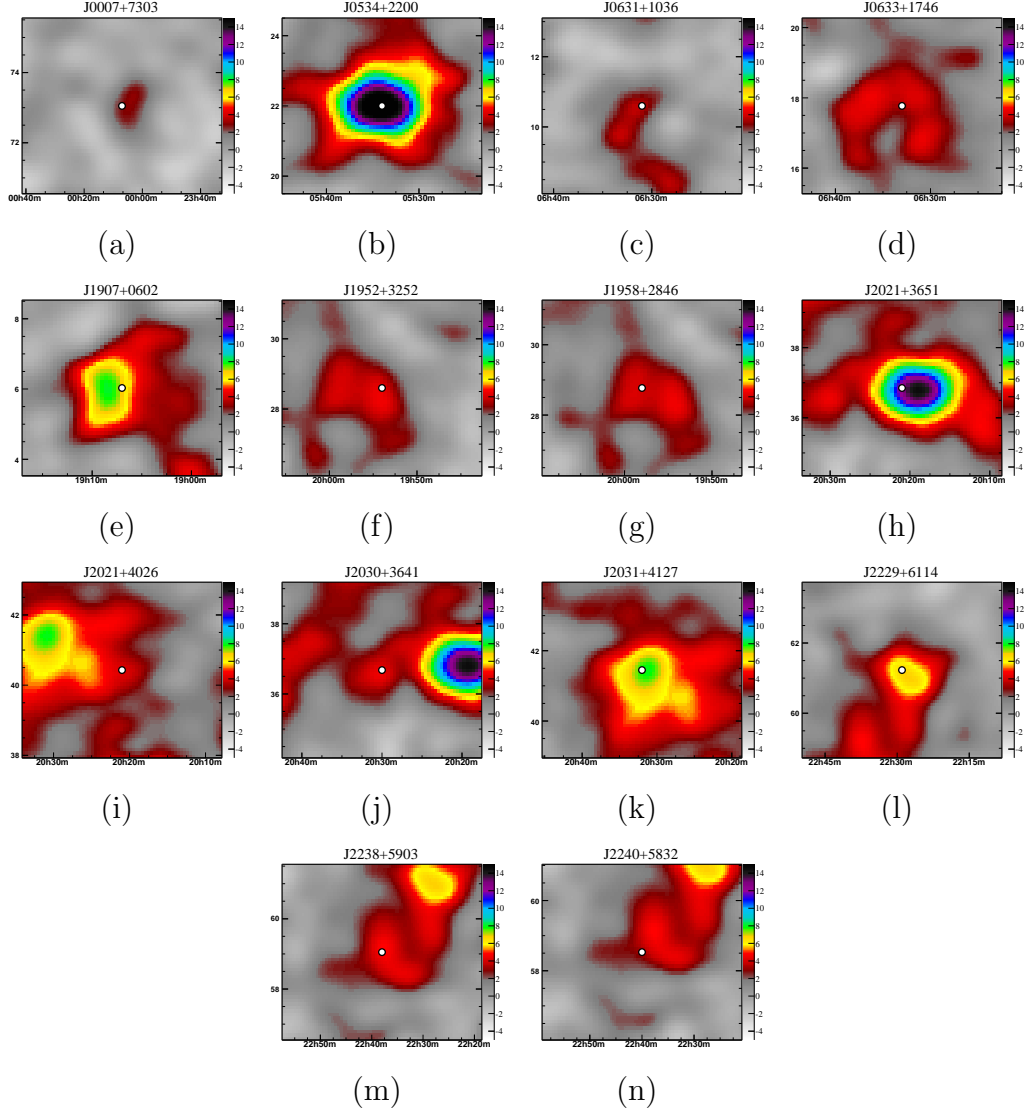


Figure 9.1: These maps show the  $5^\circ \times 5^\circ$  region around the pulsars that passed the  $\lambda = 0.01$  FDR cut. The LAT source positions are marked by white dots. These maps are made with the spectral optimization  $dN/dE \propto E^{-2.6}$  and the data have been smoothed by a Gaussian point spread function. The color of a bin shows the statistical significance (in standard deviations) of that bin. The horizontal axis is right ascension in hours and the vertical axis is declination in degrees.

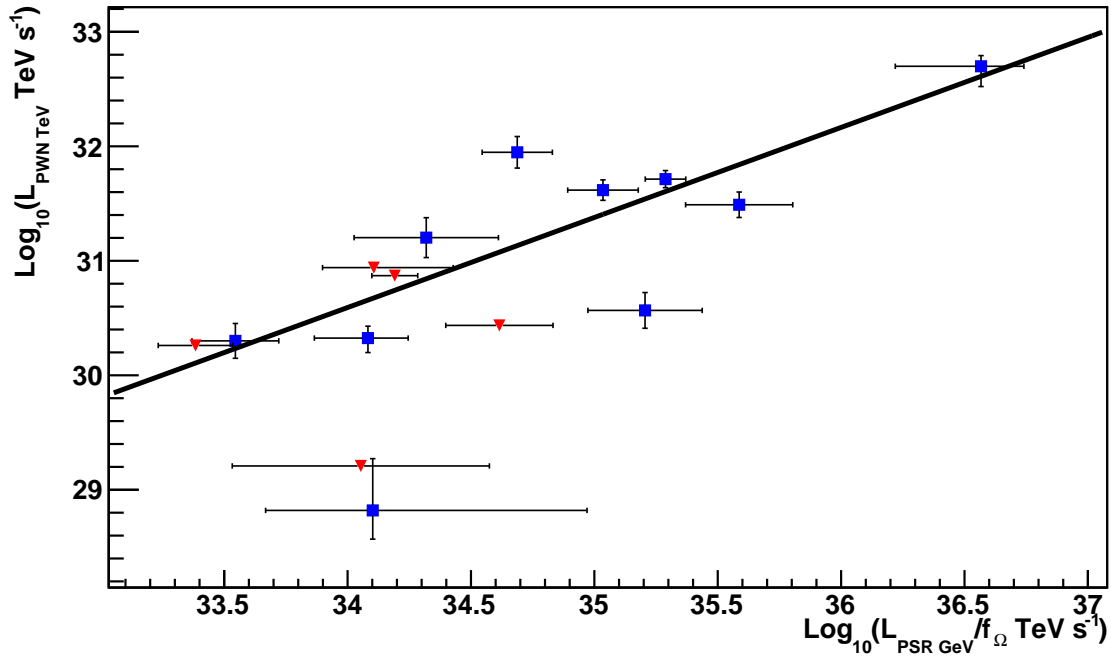


Figure 9.2: PWN TeV luminosity vs. Pulsar GeV luminosity normalized with respect to the beaming factor ( $f_{\Omega}$ ). Blue squares are the luminosity derived in the energy band from 34.5 TeV to 35.5 TeV of the candidates that passed the  $\lambda = 0.01$  FDR cut. Red triangles are the upper limit of the luminosity derived in the energy band from 34.5 TeV to 35.5 TeV of the candidates that failed the  $\lambda = 0.01$  FDR cut. The linear correlation coefficient calculated only using the candidates that passed the  $\lambda = 0.01$  FDR cut is 0.73, and the best fit line for these data points have a slope of  $0.79 \pm 0.05$  and intercept of  $3.5 \pm 1.8$  and  $\chi^2/NDF = 129.531/9$ .



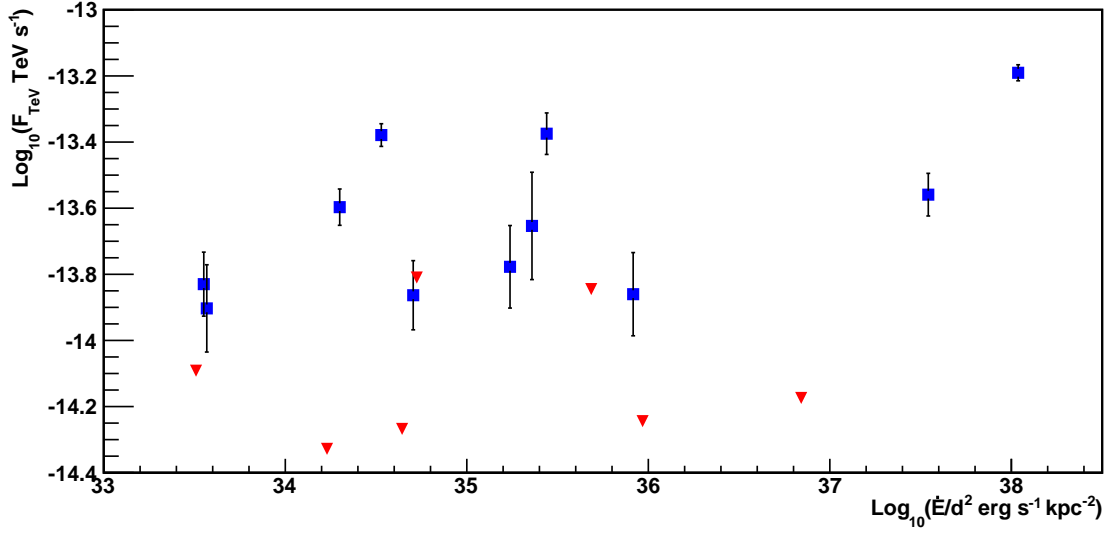


Figure 9.3: The PWN gamma-ray flux in the 34.5 to 35.5 TeV energy band is shown ( $F_{TeV}$ ). The blue squares are the flux of the candidates that passed the  $\lambda = 0.01$  FDR cut. The red triangles are the upper limits of the candidates that failed the  $\lambda = 0.01$  FDR cut.

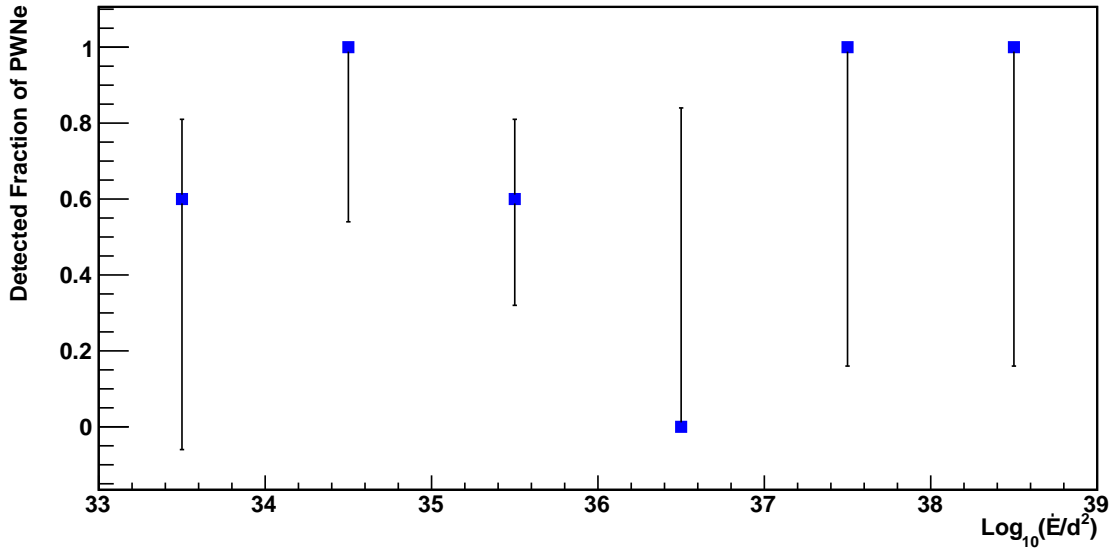


Figure 9.4: Fraction of the PWNe that passed the  $\lambda = 0.01$  FDR cut in one-decade bins of the  $\dot{E}/d^2$ .

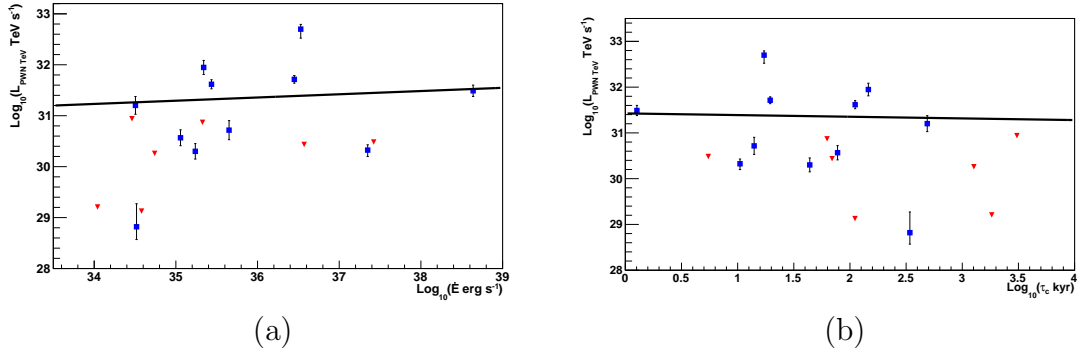


Figure 9.5: Distributions of PWNe luminosity in the 34.5 to 35.5 TeV energy band  $L_{PWN} \text{ TeV}$  vs. the spin-down luminosity  $\dot{E}$  of the associated pulsars (a), and  $L_{PWN} \text{ TeV}$  vs. the characteristic age ( $\tau_c$ ) of the associated pulsars (b) are shown. Blue squares are the  $L_{PWN} \text{ TeV}$  of the candidates that passed the  $\lambda = 0.01$  FDR cut. Red triangles are the upper limit of the  $L_{PWN} \text{ TeV}$  of the candidates that failed the FDR cut.

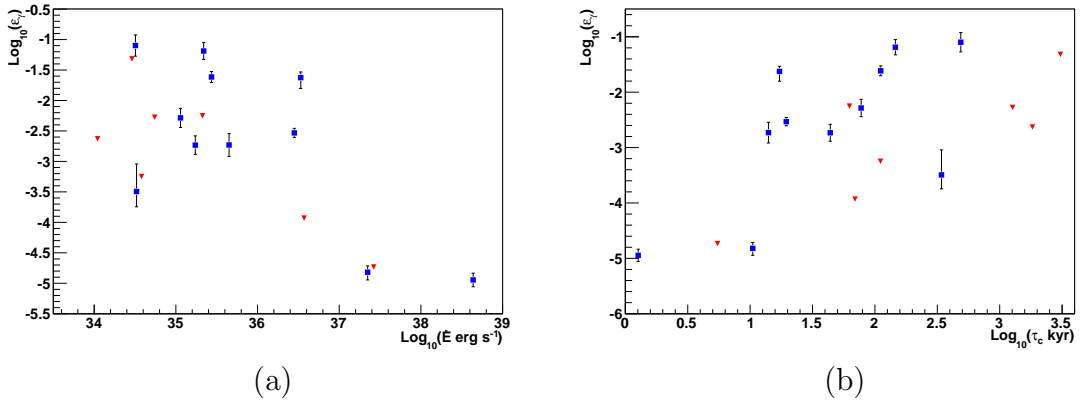


Figure 9.6: TeV efficiency of PWNe,  $\varepsilon_\gamma$ , vs.  $\dot{E}$  (a), and  $\varepsilon_\gamma$  vs.  $\tau_c$  (b) distributions are shown.  $\varepsilon_\gamma$  is defined as shown in Equation 10.16. Blue squares are the  $\varepsilon_\gamma$  of the candidates that passed the  $\lambda = 0.01$  FDR cut. Red triangles are the  $\varepsilon_\gamma$  upper limit of the candidates that failed the FDR cut.

# Chapter 10

## Experimental Constraints on Gamma-Ray Pulsar Gap Models

In this chapter I present a new method to isolate the flux correlation factor ( $f_{\Omega}$ ) of GeV pulsars as a function of the pulsar spin down luminosity ( $\dot{E}$ ). I applied this method to a sample of PWNe measured in TeV energies, and obtained the  $f_{\Omega}$  vs.  $\dot{E}$  distribution of the pulsars. I then compared my measured  $f_{\Omega}$  vs.  $\dot{E}$  distribution with the theoretically expected  $f_{\Omega}$  vs.  $\dot{E}$  distributions of 4 pulsar gap models.

Currently, there are several pulsar gap models being discussed in the pulsar community. These models can be constrained either by studying individual pulsars in detail or alternatively using the collective properties of a sample of pulsars. The large sample of pulsars discovered by the Fermi Large Area Telescope (Fermi-LAT) provides a good place to study the collective properties of GeV pulsars.

The GeV luminosity as a function of other pulsar parameters is a fundamental quantity which the models must predict. However, the potential utility of this measurement is limited

by two factors: inability to measure  $f_\Omega$  and imprecise distance measurements. The factor  $f_\Omega$  provides the correction to extrapolate the observed phase-averaged flux from the earth line-of-sight to the full sky flux for a given beam shape. It is an essential factor needed to convert observed fluxes to luminosity measurements:

$$L_{PSR\ GeV} = 4\pi d^2 f_\Omega F, \quad (10.1)$$

where  $L_{PSR\ GeV}$  is the luminosity,  $d$  is the distance to the pulsar from earth and  $F$  is the phase averaged flux measured at earth. Since  $f_\Omega$  is a model dependent parameter, luminosity calculations are also model dependent. Therefore, one option to constrain GeV pulsar emission models is to use the collective properties of the luminosity distribution, but the uncertainty of distance measurements degrades the accuracy of the luminosity distribution. This issue can be resolved by studying the ratio of the flux from pulsars ( $G_{100}$ ) to that of their associated PWNe ( $F_{PWN}$ ), which is a distance independent parameter. In the next section I present a new technique to obtain  $f_\Omega$  as a function of  $\dot{E}$ , using this distance independent parameter:  $G_{100}/F_{PWN}$ .

## 10.1 A New Method to Isolate $f_\Omega$

The ratio of a pulsar's GeV flux ( $G_{100}$ ) to PWN flux ( $F_{PWN}$ ) can be turned into a luminosity ratio by multiplying both the numerator and denominator by  $4\pi d^2$ , yielding:

$$\frac{G_{100}}{F_{PWN}} = \frac{4\pi d^2 G_{100}}{4\pi d^2 F_{PWN}} \quad (10.2)$$

The PWN luminosity ( $L_{PWN}$ ) is related to flux by:

$$L_{PWN} = 4\pi d^2 F_{PWN}. \quad (10.3)$$

However, pulsar's GeV luminosity ( $L_{PSR GeV}$ ) is also dependent on the flux correlation factor ( $f_\Omega$ ):

$$L_{PSR GeV} = 4\pi d^2 f_\Omega G_{100}. \quad (10.4)$$

Substituting Equation 10.3 and 10.4 into Equation 10.2 gives:

$$\frac{G_{100}}{F_{PWN}} = \frac{L_{PSR GeV}/f_\Omega}{L_{PWN}}. \quad (10.5)$$

This result can be combined with the theoretical correlation between  $L_{PSR GeV}$  and  $\dot{E}$ . Most of the models expect  $L_{PSR GeV} \propto \dot{E}^{\frac{1}{2}}$  above some threshold of open field-line voltage (eg. [Arons(1996)], [Abdo et al.(2013)] , [Arons, J. 2006], [Harding(1981)], [Harding & Muslimov(2002)], [Pierbattista et al.(2012)], [Muslimov & Harding(2003)], [Harding & Muslimov(2003)], [Romani & Watters(2010)], [Takata et al.(2010)], [Thompson, D.J. (2000)] , and [Thompson(2001)]). Using this relation Equation 10.5 becomes:

$$\frac{G_{100}}{F_{PWN}} \propto \frac{\dot{E}^{\frac{1}{2}}/f_\Omega}{L_{PWN}}. \quad (10.6)$$

This equation can be used to obtain  $f_\Omega$  as a function of  $\dot{E}$ , by using  $L_{PWN}$  measured in an appropriate energy band. The choice of the energy band to measure  $L_{PWN}$  must fulfill two conditions: have a tight correlation with  $L_{PSR GeV}/f_\Omega$  and be a known function of  $\dot{E}$ .

Two good possibilities are the PWN luminosity in the TeV energy band ( $L_{PWN\ TeV}$ ) and the X-ray energy band ( $L_{PWN\ X}$ ). As I discussed in Chapter 9 Mattana et al. (2009) I argued that the expected distribution of  $L_{PWN\ TeV}$  is  $L_{PWN\ TeV} \propto \dot{E}^0$ . They also validated their argument with a sample of PWNe measured in the TeV energy range. By substituting their theoretical expectation,  $L_{PWN\ TeV} \propto \dot{E}^0$ , in Equation 10.5 I can rewrite Equation 10.5 as:

$$\frac{G_{100}}{F_{PWN\ TeV}} \propto \frac{\dot{E}^{\frac{1}{2}}}{f_{\Omega}} \quad (10.7)$$

$$f_{\Omega} \propto \left( \dot{E}^{\frac{1}{2}} \times \frac{F_{PWN\ TeV}}{G_{100}} \right). \quad (10.8)$$

Mattana et al. (2009) also argued that the expected distribution of  $L_{PWN\ X}$  is,  $L_{PWN\ X} \propto \dot{E}$ , and they also validated this argument with X-ray measurements. Therefore, I can rewrite Equation 10.5 with their theoretical expectation,  $L_{PWN\ X} \propto \dot{E}$ , as:

$$\frac{G_{100}}{F_{PWN\ X}} \propto \frac{\dot{E}^{-\frac{1}{2}}}{f_{\Omega}} \quad (10.9)$$

$$f_{\Omega} \propto \left( \dot{E}^{-\frac{1}{2}} \times \frac{F_{PWN\ X}}{G_{100}} \right). \quad (10.10)$$

In the work presented in this thesis I derived the  $f_{\Omega}$  as a function of  $\dot{E}$  for a Fermi GeV pulsar sample using the pulsar GeV flux and the TeV flux of their associated PWNe.

## 10.2 The Sample of Pulsars and Their Associated PWNe

In Chapter 9 I presented the PWNe TeV flux measurements made with Milagro for 14 Fermi GeV pulsars. From a literature survey I found the PWN TeV fluxes for 7 additional PWNe observed with IACTs. Among these 7 PWNe the SEDs of 5 PWNe are measured by H.E.S.S.: Crab, Vela, K3 in Kookabura, MSH 15-52, and G 21.5-0.9. In order to be consistent with the Milagro measurements, I integrated the energy flux within a 1 TeV energy band around 35 TeV using the H.E.S.S. SEDs. The derived energy flux of these sources are shown in Table: 10.1. The SEDs of the Crab, Vela and MSH 15-52 PWNe were measured in the energy ranges of 440 GeV - 40 TeV, 550 GeV - 65 TeV and 250 GeV - 40 TeV, respectively. Therefore, their integrated energy flux around 35 TeV can be obtained without any extrapolation. However, the SEDs of K3 in Kookabura and G 21.5-0.9 PWNe were measured in the energy ranges of 200 GeV - 25 TeV and 150 GeV - 5 TeV, respectively. Therefore, their integrated energy fluxes obtained around 35 TeV by extrapolation of their SEDs might be an overestimate, if there is a cutoff below 35 TeV.

VERITAS has published SEDs of the Boomerang and CTA 1 PWNe. In both cases the SEDs of these sources were measured in the energy range of 1-15 TeV. Therefore, as for K3 and G 21.5-0.9, the integrated energy flux obtained around 35 TeV by extrapolating the SEDs might be an overestimate, if there is a cutoff before 35 TeV. For all H.E.S.S. and VERITAS measured PWNe, errors of the integrated flux are estimated by a standard Gaussian Monte Carlo propagation of the uncertainties of the SED fit, with the 16<sup>th</sup> percentile as the lower  $1\sigma$  error bar and the 84<sup>th</sup> percentile as the upper.

Before applying these measurements to obtain  $f_{\Omega}$ , I examined whether these measure-

Pulsar Name	Association	$\log_{10}(\dot{E})$	$G_{100}$	Distance	$F_{PWN TeV}$
PSR		$\text{erg s}^{-1}$	$10^{-11}$ $\text{erg cm}^{-2} \text{ s}^{-1}$	(kpc)	$10^{-14}$ $\text{TeV s}^{-1} \text{ cm}^{-2}$
J0007+7303	CTA 1	35.65	$40.1 \pm 0.4$	$1.4 \pm 0.3$	$1.4^{+4.9}_{-1.1}{}^a$
J0534+2200	Crab	38.64	$129.3 \pm 0.8$	$2.0 \pm 0.5$	$2.3^{+6.0}_{-2.0}{}^b$
J0835-4510	Vela	36.84	$906 \pm 2$	$0.29 \pm 0.02$	$16.4^{+9}_{-7}{}^c$
J1420-6048	K3	37.01	$17.0 \pm 1.4$	$5.6 \pm 0.9$	$5.4^{+1.7}_{-1.3}{}^d$
	in Kookabura				
J1509-5850	MSH 15-52	35.71	$12.7 \pm 0.7$	$2.6 \pm 0.5$	$6.2^{+0.9}_{-0.8}{}^e$
J1833-1034	G21.5-0.9	37.53	$5.9 \pm 0.5$	$4.7 \pm 0.4$	$0.99^{+1}_{-0.6}{}^f$
J2229+6114	Boomrang	37.35	$25.3 \pm 0.4$	$0.8^{+0.15}_{-0.20}$	$1.3^{+15}_{-1.2}{}^g$

Table 10.1:  $G_{100}$  is the integrated phase-averaged energy flux of the pulsar GeV emission in the 0.1-100 GeV energy band.  $F_{PWN TeV}$  is the integrated energy flux of the PWN TeV emission in the 34.5-35.5 TeV energy band. Properties of a sample of GeV pulsars cataloged in the Fermi-LAT Second Pulsar Catalog and the TeV flux of their associated PWNe. (a). VERITAS Measurement, Energy flux derived by extrapolating the SED, reference [Aliu et al.(2013)] (b). H.E.S.S. Measurement, reference [Aharonian et al.(2006a)] (c). H.E.S.S. Measurement, reference [Aharonian et al.(2006b)] (d). H.E.S.S. Measurement, Energy flux derived by extrapolating the SED, reference [Aharonian et al.(2006d)] (e). H.E.S.S. Measurement, reference [Aharonian et al.(2005)] (f). H.E.S.S. Measurement, Energy flux derived by extrapolating the SED, reference [H. E. S. S. Collaboration et al.(2007)] (g). VERITAS Measurement, Energy flux derived by extrapolating the SED, reference [Aliu et al.(2013)]



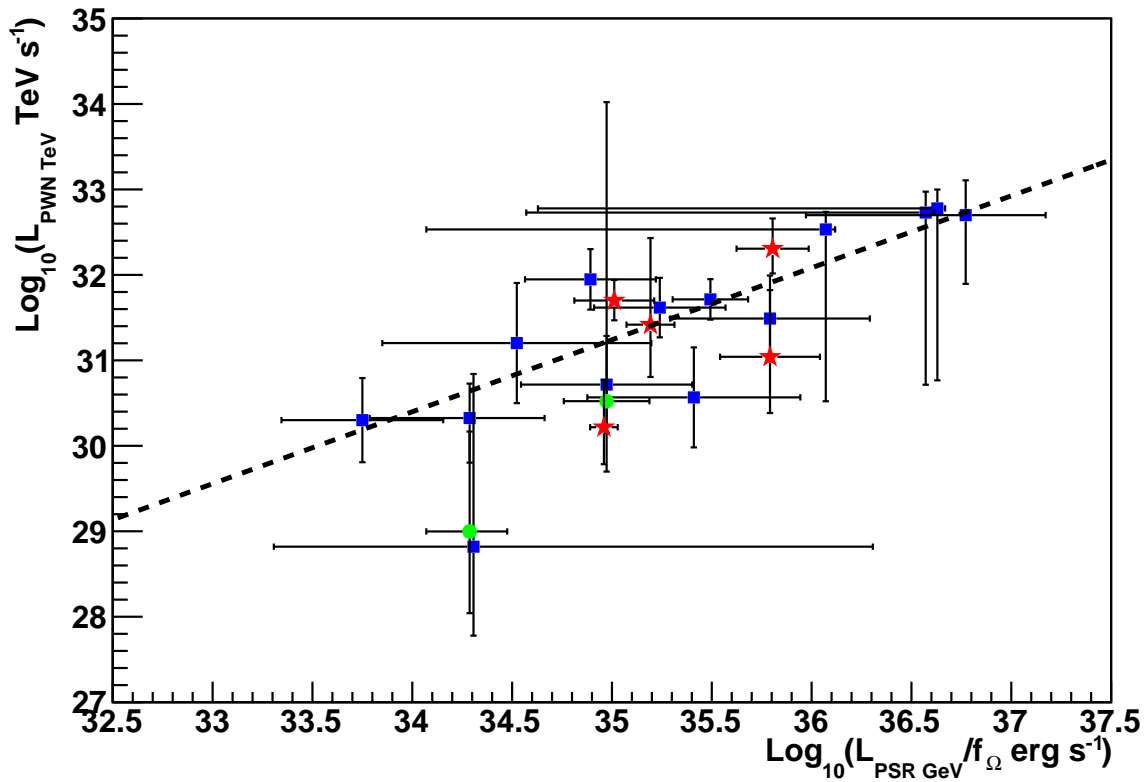


Figure 10.1: PWN TeV luminosity vs. Pulsar GeV luminosity normalized with respect to the flux correlation factor ( $f_{\Omega}$ ). Blue squares are measured by Milagro. Red stars are measured by H.E.S.S. Green circles are measured by VERITAS. The dotted line is the best fit line. The linear correlation coefficient is  $R = 0.8$ . The error bars are dominated by the distance measurement uncertainties.

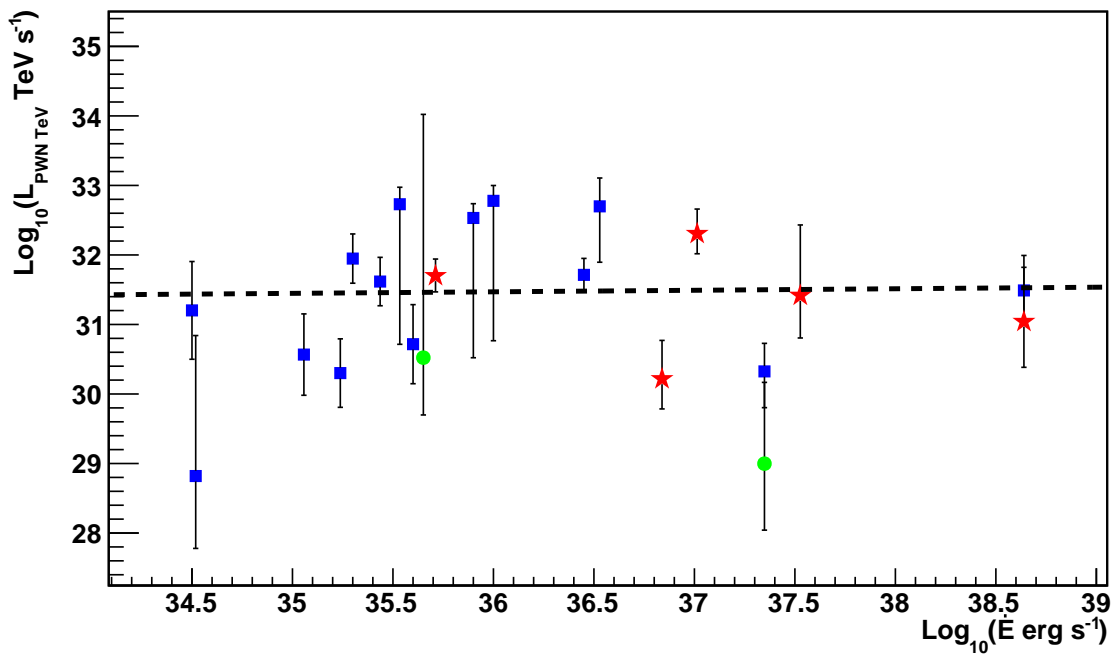


Figure 10.2: PWN TeV luminosity vs. spin-down luminosity ( $\dot{E}$ ) of the associated pulsar. Blue squares are for PWNe measured by Milagro, red stars by H.E.S.S., and green circles by VERITAS. The distance uncertainty contributes significantly to the error bars. The data are consistent with no dependence of  $L_{\text{PWN TeV}}$  on  $\dot{E}$ .

ments fulfill the two conditions required to apply the method: have a tight correlation with  $L_{PSR} GeV/f_{\Omega}$  and be a known function of  $\dot{E}$ . Using Figure 10.1 I examined the correlation between  $L_{PSR} GeV/f_{\Omega}$  and  $L_{PWN} TeV$ . The blue squares are PWNe measured by Milgro, the red stars by H.E.S.S., and the green circles by VERITAS. It appears that the PWNe measurements of the three experiments are generally consistent. Four of the TeV measurements ( $L_{PSR} = 34.3, 35.0, 35.2, 35.8$ ) have been extrapolated from lower energy bands, but do not appear to be outliers to the general scatter of the distribution. The large error bars on this plot are due to the distance uncertainties. Even though the error bars are large a reasonable correlation is obtained with a linear correlation coefficient of  $R = 0.82$ , and the best fit line for these data points yielded:

$$\log_{10}(L_{PWN} TeV) = (0.84 \pm 0.1) \log_{10}(L_{PSR} GeV/f_{\Omega}) + (1.7 \pm 3.8), \quad (10.11)$$

with  $\chi^2/NDF = 35.653/19$ . This provides evidence to conclude that this data fulfills the first condition listed above. Second, I examined the correlation between  $L_{PWN} TeV$  and  $\dot{E}$ , which was previously studied by Mattana et al. (2009) using H.E.S.S. measurements. The correlation between  $L_{PWN} TeV$  and  $\dot{E}$  for my PWN sample is shown in Figure 10.2. The best fit of these data points assuming a linear function yielded

$$\log_{10}(L_{PWN} TeV) = (0.02 \pm 0.06) \times \log_{10}(\dot{E}) + (30.6 \pm 2.5), \quad (10.12)$$

which has a slope consistent with zero and also with the slope obtained from the PWN sample in Mattana et al. (2009) of  $0.07 \pm 0.10$ . Those two observations led me to conclude that my data sample fulfills both required conditions.

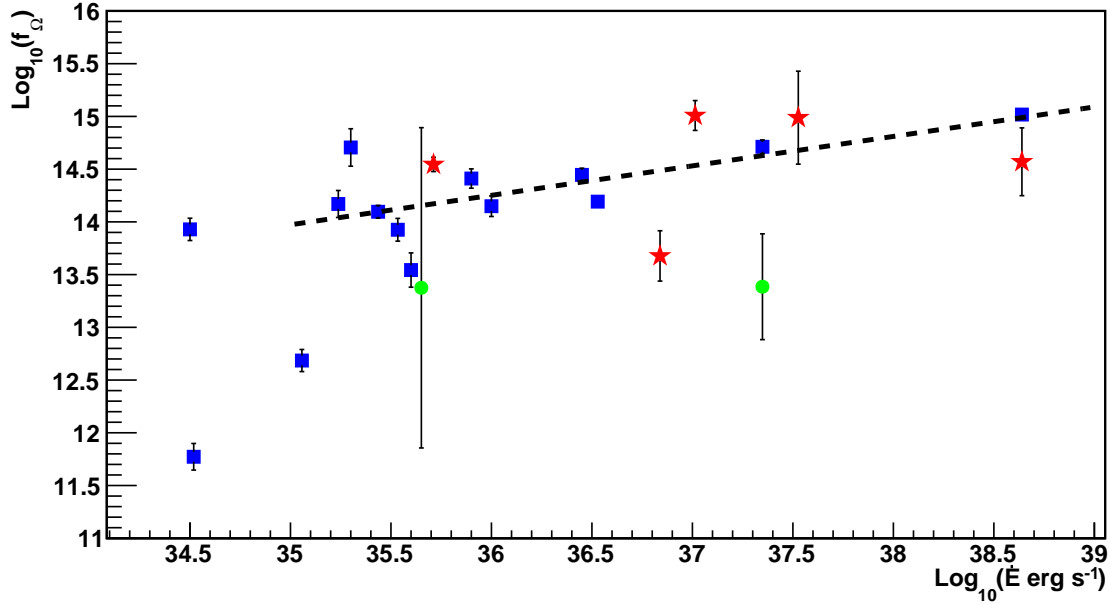


Figure 10.3: Experimentally obtained  $f_{\Omega}$  vs. pulsar spin-down luminosity  $\dot{E}$ . Blue squares are PWNe measured by Milagro, red stars by H.E.S.S, and green circles by VERITAS. The best fit line for the pulsars with  $\dot{E} > 10^{35.1}$  ergs s<sup>-1</sup> is shown as a dotted line.

### 10.3 Results and Discussion

The distribution of the experimentally obtained  $f_{\Omega}$  as a function of  $\dot{E}$ , using Equation 10.8, is shown in Figure 10.3. Note that the  $f_{\Omega}$  values obtained by this technique are not the actual values of  $f_{\Omega}$  but only its dependence on  $\dot{E}$ , because the correct normalization between the two energy bands is not predicted. It appears that above  $\dot{E} \approx 10^{35}$  erg s<sup>-1</sup>, the  $f_{\Omega}$  vs.  $\dot{E}$  distribution has a linear correlation with a slope of  $0.28 \pm 0.03$  ( $\chi^2/NDF = 33/18$ ), and below  $\dot{E} \approx 10^{35}$  ergs s<sup>-1</sup> the slope is steeper and  $f_{\Omega}$  distribution for a given  $\dot{E}$  has a tail towards smaller  $f_{\Omega}$  values.

This work allowed me to compare the experimentally obtained  $f_{\Omega}$  vs.  $\dot{E}$  distribution with the theoretically expected  $f_{\Omega}$  vs.  $\dot{E}$  distributions made by Pierbattista et al.(2012)

under four pulsar gap models. Pierbattista et al.(2012) studied four gamma-ray pulsar acceleration models. They synthesized a pulsar population based on a radio emission model and four gamma-ray pulsar gap models: Outer Gap (OG), Polar Cap (PC), Slot Gap (SG) and One Pole Caustic (OPC). Their model simulations of the correlation between  $f_{\Omega}$  and  $\dot{E}$  are shown in Figure 10.4. In all four model predictions, for pulsars with  $\dot{E} > 10^{35}$  ergs  $s^{-1}$ ,  $f_{\Omega}$  can be reasonably fit by a straight line in log – log space and the best fits give the following slopes:  $m_{PC} = 0.05 \pm 0.23$ ,  $m_{SG} = 0.003 \pm 0.004$ ,  $m_{OG} = 0.12 \pm 0.01$  and  $m_{OPC} = 0.026 \pm 0.007$ .<sup>1</sup> The slopes of the PC and SG models are consistent with zero, and the slope of the OPC is very small. The OG model is the only model that predicts a positive slope that is not consistent with zero. However, the small number of data points for the PC model have a large scatter, and, while the slope is consistent with zero, the uncertainty on the slope is much larger than for the other models.

I can now compare my results from Figure 10.3 with the expectations from the four pulsar gap models. The experimental  $f_{\Omega}$  vs.  $\dot{E}$  distribution has a non-zero slope of  $0.28 \pm 0.03$  for  $\dot{E} > 10^{35}$  erg  $s^{-1}$ . This would tend to disfavor the PC, SG and OPC models, which have slopes consistent with zero. However, the slope in our data is over twice that expected by the OG model for  $\dot{E} > 35$  ergs  $s^{-1}$ . Below  $\dot{E} = 10^{35}$  ergs  $s^{-1}$  the expected correlation between  $f_{\Omega}$  and  $\dot{E}$  for the OG model becomes more dispersed and the  $f_{\Omega}$  distribution for a given  $\dot{E}$  has a tail towards smaller  $f_{\Omega}$  values, especially for radio quiet pulsars<sup>2</sup>. This feature is also consistent with the experimentally obtained  $f_{\Omega}$  vs.  $\dot{E}$  distribution. If the two data points that have lower  $f_{\Omega}$ 's (PSR J0633+1746 and PSR J2021+4026) are radio quiet pulsars I would expect smaller  $f_{\Omega}$  values compared to radio loud pulsars. However, the radio

---

<sup>1</sup>These best fit parameters were provided in a private conversation by the authors of [Pierbattista et al.(2012)].

<sup>2</sup>Not detected by radio telescopes.

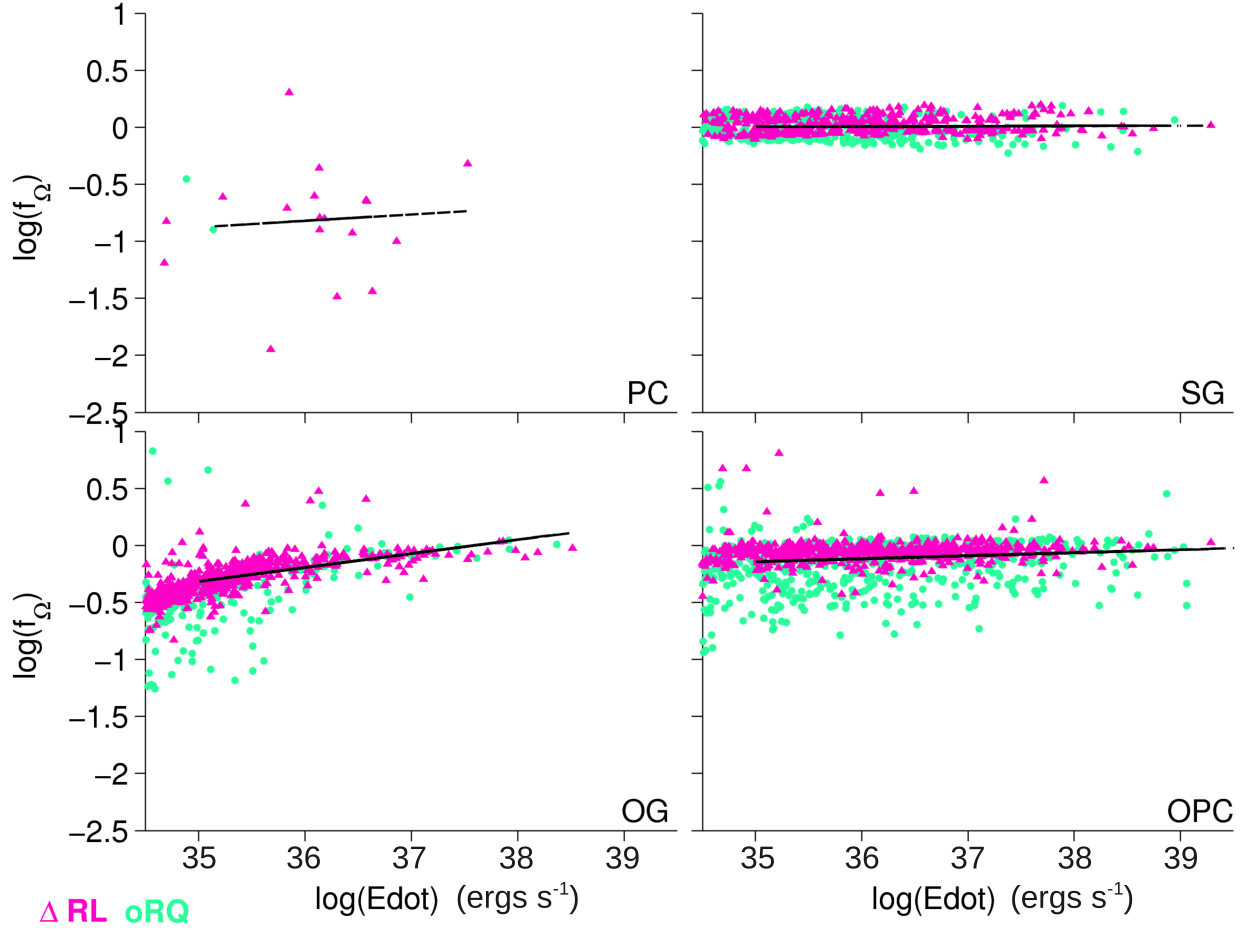


Figure 10.4: The distribution of the beaming factor ( $f_{\Omega}$ ) as a function of spin-down luminosity ( $\dot{E}$ ) for four models derived by [Pierbattista et al.(2012)]. This plot was reproduced by M. Pierbattista with linear fits for pulsars above  $\dot{E} = 10^{35}$  ergs s $^{-1}$ . For the original figure refer to [Pierbattista et al.(2012)]. Purple and green markers refer to the radio-loud and radio-quiet pulsars, respectively. Black lines refer to the best linear fits for the pulsars with  $\dot{E} > 10^{35}$  ergs s $^{-1}$ .

measurements at 1400 MHz ( $S_{1400}$ ) for these two pulsars are only upper limits: for PSR J0633+1746  $S_{1400} < 0.507$  mJy and for PSR J2021+4026  $S_{1400} < 0.02$  mJy. Therefore, it is unclear whether to categorize them as radio loud or radio quiet pulsars. By considering both features above and below  $\dot{E} \approx 10^{35}$  ergs s $^{-1}$ , I can conclude that my data sample has some features which favor the OG model for pulsar emission in the energy range 0.1-100 GeV over the SG and OPC models, even though the OG model does not quantitatively match our measurements. However, I cannot reach any conclusions about the PC model, because of the lack of data-points in the simulated  $f_{\Omega}$  vs.  $\dot{E}$  distribution.

The discrepancies between my experimental results and the model expectations might be due to the systematic limitations or inadequacies of Pierbattista et al's simulations or biases in my data sample. As Pierbattista et al. mention, results of all four simulated models are lacking pulsars with  $\dot{E} > 3 \times 10^{35}$  ergs s $^{-1}$  and characteristic age  $< 100$  kyr, and over-predict the number of low  $\dot{E}$  pulsars. Furthermore they also mention that the simulated OG model fails to explain many of the most important pulsar population characteristics. This could certainly effect their  $f_{\Omega}$  vs.  $\dot{E}$  distributions. Therefore, we can not provide tight constraints using this synthetic pulsar population. However, a comparison of my results with an improved model simulation could provide tighter constraints.

My estimates of  $f_{\Omega}$  may also be biased if there is an unexpected residual dependence of the TeV luminosity on  $\dot{E}$ , which is hidden in the TeV data scatter, or depending on the selected TeV energy range. The energy range of a 1 TeV band around 35 TeV was chosen because of the Milagro dataset. Ideally, I would prefer to do this study with a more uniform sample of PWN TeV energy fluxes obtained around the inverse Compton peak of each individual PWN. This result also depends on the relation  $L_{PSR GeV} \propto \dot{E}^{\frac{1}{2}}$ . In order to account for systematic errors of the exponent of  $\dot{E}$ , I can introduce an systematic

error of  $\pm 0.1$  to the exponent of this relation,  $L_{PSR} \text{ GeV} \propto \dot{E}^{0.5 \pm 0.1}$ . After propagating this systematic error to the slope of  $\log_{10}(f_{\Omega})$  vs.  $\log \dot{E}$  distribution, the slope becomes  $0.28 \pm 0.03_{\text{statistical}} \pm 0.1_{\text{systematic}}$ . This shows that even after introducing a systematic error of  $\pm 0.1$ , the slope is still not consistent with zero.



# Chapter 11

## Milagro Observations of Fermi-LAT Galactic Sources

In 2009 the Milagro collaboration performed a targeted search [Abdo et al.(2009a)] for Fermi-LAT bright sources (also known as the 0FGL catalog) [Abdo et al.(2009b)] using the Milagro sky maps and found that Fermi bright sources, that were measured at or above 3 standard deviations in significance ( $3\sigma$ ) by Milagro were dominated by Fermi-LAT bright sources that have associations with known pulsars. The Fermi-LAT bright source list was made using the first 3 months of Fermi-LAT data. In 2012 the Fermi-LAT collaboration extended their source list using the bright sources in the first 2 years of Fermi-LAT data. The new source list is called the Fermi-LAT 2FGL catalog [Nolan et al.(2012)]. This new catalog increased the number of Fermi-LAT sources that have associations with known pulsars and in the Milagro skycoverage by 32. Therefore, I extended the previous Milagro targeted search by making a candidate list from these 32 new Fermi-LAT sources. Results from the search source in this new source list is summarized in Table 11.1. In this list, the FDR procedure with a 1%

contamination classified 3 Fermi-LAT sources (2FGL J2238.4+5902, 2FGL J2030.0+3640 and 2FGL J1928.8+1740c) as having coincident TeV emission.

The Milagro targeted search on 0FGL sources measured the Milagro flux/flux limit at the locations of 16 Fermi-LAT sources that were associated with known pulsars [Abdo et al.(2009b)]. Among these 16 sources, 9 passed the standard FDR cut with a 1% contamination. 0FGL J2055.5+2540, 0FGL J2214.8+3002 and 0FGL J2302.9+443 were categorized as sources of unknown source type and 0FGL J1954.4+2838 was identified as a source with a spatial association with a known supernova remnant. In the 2FGL catalog these four sources have been identified with associations to known pulsars, and only 0FGL J1954.4+2838 passed the standard FDR cut of a 1% contamination. Therefore altogether 52 Fermi-LAT sources detected by Fermi-LAT have been observed by Milagro and 13 Fermi-LAT sources that have associations with known pulsars were identified with TeV associations.

One can use this sample to study how the fraction of pulsars  $F_T$  with a TeV counterpart changes as a function of the time-averaged GeV flux.  $F_T$  can be defined as the fraction of pulsars that passed the standard FDR cut in a given bin of GeV flux,

$$F_T = \frac{\text{Number of FDR true candidates in a given flux bin}}{\text{Total number of candidates in a given flux bin}}. \quad (11.1)$$

As shown in Figure 11.1  $F_T$  increases with the Fermi flux. The best fit of the  $F_T$  vs. Fermi flux assuming a liner function yield:

$$F_T = (0.49 \pm 0.09) \times (\text{Time-average Fermi flux}) + (3.9 \pm 0.7), \quad (11.2)$$

with  $\chi/NDF = 0.68/3$ . The fit of the  $F_T$  vs. Fermi flux assuming a constant has a

$\chi/NDF = 14.22/4$ . This means that the improvement of the best fit to a linear function is  $3.4\sigma$ . This gives evidence that the brighter GeV sources in the 2FGL catalog that have associations with known pulsars are more likely to have a detectable TeV counterpart.

However, one has to interpret this result with care, because of the known caveats in the 2FGL catalog. The GeV flux measurements reported in the 2FGL catalog are time-averaged fluxes of regions with GeV gamma-ray excesses. If there is a pulsar associated with this region, then the GeV emissions are coming from the pulsar, its associated PWN and from the Galactic diffuse GeV emission. Therefore, the time-averaged flux is the average of these 3 components. The ratio of pulsar time-averaged flux to PWN flux is not always the same. For example, the GeV flux only from the Crab PWN in the energy range of 10 - 316 GeV is  $486 \pm 188 \times 10^{-12} \text{ erg cm}^{-2} \text{ s}^{-1}$  [Acero et al.(2013)] and the time-average flux from the 2FGL catalog in the same energy range is  $9208.41 \pm 226 \times 10^{-12}$ . For 2FGL J1959.5+2047 the unpulsed component of the time-average GeV flux is not visible after removing the pulsed component [Acero et al.(2013)]. Thus for the region around the Crab 75% of the time-average GeV flux comes from the time-averaged pulsar emission, but for 2FGL J1959.5+2047  $\sim 100\%$  of the time-average GeV flux is coming from the time-average pulsar emission. Another disadvantage of the 2FGL flux measurements is the contamination of Galactic diffuse GeV emission. The best example is 2FGL J1928.8+1740c, which was measured with  $4.03 \sigma$  by Milagro. This source was not detected either as a GeV pulsar [Abdo et al.(2013)] or as a PWN [Acero et al.(2013)] after removing the Galactic diffuse emission.

One may argue that the dominant GeV flux emission for this set of 2FGL sources is coming from the time-average pulsar flux, because for the Crab 75% of the flux is coming from the pulsar and for 2FGL J1959.5+2047  $\sim 100\%$  of the time-average GeV flux is coming

from the pulsar. However, the time-averaged flux of a pulsar is a parameter that has to be interpreted with extra care. The time-averaged flux of a pulsar is the average flux that can be observed from the earth, but not the true flux emitted by the pulsar. The true flux of the pulsar is the phase-averaged flux. For some pulsars the width of the pulse is very narrow, for other pulsars the pulse width is very wide. When the pulse is narrow the time-averaged flux is considerably less than the phase-averaged flux, but for wide pulses the time-averaged flux can become roughly equal to the phase-averaged flux. This can be led to misidentify faint pulsars as bright pulsars and vice versa. The time-averaged flux of J2030+3641 is greater than the time-averaged flux of J0631+1036. Therefore, one can misidentify J2030+3641 as a pulsar brighter than J0631+1036. However, J0631+1036 is the brighter pulsar, because the phase-averaged flux, which is the true flux of the pulsar, is smaller for J2030+3641 than the phase-average flux of J0631+1036. This observation leads me to conclude that the time-averaged flux is a misleading parameter to determine the brightness of a pulsar.

Since phase-averaged flux is a better estimator for pulsar brightness, one can propose to remake Figure 11.1 with the phase-averaged fluxes. As shown in Figure 11.2  $F_T$  also increases with the phase-averaged Fermi flux. The best fit of the  $F_T$  vs. Fermi flux assuming a linear function yields:

$$F_T = (0.28 \pm 0.15) \times (\text{Time-average Fermi flux}) + (3.3 \pm 1.5), \quad (11.3)$$

with  $\chi/NDF = 0.95/4$ . The fit of the  $F_T$  vs. Fermi flux assuming a constant has a  $\chi/NDF = 2.16/5$ . This means that the improvement of the best fit to a linear function is  $1\sigma$ . This gives a  $1.3\sigma$  evidence to say that the brighter GeV pulsars are more likely to have a detectable TeV counterpart. One also should account for the fact that phase-average flux

still does not give the correct estimate for the pulsar brightness. In order to get the correct brightness, the phase-averaged flux has to be corrected with the beaming factor,  $f_{\Omega}$ . As shown in Figure 10.4 the theoretically expected  $f_{\Omega}$  can be varied within about an order of magnitude. Therefore, the correction can be quite substantial, which can alter equation 11.3

Altogether, the GeV flux measurements reported in the 2FGL catalog are coming from 3 different GeV sources: pulsars, PWNe and Galactic diffuse emission. Therefore, in the 2FGL catalog one can not identify a single physical source that produces the measured GeV fluxes. However, this data set gives a  $3\sigma$  evidence to say that brighter GeV sources in the 2FGL catalog that have associations with known pulsars are more likely to have a detectable TeV counterpart. As it is shown in this chapter and in chapter 9 there is no evidence to say that brighter GeV pulsars are more likely to have a detectable TeV counterpart. Therefore, the correlation between 2FGL GeV sources and their associated TeV emission might be due to the PWN component or due to the Galactic diffuse emission component. It is also possible that this correlation is a selection effect.

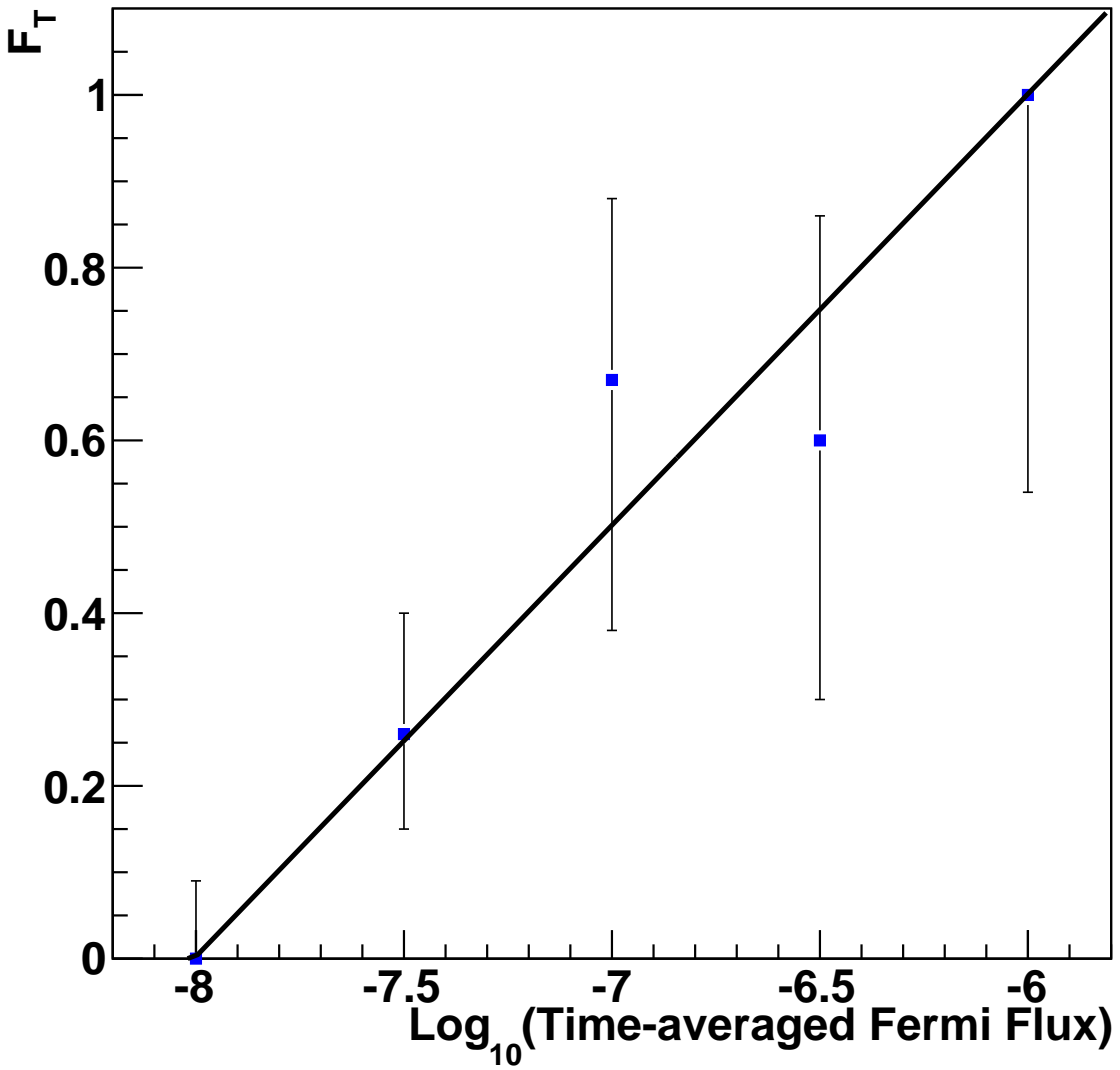


Figure 11.1: The fraction of Fermi-LAT sources seen by Milagro as a function of half-decade bins of the integrated time-averaged Fermi flux ( photons  $\text{cm}^{-2} \text{s}^{-1}$  ) in the energy range from 100 MeV to 100 GeV.

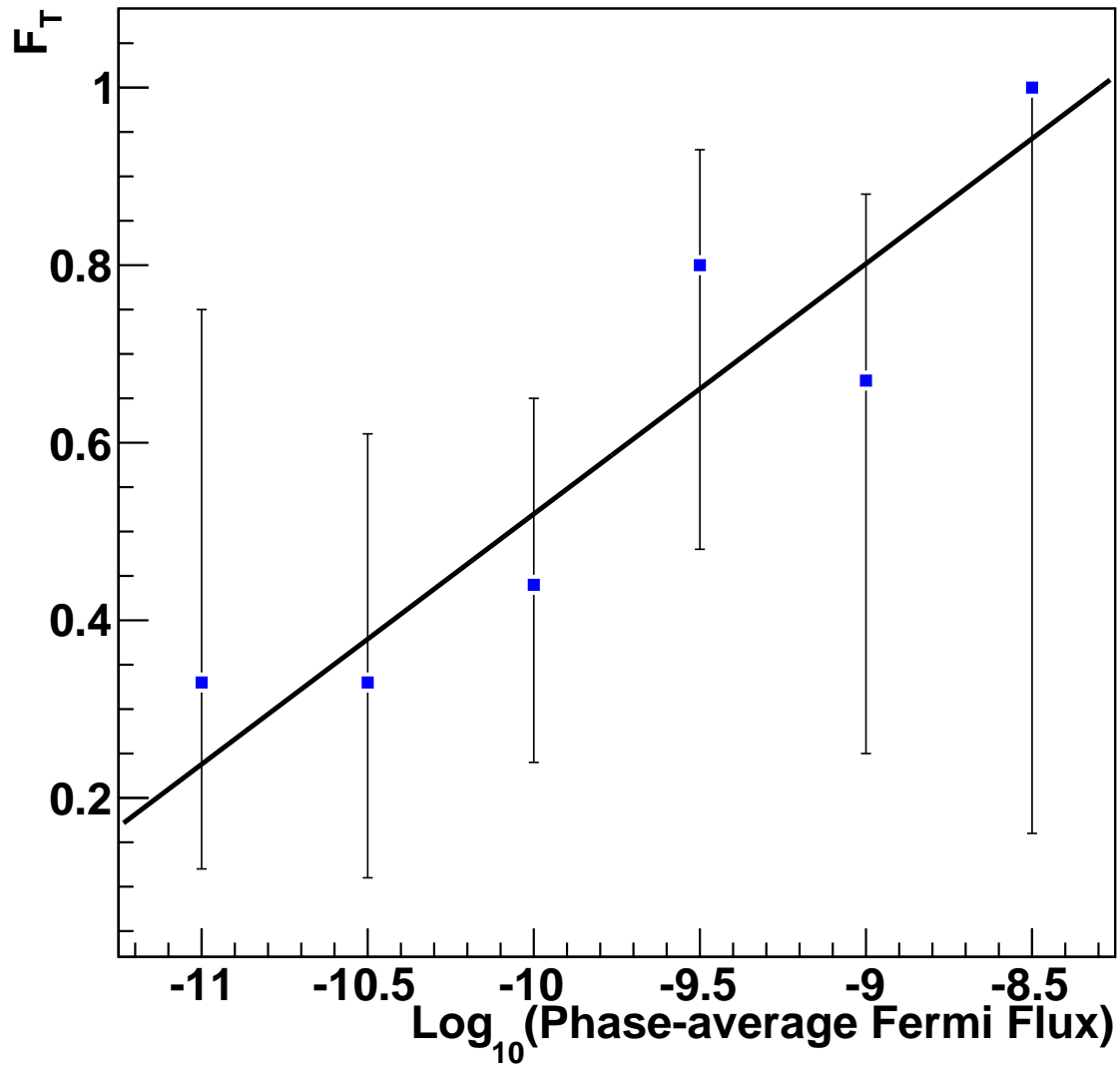


Figure 11.2: The fraction of Fermi-LAT sources seen by Milagro as a function of half-decade bins of the integrated phase-averaged Fermi flux (  $\text{photons cm}^{-2} \text{s}^{-1}$  ) in the energy range from 100 MeV to 100 GeV.

Fermi Name 2FGL	RA (deg)	DEC (deg)	l (deg)	b (deg)	Flux/Flux Limit ( $\times 10^{-17} \text{TeV}^{-1}$ $\text{s}^{-1} \text{cm}^{-2}$ )	Source Type	Significance $\sigma$	Associated source
J0023.5+0924	5.89	9.41	111.5	-52.85	< 22.42	psr	-0.73	PSR J0023+09
J0034.4-0534	8.61	-5.58	111.55	-68.08	< 54.58	PSR	-2.06	PSR J0034-0534
J0102.9+4838	15.74	48.65	124.9	-14.18	< 22.31	psr	0.51	PSR J0103+48
J0205.8+6448	31.45	64.81	130.74	3.07	< 20.75	PSR	-0.88	PSR J0205+6449
J0218.1+4233 <sup>1</sup>	34.53	42.55	139.5	-17.51	< 41.80	PSR	2.94	PSR J0218+4232
J0248.1+6021	42.04	60.36	136.89	0.69	< 38.32	PSR	1.54	PSR J0248+6021
J0308.3+7442	47.08	74.71	131.73	14.23	< 53.95	psr	-0.15	PSR J0308+7442
J0340.4+4131	55.1	41.53	153.78	-11.01	< 14.87	PSR	-0.52	PSR J0340+4130
J0659.7+1417	104.93	14.29	201.05	8.27	< 37.31	PSR	1.18	PSR J0659+1414
J0751.1+1809	117.78	18.15	202.7	21.09	< 19.51	PSR	-0.43	PSR J0751+1807
J1023.6+0040	155.92	0.68	243.43	45.78	< 43.66	psr	-0.33	PSR J1023+0038
J1142.9+0121	175.74	1.35	267.56	59.44	< 37.41	psr	-0.9	PSR J1142+01
J1301.5+0835	195.39	8.58	310.76	71.3	< 21.62	psr	-0.82	PSR J1301+08
J1312.7+0051	198.18	0.85	314.82	63.23	< 58.01	psr	0.5	PSR J1312+00
J1549.7-0657	237.43	-6.96	1.23	35.03	< 88.75	psr	-0.8	PSR J1549-06
J1714.0+0751	258.5	7.86	28.84	25.21	< 18.13	PSR	-1.58	PSR J1713+0747
J1745.6+1015	266.4	10.27	34.84	19.23	< 32.77	psr	0.48	PSR J1745+10
J1810.7+1742	272.69	17.7	44.62	16.76	< 18.39	psr	-0.6	PSR J1810+17
J1846.4+0920	281.61	9.34	40.7	5.34	< 23.81	PSR	-0.54	PSR J1846+0919
<b>J1928.8+1740c</b>	<b>292.22</b>	<b>17.68</b>	<b>52.87</b>	<b>0.03</b>	<b>46.41±11.50</b>	<b>psr</b>	<b>4.03</b>	<b>PSR J1928+1746</b>
J1957.9+5033	299.48	50.56	84.61	10.98	< 28.56	PSR	1.41	PSR J1957+5033
J1959.5+2047	299.9	20.79	59.18	-4.7	< 15.32	PSR	-0.85	PSR J1959+2048
<b>J2030.0+3640</b>	<b>307.51</b>	<b>36.68</b>	<b>76.12</b>	<b>-1.45</b>	<b>42.68±9.55</b>	<b>PSR</b>	<b>4.46</b>	<b>PSR J2030+3641</b>
J2017.3+0603	304.35	6.05	48.63	-16.02	< 27.2	PSR	-0.71	PSR J2017+0603
J2043.2+1711	310.81	17.18	61.9	-15.3	< 17.82	PSR	-0.76	PSR J2043+1710
J2043.7+2743	310.95	27.72	70.65	-9.14	< 14.62	PSR	-0.72	PSR J2043+2740
J2046.7+1055	311.69	10.93	57.02	-19.57	< 37.49	psr	0.99	PSR J2047+10
J2129.8-0428	322.47	-4.48	48.93	-36.96	< 104.35	psr	0.55	PSR J2129-04
J2215.7+5135	333.94	51.59	99.89	-4.18	< 13.28	psr	-1.1	PSR J2215+51
J2234.7+0945	338.69	9.75	76.29	-40.43	< 31.44	psr	0.38	PSR J2234+09
<b>J2238.4+5902</b>	<b>339.61</b>	<b>59.05</b>	<b>106.55</b>	<b>0.47</b>	<b>50.41±11.10</b>	<b>PSR</b>	<b>4.53</b>	<b>PSR J2238+5903</b>
J2239.8+5825 <sup>2</sup>	339.97	58.43	106.41	-0.16	< 51.39	PSR	3.01	PSR J2240+5832

Table 11.1: Summary of the search with  $\lambda = 0.01$  for TeV emission from the pulsars in the 2FGL list that were not listed in the 0FGL. (Note that we used the same abbreviations for the source type as the 2FGL: PSR = Pulsar identified by pulsations and psr = Pulsar identifies by spatial association.) The Milagro flux derived at 35 TeV is given for the candidates that passed the  $\lambda = 0.01$  FDR cut and 95% confidence level upper limits are given for the rest.



# Chapter 12

## Conclusions

In this thesis I presented the GeV-TeV correlations of point-like sources, upper limits to the Synchrotron Self-Compton model for BL Lac type AGNs, and constraints for the pulsar GeV emission models. I also discussed the GPS Timing and Control system for the High Altitude Water Cherenkove (HAWC) observatory, for which I developed the FPGA firmware. HAWC is a next generation TeV gamma-ray observatory, which will begin to survey the northern hemisphere of the sky at its full capacity in 2015.

My data sample was obtained from three targeted searches for extragalactic sources and one targeted search for pulsars, using the existing Milagro sky maps. The detection threshold for these targeted searches was derived using the False Discovery Rate procedure with a 1% contamination fraction. The first extragalactic candidate list was made from extragalactic candidates in the Fermi-LAT 2FGL catalog and the second list from the extragalactic candidates in the TeVCat catalog. From these two extragalactic lists, Markarian 421 was the only extragalactic source that Milagro was able to detect. The time averaged flux measurements of Markarian 421 measured by Milagro compared to the IACT measurements of the transient states of Markarian 421 lead me to conclude that the Markarian 421 stays in

the low flux state most of the time. A research paper that summarizes the above results, of which I was the primary author, was accepted to the Astroparticle Physics Journal. The third extragalactic candidate list is a list of potential TeV emitting BL Lac candidates that was compiled using x-ray observations of BL Lac objects and a Synchrotron Self-Compton model. Milagro's sensitivity was not enough to detect any of those candidates. However, the 95% confidence flux upper limits of those sources were above the predicted flux, so the Synchrotron Self-Compton model used to predict TeV emission is still viable. This work was published in [Abeysekara & Milagro Collaboration(2013)].

The pulsar candidate list was made from GeV pulsars in the Fermi-LAT second pulsar catalog. This search was able to measure TeV emission from associated PWNe for 14 GeV pulsars. The TeV PWN luminosity ( $L_{PWN\ TeV}$ ) vs.  $\dot{E}$  distribution and the  $L_{PWN\ TeV}$  vs.  $\tau_c$  distribution of this sample were both consistent with the leptonic model proposed by [Mattana et al.(2009)]. For this sample, a linear correlation between pulsar GeV emission and PWN TeV emission was observed, with a linear correlation coefficient of  $R = 0.82$ . This observed GeV –TeV correlation suggests the possibility of a linear relationship between gamma-ray emission mechanisms in pulsars and TeV emission mechanisms in PWNe. However, it is not possible to explain this linear relationship using the electron-positron populations of curvature radiation inside the magnetosphere and synchrotron radiation in the PWN. An alternative possibility is a linear relationship between the ambient photon density in the PWN and the pulsar wind current. A more detailed theoretical study will be needed to fully understand this correlation.

The correlations between PWN detectability and  $\dot{E}/d^2$ , TeV efficiency ( $\epsilon_\gamma$ ) and  $\dot{E}$ , and TeV efficiency and  $\tau_c$  were studied for this sample of 14 GeV pulsars. There was no correlation between PWN detectability and  $\dot{E}/d^2$ , which suggests that the current rate of

energy a pulsar feeds its associated PWN is not the only parameter relevant for the PWN TeV flux. There were no correlations between  $\varepsilon_\gamma$  and  $\dot{E}$ , and  $\varepsilon_\gamma$  and  $\tau_c$ . However, the two PWNe associated with the youngest pulsars have an  $\varepsilon_\gamma$  more than an order of magnitude less than the other PWNe. This observation supports the argument that TeV photons are produced by the accumulated electrons in the PWN.

In this thesis I also presented a new multiwavelength technique that I developed to isolate the flux correlation factor ( $f_\Omega$ ) of GeV pulsars as a function of pulsar spin down luminosity. This technique requires three input parameters: pulsar spin down luminosity, pulsar phase-averaged GeV flux, and TeV flux from the associated PWN. The measured correlation has some features that favor the Outer Gap model over the Polar Cap, Slot Gap and One Pole Caustic models for pulsar emission in the energy range of 0.1 to 100 GeV, though these simulated models failed to explain many of the most important pulsar population characteristics. A research paper that summarizes this new technique, of which I was the first author, was submitted to the *Astrophysical Journal*.

Altogether my findings support that the TeV emission from PWNe are produced by the Inverse Compton scattering of the accumulated electrons. Using this property, I developed a new multiwavelength technique to study GeV pulsar acceleration mechanisms. In this thesis work I successfully applied this technique to constrain the existing GeV pulsar gap models. My attempt to constraint a Synchrotron Self-Compton model for BL Lac objects using the Milagro data set motivate the significance of building more sensitive gamma-ray observatories, such as HAWC.

# APPENDIX

# Appendix

## Energy Estimators

### Neural Network Based Energy Estimator

An improved energy estimator for Milagro was developed using the Bayesian Neural Network (BNN) in the ROOT framework [Zhong et al.(2011)]. The BNN was trained using five input parameters: incident angle, core radius, nFit, nCalMU and A5 (refer to Chapter 4 for the definitions of these parameters). Both test and training samples were also selected using two cuts:  $A5 > 1$  and  $FRASOR > 0.2$ . The A5 cut removes the hadron like showers in the data sample, and the FRASOR cut removes the low energy events which barely passed the Milagro threshold. The Milagro simulated data sample has only about 30000 effective events. I divided the sample into two and trained the BNN using one sample and used the other sample for testing. I will call the new energy estimator EBNN.

Figure A.1 shows the comparison between the EBNN obtained using MC simulated data and are obtained using a sample of real Milagro data. As it can be seen in the top histogram in Figure A.1, the simulated EBNN follows the general trend of the EBNN obtained with real data. However, they are not consistent with the one sigma error bars. The bottom histogram

in Figure A.1 shows the ratio between the EBNN obtained with a real data sample and the EBNN obtained with a simulated data sample. If the simulations are ideal this ratio should equal 1. Data points are closer to 1 in the range from 3.25 to 4.25, but deviated from 1 at both ends.

Figure A.2 shows the correlations between the energy estimators and the expected true energy. Note that these plots were made using a simulated data sample, therefore the expected energy is known. The histogram to the left shows the correlation between EBNN and expected energy, which has a linear correlation coefficient of 0.84. The histogram to the right shows the correlation between FRASOR, the old energy estimator, and the expected energy, which has a linear correlation coefficient of 0.54. The improvement of the linearity is substantial for the EBNN compared to the existing energy estimator, FRASOR.

Figure A.3 shows the typical dependence of EBNN on the expected energy. Note that the width of a single EBNN bin covers a wide range of energies and these energies overlap significantly. The corresponding figure with FRASOR is shown in Figure A.4. Distributions are narrower for the EBNN compared to the FRASOR.

## The Gamma-Table

The Gamma-Tables are a set of tables that summarize the Milagro expected excess of a Milagro map made with the spectral optimization of  $E^{-2.6}$  for a source with a known spectrum and at a known location in the sky. Each table summarizes the Milagro expected excess for a given Milagro epoch and for a source in a given declination. The naming convention of files is, E<N>\_dec<ddd>.0.dat, where <N> is the Milagro epoch and <ddd> is the declination of a source in degrees. For example, “E8\_dec42.0.dat” summarizes the

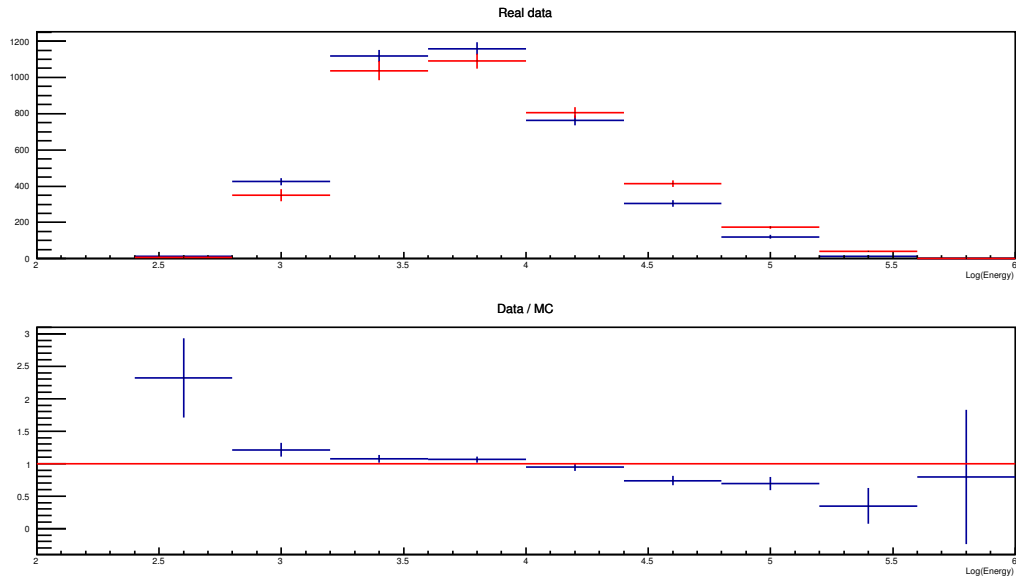


Figure A.1: Comparison between Monte Carlo simulated data and real data for cosmic-rays. In the top figure, the red data points show the distribution of the energy estimator of the Monte Carlo simulated data. In the top figure, the blue data points show the distribution of the energy estimator of the real data. In the bottom figure, the blue data points show the ratio data/monte Carlo simulations.

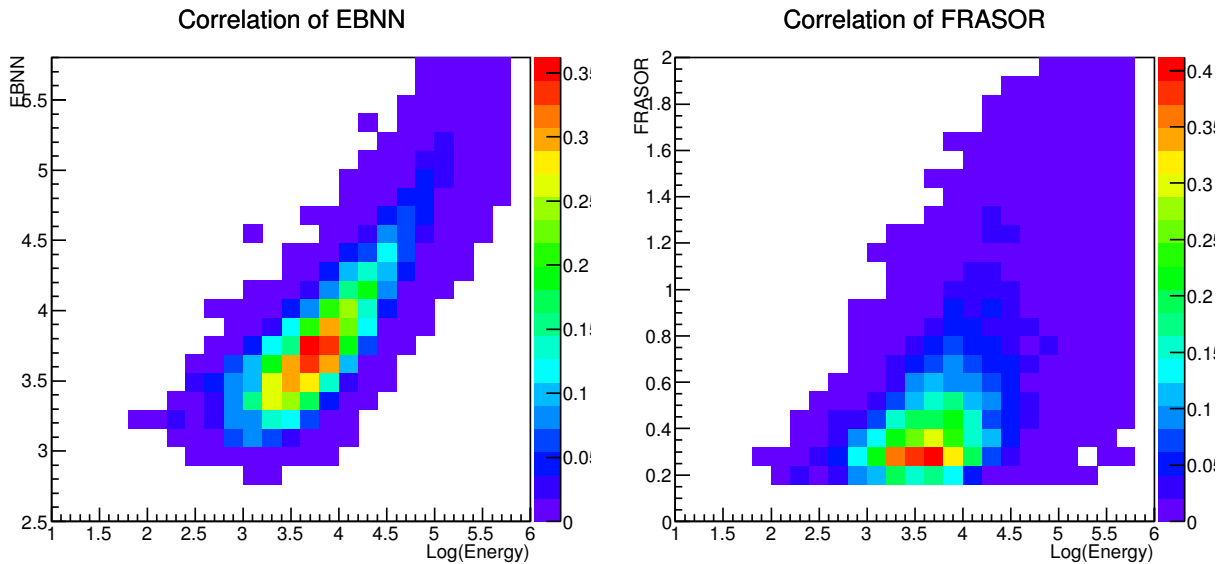


Figure A.2: Correlation between the energy estimators and true energy. Histogram to the left is the correlation between EBNN and  $\log(\text{Energy})$ . Histogram to the right is the correlation between FRASOR, the old energy estimator, and  $\log(\text{Energy})$ . Both of these plots were made using a simulated data sample.

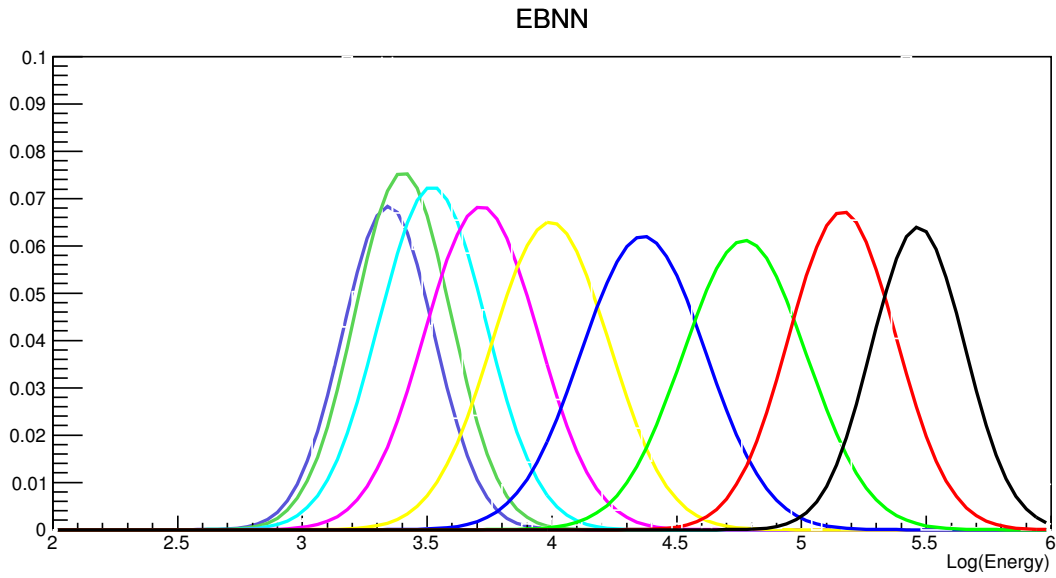


Figure A.3: Unit-normalized distribution of true energies for events in EBNN bins, 0.2-0.4, 0.4-0.6, 0.6-0.8, 0.8-1.0, 1.0-1.2, 1.2-1.4, 1.4-1.6, 1.6-1.8 and 1.8-2.0.

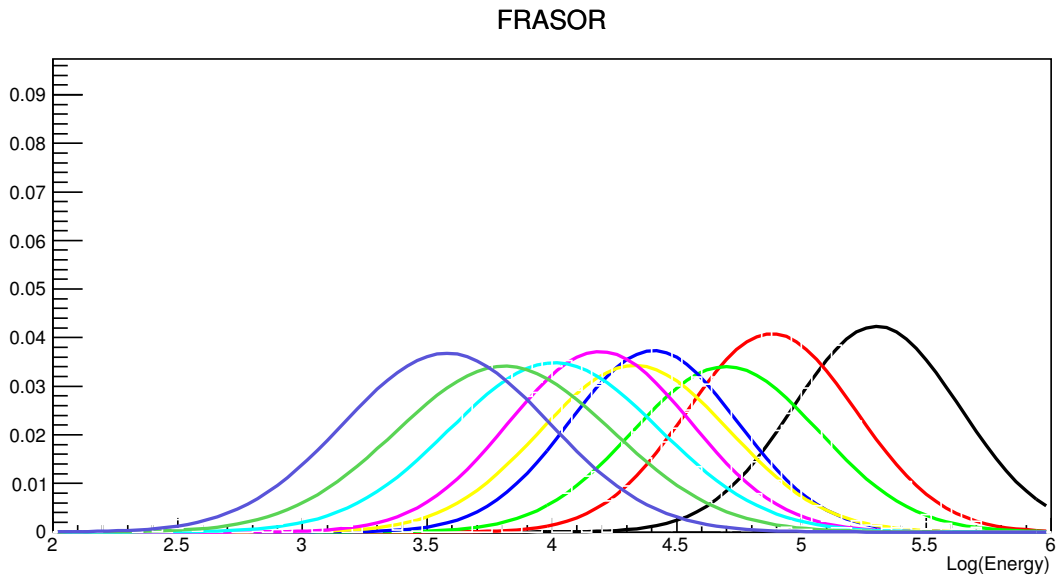


Figure A.4: Unit-normalized distribution of true energies for events in FRASOR bins, 0.2-0.4, 0.4-0.6, 0.6-0.8, 0.8-1.0, 1.0-1.2, 1.2-1.4, 1.4-1.6, 1.6-1.8 and 1.8-2.0.



Epoch	live time in days
1	0.
2	322.2
3	387.2
4	443.9
5	160.2
6	156.2
7	181.3
8	257.9
9	386.1

Table A.1: Epoch live times

Milagro expected excess per day of Milagro epoch 8 for a source at declination 42.0. Each table has 4860 rows and 42 columns. The first column is the spectral index and the second column is the  $\log_{10}(\text{Energy cutoff})$  of the simulated source. Every 5<sup>th</sup> column starting from column 3 is the expected excess from FRASOR bin 1 through 10. Every 5<sup>th</sup> column starting from column 4 is the error of expected excess from FRASOR bin 1 through 10. Every 5<sup>th</sup> column starting from column 5 is the mean energy of events that landed in each FRASOR bin. Every 5<sup>th</sup> column starting from column 6 is the standard deviation of energy for the events that landed in each FRASOR bin. For example, column 3, 4, 5 and 6 are the expected excess, error of the expected excess, mean energy of the events and the standard deviation of energy for the events landed in FRASOR bin 1,  $0 < \text{FRASOR} < 0.2$ . Note that all of these excess measurements are per day, in order to get the total excess from the full epoch this number has to be multiplied by the number of live days. Table A.1 summarizes the number of live days in each epoch.

# BIBLIOGRAPHY

# BIBLIOGRAPHY

- [Abdo(2007)] Abdo, A. A. 2007, Ph.D. Thesis,
- [Abdo et al. (2007)] Abdo, A. A., et al. 2007, *ApJ. Lett.*, 664, L91
- [Abdo et al.(2009a)] Abdo, A. A., Allen, B. T., Aune, T., et al. 2009, *ApJ. Lett.*, 700, L127
- [Abdo et al.(2009b)] Abdo, A. A., Ackermann, M., Ajello, M., et al. 2009, *ApJS*, 183, 46
- [Abdo et al.(2012)] Abdo, A. A., Allen, B. T., Atkins, R., et al. 2012, *ApJ.*, 750, 63
- [Abdo et al.(2013)] Abdo, A. A., Ajello, M., Allafort, A., et al. 2013, *ApJS*, 208, 17
- [Abeysekara & Milagro Collaboration(2013)] Abeysekara, A. U., & Milagro Collaboration 2013, AAS/High Energy Astrophysics Division, 13, #123.01
- [Acciari et al.(2009)] Acciari, V. A., Aliu, E., Arlen, T., et al. 2009, *ApJ. Lett.*, 703, L6
- [Acciari et al.(2011)] Acciari, V. A., Arlen, T., Aune, T., et al. 2011, *ApJ.*, 729, 2
- [Acero et al.(2013)] Acero, F., Ackermann, M., Ajello, M., et al. 2013, *ApJ.*, 773, 77
- [Afanas'Ev et al.(2005)] Afanas'Ev, V. L., Dodonov, S. N., Moiseev, A. V., et al. 2005, *Astronomy Reports*, 49, 374
- [Aharonian et al.(2005)] Aharonian, F., Akhperjanian, A. G., Aye, K.-M., et al. 2005, *A. & A.*, 435, L17
- [Aharonian et al.(1999)] Aharonian, F. A., Akhperjanian, A. G., Barrio, J. A., et al. 1999, *A. & A.*, 349, 11
- [Aharonian et al.(2001)] Aharonian, F. A., Akhperjanian, A. G., Barrio, J. A., et al. 2001, *A. & A.*, 366, 62
- [Aharonian et al.(2005)] Aharonian, F., Akhperjanian, A., Beilicke, M., et al. 2005, *A. & A.*, 431, 197

- [Aharonian et al.(2006a)] Aharonian, F., Akhperjanian, A. G., Bazer-Bachi, A. R., et al. 2006, *A. & A.*, 457, 899
- [Aharonian et al.(2006b)] Aharonian, F., Akhperjanian, A. G., Bazer-Bachi, A. R., et al. 2006, *A. & A.*, 448, L43
- [Aharonian et al.(2006c)] Aharonian, F., Akhperjanian, A. G., Bazer-Bachi, A. R., et al. 2006, *ApJ.*, 636, 777
- [Aharonian et al.(2006d)] Aharonian, F., Akhperjanian, A. G., Bazer-Bachi, A. R., et al. 2006, *A. & A.*, 456, 245
- [Aharonian et al.(2007)] Aharonian, F. A., Akhperjanian, A. G., Bazer-Bachi, A. R., et al. 2007, *A. & A.*, 469, L1
- [Aharonian et al.(2012)] Aharonian, F. A., Bogovalov, S. V., & Khangulyan, D. 2012, *Nature*, 482, 507
- [H. E. S. S. Collaboration et al.(2007)] H. E. S. S. Collaboration, :, Djannati-Atai, A., et al. 2007, arXiv:0710.2247
- [Albert et al.(2007)] Albert, J., Aliu, E., Anderhub, H., et al. 2007, *ApJ.*, 663, 125
- [Aliu et al.(2013)] Aliu, E., Archambault, S., Arlen, T., et al. 2013, *ApJ.*, 764, 38
- [Arons(1996)] Arons, J. 1996, *A&AS*, 120, 49
- [Arons, J. 2006] Arons, J. 2006, On the Present and Future of Pulsar Astronomy, 26th Meeting of the IAU, Joint Discussion 2, JD02, 39, 2
- [Atkins et al.(2004)] Atkins, R., Benbow, W., Berley, D., et al. 2004, *ApJ.*, 608, 680
- [Atoyan & Aharonian(1996)] Atoyan, A. M., & Aharonian, F. A. 1996, *MNRAS*, 278, 525
- [Atwood et al.(2009)] Atwood, W. B., Abdo, A. A., Ackermann, M., et al. 2009, *ApJ.*, 697, 1071
- [Carrigan et al.(2008)] Carrigan, S., Hinton, J. A., Hofmann, W., & et al. 2008, International Cosmic Ray Conference, 2, 659

- [Cheng & Zhang(1996)] Cheng, K. S., & Zhang, J. L. 1996, *ApJ.*, 463, 271
- [Costamante & Ghisellini(2002)] Costamante, L., & Ghisellini, G. 2002, *A. & A.*, 384, 56
- [Dwek & Krennrich(2005)] Dwek, E., & Krennrich, F. 2005, *ApJ.*, 618, 657
- [de Jager & Djannati-Ataï(2009)] de Jager, O. C., & Djannati-Ataï, A. 2009, *Astrophysics and Space Science Library*, 357, 451
- [de Jager et al.(2009)] de Jager, O. C., Ferreira, S. E. S., Djannati-Ataï, A., et al. 2009, arXiv:0906.2644
- [Gabici et al.(2009)] Gabici, S., Aharonian, F. A., & Casanova, S. 2009, *MNRAS*, 396, 1629
- [Gibbs et al.(2003)] Gibbs, K., Criswell, S., Falcone, A., et al. 2003, *International Cosmic Ray Conference*, 5, 2823
- [Glendenning(1992)] Glendenning, N. K. 1992, *Phys. Rev. D*, 46, 4161
- [Gustavo E.R. and K.S. Cheng (2004)] in *Cosmic Gamma-ray Sources*, ed. K.S. Cheng 2004 *Astrophysics and Space Science Library*, 2004
- [Harding(1981)] Harding, A. K. 1981, *ApJ.*, 245, 267
- [Harding & Muslimov(2002)] Harding, A. K., & Muslimov, A. G. 2002, *ApJ.*, 568, 862
- [Harko & Cheng(2002)] Harko, T., & Cheng, K. S. 2002, *MNRAS*, 335, 99
- [Hays(2004)] Hays, E. A. 2004, Ph.D. Thesis
- [Hewish et al.(1968)] Hewish, A., Bell, S. J., Pilkington, J. D. H., Scott, P. F., & Collins, R. A. 1968, *Nature*, 217, 709
- [Hinton(2004)] Hinton, J. A. 2004, *New Astron. Rev.*, 48, 331
- [Klebesadel et al.(1973)] Klebesadel, R. W., Strong, I. B., & Olson, R. A. 1973, *ApJ. Lett.*, 182, L85
- [Konopelko et al.(2003)] Konopelko, A., Mastichiadis, A., Kirk, J., de Jager, O. C., & Stecker, F. W. 2003, *ApJ.*, 597, 851

- [Krennrich et al.(2001)] Krennrich, F., et al. 2001, *ApJ. Lett.*, 560, L45
- [Kurczynski & Gawiser(2010)] Kurczynski, P., & Gawiser, E. 2010, *AJ.*, 139, 1592
- [Lattimer et al.(1990)] Lattimer, J. M., Prakash, M., Masak, D., & Yahil, A. 1990, *ApJ.*, 355, 241
- [Lattimer & Prakash(2001)] Lattimer, J. M., & Prakash, M. 2001, *ApJ.*, 550, 426
- [Li & Ma(1983)] Li, T.-P., & Ma, Y.-Q. 1983, *ApJ.*, 272, 317
- [Lorimer & Kramer(2012)] Lorimer, D. R., & Kramer, M. 2012, Handbook of Pulsar Astronomy, by D. R. Lorimer, M. Kramer, Cambridge, UK: Cambridge University Press, 2012
- [Mattana et al.(2009)] Mattana, F., Falanga, M., Götz, D., et al. 2009, *ApJ.*, 694, 12
- [Mayer et al.(2012)] Mayer, M., Brucker, J., Holler, M., et al. 2012, arXiv:1202.1455
- [Miller et al.(2001)] Miller, C. J., et al. 2001, *AJ.*, 122, 3492
- [Muslimov & Harding(2003)] Muslimov, A. G., & Harding, A. K. 2003, *ApJ.*, 588, 430
- [Harding & Muslimov(2003)] Harding, A. K., & Muslimov, A. G. 2003, Pulsars, AXPs and SGRs Observed with BeppoSAX and Other Observatories, 121
- [Muslimov & Harding(2004)] Muslimov, A. G., & Harding, A. K. 2004, *ApJ.*, 606, 1143
- [Nolan et al.(2012)] Nolan, P. L., Abdo, A. A., Ackermann, M., et al. 2012, VizieR Online Data Catalog, 219, 90031
- [Oppenheimer & Volkoff(1939)] Oppenheimer, J. R., & Volkoff, G. M. 1939, Physical Review, 55, 374
- [Pacini & Salvati(1973)] Pacini, F., & Salvati, M. 1973, *ApJ.*, 186, 249
- [Pareschi et al.(2013)] Pareschi, G., Armstrong, T., Baba, H., et al. 2013, *Proceedings of the SPIE*, 8861,

- [Pierbattista et al.(2012)] Pierbattista, M., Grenier, I. A., Harding, A. K., & Gonthier, P. L. 2012, *A. & A.*, 545, A42
- [Punch et al.(1992)] Punch, M., Akerlof, C. W., Cawley, M. F., et al. 1992, *Nature*, 358, 477
- [Romani & Watters(2010)] Romani, R. W., & Watters, K. P. 2010, *ApJ.*, 714, 810
- [Swanenburg et al.(1981)] Swanenburg, B. N., Bennett, K., Bignami, G. F., et al. 1981, *ApJ. Lett.*, 243, L69
- [Takata et al.(2010)] Takata, J., Wang, Y., & Cheng, K. S. 2010, *ApJ.*, 715, 1318
- [Thompson, D.J. (2000)] in High Energy Gamma-Ray Astronomy, ed. F.A. Aharonian & H. J. Volk (AIP:New Yor), 103
- [Thompson(2001)] Thompson, D. J. 2001, American Institute of Physics Conference Series, 558, 103
- [VERITAS Collaboration et al.(2011)] VERITAS Collaboration, Aliu, E., Arlen, T., et al. 2011, *Science*, 334, 69
- [Wakely & Horan(2008)] Wakely, S. P., & Horan, D. 2008, International Cosmic Ray Conference, 3, 1341
- [Weekes et al.(1989)] Weekes, T. C., Cawley, M. F., Fegan, D. J., et al. 1989, *ApJ.*, 342, 379
- [Zhang & Yuan(1998)] Zhang, J. L., & Yuan, Y. F. 1998, *ApJ.*, 493, 826
- [Zhong et al.(2011)] Zhong, J., Huang, R.-S., & Lee, S.-C. 2011, Computer Physics Communications, 182, 2655